

INVESTIGATION OF THE EFFECT OF GEOMETRICAL PARAMETERS OF
PRESSURE SWIRL ATOMIZER ON THE HOLLOW CONE SPRAY

A THESIS SUBMITTED TO
THE GRADUATE SCHOOL OF NATURAL AND APPLIED SCIENCES
OF
MIDDLE EAST TECHNICAL UNIVERSITY

BY

TOLGA TOKGÖZ

IN PARTIAL FULFILLMENT OF THE REQUIREMENTS
FOR
THE DEGREE OF MASTER OF SCIENCE
IN
MECHANICAL ENGINEERING

SEPTEMBER 2019

Approval of the thesis:

**INVESTIGATION OF THE EFFECT OF GEOMETRICAL PARAMETERS
OF PRESSURE SWIRL ATOMIZER ON THE HOLLOW CONE SPRAY**

submitted by **TOLGA TOKGÖZ** in partial fulfillment of the requirements for the degree of **Master of Science in Mechanical Engineering Department, Middle East Technical University** by,

Prof. Dr. Halil Kalıpçılar
Dean, Graduate School of **Natural and Applied Sciences**

Prof. Dr. M. A. Sahir Arıkan
Head of Department, **Mechanical Engineering**

Prof. Dr. Abdullah Ulaş
Supervisor, **Mechanical Engineering, METU**

Examining Committee Members:

Assoc. Prof. Dr. Cüneyt Sert
Mechanical Engineering, METU

Prof. Dr. Abdullah Ulaş
Mechanical Engineering, METU

Prof. Dr. Kahraman Albayrak
Mechanical Engineering, METU

Assoc. Prof. Dr. M. Metin Yavuz
Mechanical Engineering, METU

Assist. Prof. Dr. Onur Baş
Mechanical Engineering, TEDU

Date: 03.09.2019

I hereby declare that all information in this document has been obtained and presented in accordance with academic rules and ethical conduct. I also declare that, as required by these rules and conduct, I have fully cited and referenced all material and results that are not original to this work.

Name, Surname: Tolga Tokgöz

Signature:

ABSTRACT

INVESTIGATION OF THE EFFECT OF GEOMETRICAL PARAMETERS OF PRESSURE SWIRL ATOMIZER ON THE HOLLOW CONE SPRAY

Tokgöz, Tolga
Master of Science, Mechanical Engineering
Supervisor: Prof. Dr. Abdullah Ulaş

September 2019, 136 pages

In this study, effects of geometrical parameters of pressure swirl atomizer on the hollow cone spray are investigated experimentally, and physical phenomenon inside the pressure swirl atomizer is investigated numerically. In the experimental studies, hollow cone spray properties are examined macroscopically and microscopically. Macroscopic spray properties are studied by a visual technique called high-speed shadowgraphy. The hollow cone spray images are captured for different geometrical configurations of the pressure swirl atomizer at different flow rates. Then, the mean spray cone angles are obtained using the image processing program and breakup lengths are measured using obtained images. Microscopic properties of spray are researched by Phase Doppler Particle Analyzer system. Microscopic properties of spray such as droplet diameters and velocity distributions are obtained for different geometrical configurations of the pressure swirl atomizer and different flow rates. Within the scope of numerical studies, two-dimensional axisymmetric swirl flow simulations are carried out to examine the internal flow and spray of the pressure swirl atomizer. In these simulations, a computational fluid dynamics tool based on volume of fluid is used. In consequence of experimental studies, it is obtained that spray cone angle is not much sensitive to the mass flow rate, nozzle length, and tangential port number. However, nozzle diameter has a remarkable impact on the spray cone angle.

Increase in nozzle diameter leads to an increase in the spray cone angle. Decreasing nozzle diameter and increasing mass flow rate result in a shortening of the breakup length. On the other hand, nozzle length and tangential port number have minor effect on the breakup length. Microscopically, x-velocity and y-velocity of the droplets are dependent on the mass flow rate and nozzle diameter, and magnitudes of velocities increase with increasing mass flow rate and decreasing nozzle diameter. On the contrary, nozzle length and tangential port number has a negligible effect on the magnitudes of velocities. Sauter mean diameter of the hollow cone spray increases with increasing nozzle diameter and decreasing mass flow rate, but nozzle length has no significant effect on it. However, increasing tangential port number increases the uniformity of the particle and Sauter mean diameter distribution. As a result of numerical studies, complex two-phase flow and velocity distributions in the pressure swirl atomizer are studied. Numerical results show that spray cone angle and air core diameter remain nearly the same with increasing mass flow rate. On the contrary, increasing mass flow rate causes an increase in axial and swirl velocities.

Keywords: Pressure Swirl Atomizer, Phase Doppler Particle Analyzer, Spray Cone Angle, Breakup Length, Hollow Cone Spray, High Speed Shadowgraphy Technique, Sauter Mean Diameter, Air Core Diameter, Computational Fluid Dynamics.

ÖZ

BASINÇLI GİRDAP TİPİ PÜSKÜRTECİN GEOMETRİK PARAMETRELERİNİN SPREY ÜZERİNDEKİ ETKİSİNİN ARAŞTIRILMASI

Tokgöz, Tolga
Yüksek Lisans, Makina Mühendisliği
Tez Danışmanı: Prof. Dr. Abdullah Ulaş

Eylül 2019, 136 sayfa

Bu çalışmada, basınçlı girdap tipi püskürtecın geometrik parametrelerinin sprej üzerindeki etkisi deneysel olarak araştırılmıřtır ve basınçlı girdap tipi püskürtecın iç akıřındaki fiziksel olgular sayısal yöntemlerle incelenmiřtir. Deneysel çalışmalarda sprejin makroskobik ve mikroskobik özellikleri incelenmiřtir. Makroskobik özellikler, Yüksek Hızlı Gölge Görüntüleme Tekniđi kullanılarak görselleřtirilmiřtir. Farklı geometrik özelliklere sahip basınçlı girdap tipi püskürteçler için üç farklı kütlelel debi deđerinde sprej görüntüleri alınmıřtır. Daha sonra, görüntü iřleme aracı kullanılarak ortalama sprej koni açıları elde edilmiřtir ve elde edilen görüntüler üzerinden dađılma uzunluđu ölçülmüřtür. Sprejin mikroskobik özellikleri Faz Doppler Parçacık Analizcisi ile araştırılmıřtır. Farklı geometrik özelliklere sahip basınçlı girdap tipi püskürteçler için sprejin parçacık çap ve hız dađılımları üç farklı kütlelel debi deđerinde elde edilmiřtir. Sayısal çalışmalar kapsamında, basınçlı girdap tipi püskürtecın iç akıřını ve sprejini incelemek amacıyla iki boyutlu aksenele simetrik girdap akıřı benzetimleri gerçekteřtirilmiřtir. Bu benzetimlerde, sonlu hacim yöntemi tabanlı bir hesaplamalı akıřkanlar dinamiđi aracı kullanılmıřtır. Deneysel çalışmalar sonucunda, sprej koni açısının kütlelel debiye, nozul uzunluđuna ve teđetsel giriş sayısına çok fazla duyarlı olmadıđı, fakat nozul çapının sprej koni açısı üzerinde bir etkisi olduđu elde edilmiřtir. Artan nozul çapının sprej koni açısında bir artışa sebep

olduđu grlmřtr. Dađılma uzunluđunun, artan ktlesel debi ve azalan nozul apı ile kısaldıđı gzlenmiřtir. Diđer taraftan, nozul uzunluđu ve teđetsel giriř sayısının dađılma uzunluđuna nemli bir etkisinin olmadıđı elde edilmiřtir. Mikroskobik olarak, paracıkların x-hızı ve y-hızının ktlesel debi ve nozul apına bađlı olduđu ve hızların byklđnn artan ktlesel debi ve azalan nozul apı ile arttıđı belirlenmiřtir. Aksine, nozul uzunluđunun ve teđetsel giriř sayısının hızlar zerindeki etkisinin ihmal edilebilir seviyelerde olduđu elde edilmiřtir. Spreyin Sauter ortalama ap deđerinin artan nozul apı ve azalan ktlesel debi deđerleriyle arttıđı fakat deđiřen nozul uzunluđu ile nemli lde deđiřmediđi gzlemlenmiřtir. Bununla birlikte, teđetsel giriř sayısındaki artıřın ise paracık ve Sauter ortalama ap dađılımlarının homojenliđini arttırdıđı belirlenmiřtir. Sayısal alıřmaların sonucu olarak, basınlı girdap tipi pskrtecin iindeki karmařık iki fazlı akıř ve hız dađılımları incelenmiřtir. Sayısal sonular, spreyn koni aısının ve hava ekirdeđi apının artan ktlesel debi deđerlerinde neredeyse aynı kaldıđını gstermiřtir. Eksenel ve dnsel hızların ise ktlesel debi deđerlerine bađlı olduđu ve artan debi deđerleriyle arttıđı belirlenmiřtir.

Anahtar Kelimeler: Basınlı Girdap Tipi Pskrte, Spreyn Koni Aısı, Dađılma Uzunluđu, İi Boř Koni Spreyn, Yksek Hızlı Glge Grntleme Tekniđi, Sauter Ortalama apı, Faz Doppler Paracık Analizcisi, Hava ekirdeđi apı, Hesaplamalı Akıřkanlar Dinamiđi.

To my family...

ACKNOWLEDGEMENTS

Firstly, I wish to express my deepest gratitude to my supervisor Prof. Dr. Abdullah ULAŞ for his guidance, understanding, and insight throughout the research.

I would like to thank to my thesis committee members for their valuable comments on the research.

Furthermore, I am grateful to the Chief of the Propulsion Systems Division in TÜBİTAK SAGE, Dr. Bülent SÜMER, for his support and precious help on research.

I would like to express my sincere to my colleagues at TÜBİTAK SAGE, especially Bora YAZICI, for their crucial advises during the preparation of this thesis.

I would like to thank my mother Nihayet TOKGÖZ, my father Naci TOKGÖZ, my sister Burcu TOKGÖZ and my brother Alp Tugay TOKGÖZ for their continuous support and encouragement through my life.

Special thanks go to my wife, Semra GÜMRÜK TOKGÖZ, for her understanding, patience, support, and love during this difficult period.

Finally, this thesis is dedicated to my family. It would be impossible without their support and understanding.

TABLE OF CONTENTS

ABSTRACT	v
ÖZ	vii
ACKNOWLEDGEMENTS	x
TABLE OF CONTENTS	xi
LIST OF TABLES	xv
LIST OF FIGURES	xvi
LIST OF SYMBOLS	xxi
LIST OF ABBREVIATIONS	xxii
CHAPTERS	
1. INTRODUCTION	1
1.1. Research Background.....	1
1.2. Research Problem.....	10
1.3. Literature Survey	11
1.3.1. Introduction.....	11
1.3.2. Research on Effect of Geometrical Parameters on Pressure Swirl Atomizer Performance	11
1.4. Content of the Thesis.....	24
1.5. Definitions	24
1.5.1. Arithmetic Mean Diameter	24
1.5.2. Sauter Mean Diameter	25
1.5.3. Spray Cone Angle.....	25
1.5.4. Breakup Length.....	25

1.5.5. Discharge Coefficient.....	26
2. EXPERIMENTAL SETUP & MEASUREMENT DETAILS.....	27
2.1. Introduction.....	27
2.2. Experimental Setup.....	27
2.3. Atomizer Test Assembly.....	28
2.3.1. Introduction.....	28
2.3.2. Pressure Swirl Atomizer.....	30
2.3.3. Reservoir.....	32
2.3.3.1. Introduction.....	32
2.3.3.2. Verification of Reservoir Design.....	32
2.3.3.3. Simulation Results.....	35
2.3.3.4. Conclusion.....	36
2.4. Experimental Method.....	37
2.4.1. High Speed Shadowgraphy System.....	37
2.4.1.1. Image Processing.....	38
2.4.1.2. Pixel Coordinates Conversion to Physical Coordinates.....	39
2.4.2. Phase Doppler Particle Analyzer.....	40
2.4.2.1. Verification of PDPA System Measurement.....	42
2.5. Experimental Investigation of the Hollow Cone Spray.....	47
2.5.1. Macroscopic Properties.....	47
2.5.1.1. Spray Cone Angle.....	47
2.5.1.2. Breakup Length.....	49
2.5.2. Microscopic Properties.....	49
2.6. Pressure Drop Measurement.....	51

3. NUMERICAL SIMULATIONS.....	53
3.1. Introduction	53
3.2. Method of Numerical Solution.....	53
3.2.1. Boundary Conditions	54
3.2.2. Measurement Locations	55
3.2.3. Grid Sensitivity Study.....	56
3.2.3.1. Grid Sensitivity Simulations Results	57
3.2.3.2. Conclusion	63
3.2.4. Spray Cone Angle Calculation	64
4. RESULT OF EXPERIMENTAL STUDY	65
4.1. Results of Macroscopic Properties	65
4.1.1. Results of Spray Cone Angle Measurements	65
4.1.2. Results of Breakup Length Measurements	68
4.2. Results of Microscopic Measurements.....	69
4.2.1. Nozzle Diameter Effects on the Microscopic Properties.....	71
4.2.2. Nozzle Length Effect on the Microscopic Properties.....	80
4.2.3. Tangential Port Number Effect on the Microscopic Properties.....	89
4.2.4. Mass Flow Rate Effect on the Microscopic Properties.....	98
4.3. Results of Pressure Drop Measurements	101
5. RESULTS OF NUMERICAL STUDY	103
5.1. Introduction	103
5.2. Numerical Simulation Results.....	103
5.2.1. Pressure Swirl Atomizer Flow	103
5.2.2. Mass Flow Rate Effect on the Pressure Swirl Atomizer Flow	107

5.2.2.1. Mass Flow Rate Effect on Mean Volume Fraction	107
5.2.2.2. Mass Flow Rate Effect on Spray Cone Angle and Air Core Diameter	108
5.2.2.3. Mass Flow Rate Effect on Mean Axial Velocity	109
5.2.2.4. Mass Flow Rate Effect on Mean Swirl Velocity	110
5.2.3. Spray Cone Angle	110
6. COMPARISON OF EXPERIMENTAL AND NUMERICAL RESULTS	111
6.1. Spray Cone Angle Comparison.....	111
6.2. Axial and Radial Velocity Comparison	112
7. CONCLUSIONS	115
REFERENCES	119
APPENDICES	
A. Mass Flow Rate Effect on Microscopic Properties of Test Atomizers	125

LIST OF TABLES

TABLES

Table 1.1. SMD Correlations [21].....	20
Table 2.1. Selected Test Atomizers	31
Table 2.2. Mass Flow Rates at Measurement Locations.....	36
Table 2.3. Calculated Deviations for Tangential Ports	36
Table 2.4. Settings of High-Speed Camera for SCA Measurement.....	37
Table 2.5. Comparison of Theoretical Values and MDG Measurement Results.....	44
Table 2.6. Comparison of Theoretical Values and MDG Measurement Results.....	46
Table 4.1. Image Quantity Dependency.....	65
Table 4.2. Calculated Mean SCAs for Selected Atomizers	65
Table 4.3. Calculated Mean SCAs for Selected Atomizers	66
Table 4.4. Calculated Mean SCAs for Selected Atomizers	66
Table 4.5. Radial and Axial Velocity Components of Baseline PSA.	67
Table 4.6. Measured Breakup Lengths for Selected Atomizers.....	68
Table 4.7. Measured Breakup Lengths for Selected Atomizers.....	68
Table 4.8. Measured Breakup Lengths for Selected Atomizers.....	68
Table 4.9. Mean Pressure Drop Values of Atomizers as a Function of Nozzle Diameter at Different Mass Flow Rates.....	101
Table 4.10. Mean Pressure Drop Values of Atomizers as a Function of Nozzle Length at Different Mass Flow Rates.....	101
Table 4.11. Mean Pressure Drop Values of Atomizers as a Function of Tangential Port Number at Different Mass Flow Rates	102
Table 5.1. Mean SCA of Baseline PSA	110
Table 6.1. Comparison of SCAs	111

LIST OF FIGURES

FIGURES

Figure 1.1. A Schematic of LRE	1
Figure 1.2. Thrust Chamber Assembly	2
Figure 1.3. Pressure Atomizers [4]	5
Figure 1.4. Rotary Atomizers [4]	5
Figure 1.5. Air Assist Atomizers [4]	6
Figure 1.6. Air Blast Atomizers [4]	6
Figure 1.7. Main Parts of PSA	7
Figure 1.8. Schematic View of PSA	7
Figure 1.9. Spray Development of PSA with Increasing Injection Pressure [4]	8
Figure 1.10. a) Closed-End PSA, b) Open-End PSA	9
Figure 1.11. Coaxial Pressure Swirl Injector	10
Figure 1.12. Geometrical Parameters of PSA	10
Figure 1.13. Geometrical Parameters Effects on SCA and SMD [10]	12
Figure 1.14. Effects of geometrical parameters of PSA on its performance [12]	14
Figure 1.15. Effects of the atomizer constant, D_s/D_o , L_s/D_s , and L_o/D_o on the dimensionless liquid film thickness at the orifice exit, discharge coefficient, and half SCA [13]	15
Figure 1.16. Effect of injection pressure, L_o/D_o , N_{tp} and liquid viscosity on SCA [14]	16
Figure 1.17. Effect of tangential port number and injection pressure on discharge coefficient and SCA [17]	18
Figure 1.18. Effect of geometrical parameters on SMD [21]	20
Figure 1.19. a) Comparison of measured SMD and predicted SMD for water b) Comparison of measured SMD and predicted SMD for Jet A-1 [21]	21
Figure 1.20. Effect of Varying Parameters on dynamic properties of PSA [27]	22

Figure 1.21. Spray Cone Angle.....	25
Figure 2.1. A Schematic of the Experimental Facility.....	27
Figure 2.2. Experimental Facility	28
Figure 2.3. Mechanical Design of Atomizer Test Assembly.....	29
Figure 2.4. The technical drawing of the baseline PSA.....	30
Figure 2.5. A Sample Manufactured PSA.....	31
Figure 2.6. Simple Analysis Model and Boundary Conditions	32
Figure 2.7. Generated Four Grids	33
Figure 2.8. Mesh Blocks of Computational Domain	34
Figure 2.9. Tangential Ports with Render Mode for Computational Domains	35
Figure 2.10. Close View of Tangential Ports with Render Mode for Computational Domains	35
Figure 2.11. Captured Images of the Hollow Cone Spray	37
Figure 2.12. Application of Sobel Edge Detector	38
Figure 2.13. Intensity Distribution on a Line at $x=275$ pixel.....	38
Figure 2.14. Position of Rulers	39
Figure 2.15. A Schematic of TSI Two-Component PDPA System [31]	40
Figure 2.16. TSI Two-Component PDPA System in Facility.....	40
Figure 2.17. Probe Volume [32]	41
Figure 2.18. Monosize Droplet Generator [33].....	42
Figure 2.19. A general view of MDG	43
Figure 2.20. Velocity Measurement with HSSS	45
Figure 2.21. Actual Velocity Calculation	46
Figure 2.22. Hollow Cone Spray of Baseline PSA (A-1) for Different Flow Rates..	47
Figure 2.23. Calculation Method of SCA	48
Figure 2.24. Demonstration of Breakup Length	49
Figure 2.25. Measurement Points of Velocity Distribution and SMD.....	50
Figure 2.26. Snapshots of Hollow Cone Spray and Velocity-Droplet Size Measurement with PDPA.....	50
Figure 2.27. Location of Pressure Transducer	51

Figure 3.1. Boundary Conditions.....	55
Figure 3.2. Measurement Locations	56
Figure 3.3. Grid Sensitivity	56
Figure 3.4. Evolution of air volume fraction contours for GRID1, GRID2, GRID3 and GRID4.....	57
Figure 3.5. Contours of Mean Volume Fraction for Air.....	58
Figure 3.6. Contours of Mean volume fraction for air at the beginning of the swirl chamber.....	59
Figure 3.7. Contours of Mean Static Pressure [bars].....	59
Figure 3.8. Contours of Mean Axial Velocity Contours [m/s].....	60
Figure 3.9. Contours of Mean Swirl Velocity [m/s].....	61
Figure 3.10. Mean Static Pressure at Designated Lines	62
Figure 3.11. Mean Axial Velocities at Designated Lines.....	62
Figure 3.12. Mean Swirl Velocities at Designated Lines	63
Figure 3.13. Sobel Edge Detector Application for Numerical Simulations	64
Figure 4.1. X-Velocity Histograms at designated locations (A-1).....	69
Figure 4.2. Y-Velocity Histograms at designated locations (A-1).....	70
Figure 4.3. Diameter Histograms at designated locations (A-1).....	70
Figure 4.4. Nozzle Diameter Effect on the Microscopic Properties for Q_1	72
Figure 4.5. Nozzle Diameter Effect on the Microscopic Properties for Q_2	74
Figure 4.6. Nozzle Diameter Effect on the Microscopic Properties for Q_3	75
Figure 4.7. Comparison of the Effect of Nozzle Diameter on the Microscopic Properties for $Q_1=0.100$ kg/s at Specified x Coordinates.....	77
Figure 4.8. Comparison of the Effect of Nozzle Diameter on the Microscopic Properties for $Q_2=0.173$ kg/s at Specified x Coordinates.....	78
Figure 4.9. Comparison of the Effect of Nozzle Diameter on the Microscopic Properties for $Q_3=0.240$ kg/s at Specified x Coordinates	79
Figure 4.10. Nozzle Length Effect on the Microscopic Properties for Q_1	81
Figure 4.11. Nozzle Length Effect on the Microscopic Properties for Q_2	83
Figure 4.12 Nozzle Length Effect on the Microscopic Properties for Q_3	84

Figure 4.13. Comparison of the Nozzle Length Effect on the Microscopic Properties for $Q_1=0.100$ kg/s at Specified x Coordinates.....	86
Figure 4.14. Comparison of Nozzle Length Effect on the Microscopic Properties for $Q_2=0.173$ kg/s at Specified x Coordinates.	87
Figure 4.15. Comparison of Nozzle Length Effect on the Microscopic Properties for $Q_3=0.240$ kg/s at Specified x Coordinates.	88
Figure 4.16. Tangential Port Number Effect on the Microscopic Properties for Q_1 ..	90
Figure 4.17. Tangential Port Number Effect on the Microscopic Properties for Q_2 ..	92
Figure 4.18. Tangential Port Number Effect on the Microscopic Properties for Q_3 ..	93
Figure 4.19. Comparison of Tangential Port Number Effect on the Microscopic Properties for $Q_1=0.100$ kg/s at Specified x Coordinates	95
Figure 4.20. Comparison of Tangential Port Number Effect on the Microscopic Properties for $Q_2=0.173$ kg/s at Specified x Coordinates	96
Figure 4.21. Comparison of Tangential Port Number Effect on the Microscopic Properties for $Q_3=0.240$ kg/s at Specified x Coordinates.	97
Figure 4.22. Mass Flow Rate Effect on the Microscopic Properties of Baseline PSA	99
Figure 4.23. Comparison of Mass Flow Rate Effect on the Microscopic Properties of Baseline PSA at Specified x Coordinates.	100
Figure 5.1. Contours of Mean Volume Fraction for Air [m/s].....	103
Figure 5.2. Mean Volume Fractions at Measurement Lines.....	104
Figure 5.3 Contours of Mean Axial Velocity [m/s]	104
Figure 5.4. Mean Axial Velocities at Measurement Lines.....	105
Figure 5.5. Contours of Mean Swirl Velocity [m/s]	106
Figure 5.6. Mean Swirl Velocities at Measurement Lines.....	106
Figure 5.7. Mass Flow Rate Effect on Mean Volume Fractions at Designated Lines	107
Figure 5.8. Mass Flow Rate Effect on SCA and Air Core Diameter at Designated Lines	108
Figure 5.9 Mass Flow Rate Effect on Axial Velocities at Designated Lines.....	109

Figure 5.10. Mass Flow Rate Effect on Mean Swirl Velocities at Designated Lines	110
Figure 6.1. Comparison of Spray Cone Angle Graphically.....	111
Figure 6.2. Comparison of Axial Velocities at x=20 mm for Three Mass Flow Rates	112
Figure 6.3. Comparison of Radial Velocities at x=20 mm for Three Mass Flow Rates	113
Figure A.1. Mass Flow Rate Effect on the Microscopic Properties of A-2.....	125
Figure A.2. Comparison of Mass Flow Rate Effect on the Microscopic Properties of A-2 at Specified x Coordinates.....	126
Figure A.3. Mass Flow Rate Effect on the Microscopic Properties of A-3.....	127
Figure A.4. Comparison of Mass Flow Rate Effect on the Microscopic Properties of A-3 at Specified x Coordinates.....	128
Figure A.5. Mass Flow Rate Effect on the Microscopic Properties of A-6.....	129
Figure A.6. Comparison of Mass Flow Rate Effect on the Microscopic Properties of A-6 at Specified x Coordinates.....	130
Figure A.7. Mass Flow Rate Effect on the Microscopic Properties of A-7.....	131
Figure A.8. Comparison of Mass Flow Rate Effect on the Microscopic Properties of A-7 at Specified x Coordinates.....	132
Figure A.9. Mass Flow Rate Effect on the Microscopic Properties of A-5.....	133
Figure A.10. Comparison of Mass Flow Rate Effects on the Microscopic Properties of A-5 at Specified x Coordinates	134
Figure A.11. Mass Flow Rate Effect on the Microscopic Properties of A-4.....	135
Figure A.12. Comparison of Mass Flow Rate Effect on the Microscopic Properties of A-4 at Specified x Coordinates.....	136

LIST OF SYMBOLS

SYMBOLS

A_o	=	cross-sectional area of nozzle orifice
A_p	=	tangential port area
C_d	=	discharge coefficient
D_o	=	nozzle diameter
D_s	=	swirl chamber diameter
D_{tp}	=	tangential port diameter
L_o	=	nozzle length
L_s	=	swirl chamber radius
L_{tp}	=	tangential port length
N_{tp}	=	tangential port number
Q	=	mass flow rate
R_n	=	nozzle radius
R_{sc}	=	swirl chamber radius
R_{tp}	=	tangential port radius
V_a	=	axial velocity
V_r	=	radial velocity
V_t	=	tangential velocity
α	=	spray cone angle
β	=	convergence angle
θ	=	divergence angle

LIST OF ABBREVIATIONS

ABBREVIATIONS

CFD	=	Computational Fluid Dynamics
FN	=	Flow Number
HSSS	=	High Speed Shadowgraphy System
LOX	=	Liquid Oxygen
LRE	=	Liquid Rocket Engine
MDG	=	Monosize Droplet Generator
MFR	=	Mass Flow Rate
PDPA	=	Phase Doppler Particle Analyzer
PSA	=	Pressure Swirl Atomizer
SCA	=	Spray Cone Angle
SMD	=	Sauter Mean Diameter
TP	=	Tangential Ports
VOF	=	Volume of Fluid

CHAPTER 1

INTRODUCTION

In this chapter, principal information related to the liquid propellant rocket engines, devices used for liquid atomization, and pressure swirl atomizers is given. Firstly, background to the research is presented. Afterwards, research problem is defined. Then, literature survey about this work is presented, and content of the thesis is explained. Lastly, definitions are given.

1.1. Research Background

Liquid Rocket Engine (LRE) is a rocket engine that generates thrust using liquid propellants. The LREs are used commonly in rockets and launch systems. This kind of engines have high performance, restart chance and thrust regulation capability [1]. A typical LRE consists of propellant feed system and thrust chamber assembly [1]. A general schematic which shows the main elements of an LRE together with the fuel/oxidizer tanks is demonstrated in Figure 1.1.

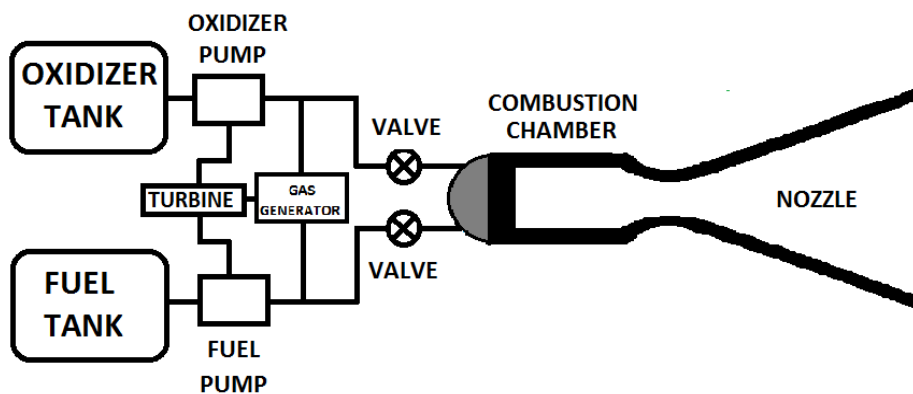


Figure 1.1. A Schematic of LRE

In LREs, fuel and oxidizer are stored separately in the fuel tank and oxidizer tank. Stored propellants are transferred from the tanks into the thrust chamber assembly using propellant feed system, and they burn in the thrust chamber assembly to generate thrust based on the Newton's third law as a result of chemical reaction. The thrust equation [2] is given below:

$$F = \frac{\dot{w}}{g} V_e + A_e (P_e - P_a) \quad (1.1)$$

where F indicates the thrust force of LRE, \dot{w} indicates the weight flow rate, g indicates the gravitational acceleration, V_e indicates the exhaust velocity, A_e indicates the exit area of the engine's gas exhaust, P_a indicates the atmospheric pressure, and P_e indicates the local pressure of the hot gas jet at the exit plane of the nozzle.

Thrust chamber assembly mainly consists of a number of injectors, combustion chamber, and nozzle. The injectors atomize fuel and oxidizer into small droplets and spray into the combustion chamber. Atomized fuel and oxidizer mix and burn in the combustion chamber to generate a high velocity and high-pressure stream of hot gases. The resulting hot gases pass through the converging-diverging nozzle and nozzle converts the enthalpy of the hot gases into kinetic energy and generates thrust. In Figure 1.2, the basic components of thrust chamber assembly are depicted.

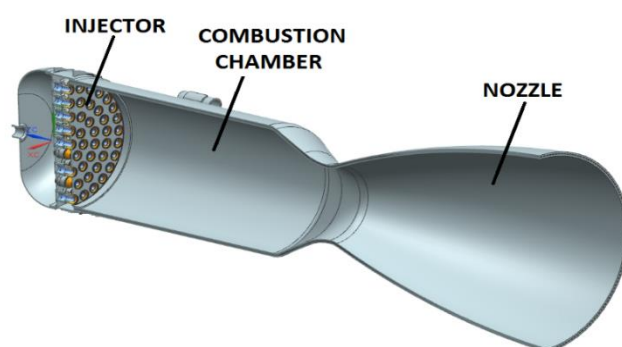


Figure 1.2. Thrust Chamber Assembly

The injector is the one of the most important part of the thrust chamber assembly which mixes and atomizes the fuel and oxidizer, and starts the combustion. An efficient and stable combustion is possible with a successful injector performance; therefore, the thrust chamber assembly performance directly depends on the injector. The main purpose of the injector is to produce high combustion performance and provide stable operation conditions without endangering the thrust chamber assembly endurance [3].

Atomization process has an importance in many industrial applications. Bulk liquid is separated into small droplets via atomizer. Atomizers are categorized as pressure atomizer, rotary atomizer, and twin fluid atomizer [4].

Pressure atomizers convert the pressure energy into kinetic energy and generate spray. Types of pressure atomizers are given in Figure 1.3.

Plain-orifice type pressure atomizers include a circular orifice for atomization. In plain-orifice atomizers, decreasing orifice diameter increases the atomization quality. Plain-orifice atomizers are simple, cheap, and durable, however, they have solid spray cone and narrow spray cone angle (SCA) [4]. These atomizers are generally used in combustion applications of diesel engines, ramjets, and rocket engines.

Pressure swirl atomizers (PSAs) have swirl chamber which is fed with tangential ports in addition to the circular orifice. In PSAs, liquid passes into the swirl chamber via the tangential ports and discharge the circular orifice as a conical sheet. PSAs have simple design, wide SCA, good atomization performance, and stable combustion characteristics, therefore they are widely used in gas turbines, rocket engines and many other applications [4]. A disadvantage of PSAs is that they have poor atomization performance for low inlet pressures.

Duplex atomizers have two inlet slots as small and large to feed the swirl chamber. At low flow rates, fluid passes into the swirl chamber through the small slot. When the flow rate increases, fluid passes through the large slot and enters the swirl chamber. In this way, duplex atomizers allow good atomization at high flow rates without requiring high delivery pressures. However, poor atomization quality is observed near the point where secondary liquid is first admitted into the swirl chamber, and SCA changes with changing flow rate [4]. Duplex atomizers are generally used in gas turbines and in some other engineering applications [5].

In addition to two slides as in duplex atomizer, dual orifice atomizers have two coaxial swirl chambers. At low flow rates, fluid flows through the inner section. At high flow rates, fluid continues to pass through the primary section, but most of the fluid passes through the secondary section [4]. The dual orifice atomizers have a wide working pressure range than PSAs, but atomization quality decreases when the distribution valve is opening [5], [6]. These type atomizers are commonly used in industrial and aircraft engines [4].

Fan spray atomizers have an orifice which has V groove at the end of cylindrical port. Fan spray atomizers have good atomization performance; however, they need high supply pressure values. These atomizers are generally used in the coating industry, small annular gas turbine combustors, and painting applications [4].

Spill return atomizers are similar to simplex atomizers; the only difference is that spill return atomizers have a return flow line and a valve to control the liquid flow from the swirl chamber to liquid source [4]. Spill return atomizers have better atomization quality than PSAs for low flow rates. However, metering of flow rate is so complicated in these type atomizers and SCA changes with varying flow rate which has a negative effect combustion efficiency [7]. Because of these drawbacks, the use of spill return atomizers in aircraft engines has declined [6].

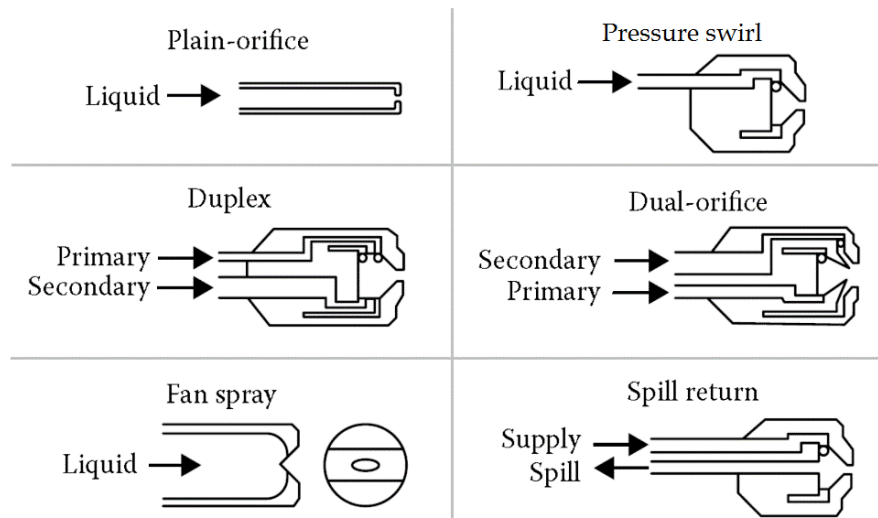


Figure 1.3. Pressure Atomizers [4]

Rotary atomizers atomize the liquid by a high-speed rotating disk. The liquid flows through the rotary disk and leaves from its outer edge at high velocity [4]. Nearly uniform atomization is possible by rotary atomizers and atomization quality is independent from flow rate. However, a 360° spray pattern is generated by rotary atomizers. These atomizers are widely used in spray drying and crop spraying applications. A schematic of rotary atomizer is given in Figure 1.4.

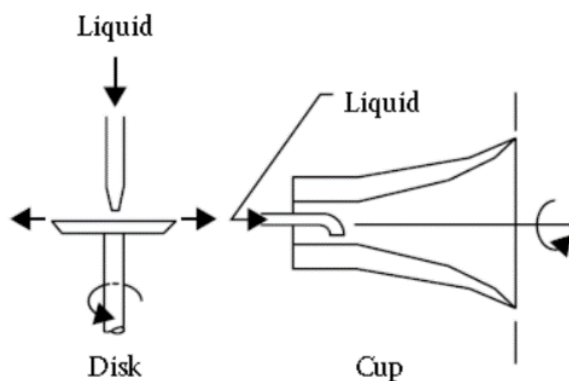


Figure 1.4. Rotary Atomizers [4]

Air assist atomizers mix the liquid with air or steam at high velocity (usually sonic). In internal mixing air assist atomizers, mixing of liquid and gas occurs inside the atomizer. On the contrary, liquid and gas mix at the outside of the atomizer in external mixing air assist atomizers. These types of atomizers are a good choice to atomize the high viscosity liquids, and used in industrial furnaces and industrial gas turbines [4]. Schematics of air assist atomizers are given in Figure 1.5.

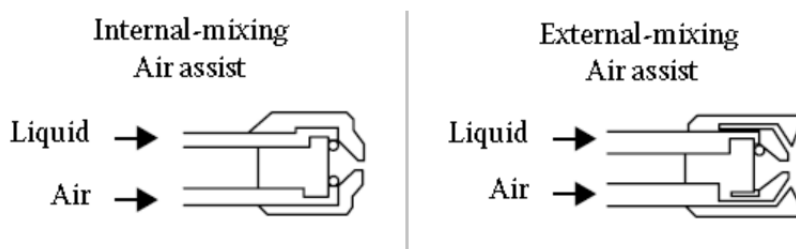


Figure 1.5. Air Assist Atomizers [4]

Air blast atomizers are very similar to air assist atomizers, the main difference is the amount of air or steam used. Air blast atomizers use air or steam at a greater amount and lower speed (<100 m/s) than air assist atomizers. Air blast atomizers are generally used in continuous flow combustion systems. There are two types of air blast atomizers as plain jet and prefilming. In plain jet air blast atomizers, liquid is injected into the air as one or more discrete jets. In prefilming air blast atomizers, liquid which is formed into a thin conical sheet is subjected to the high velocity air stream [4]. Air blast atomizer types are shown in Figure 1.6.

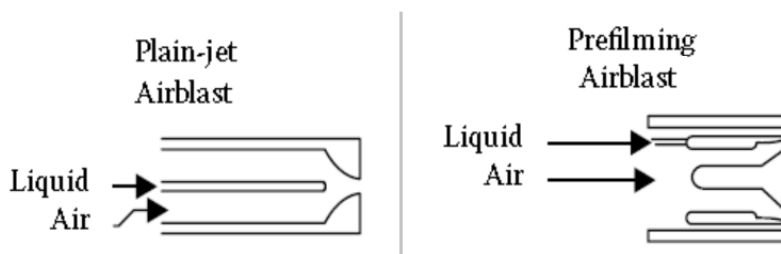


Figure 1.6. Air Blast Atomizers [4]

Although the PSAs are simple and inexpensive, they have good atomization characteristics. Furthermore, these types of atomizers are one of the most reliable types of atomizer, and they contribute a stable combustion and provide high thrust. PSAs consist of four main parts as tangential port, swirl chamber, nozzle, and convergence section. The main parts of the PSAs are indicated in Figure 1.7.

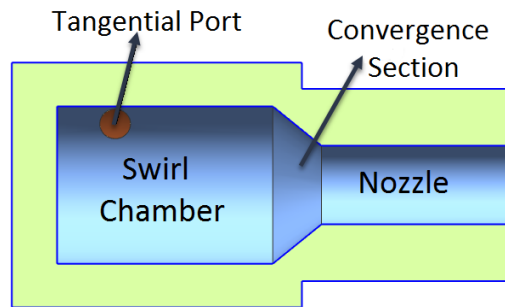


Figure 1.7. Main Parts of PSA

In a PSA, liquid passes through a number of tangential ports, then enters the swirl chamber, and begins a swirling motion. Due to the high swirl velocity, the pressure through the centerline of the atomizer drops below the ambient pressure, and air begins to flow into the atomizer from the ambient and an air core forms around the axis of the PSA. Then, the liquid takes the shape of a thin film and exits from the nozzle as a hollow conical sheet. The rotating thin film disintegrates into small droplets at atomizer exit and atomization occurs [5]. A schematic view of the PSA is given in Figure 1.8.

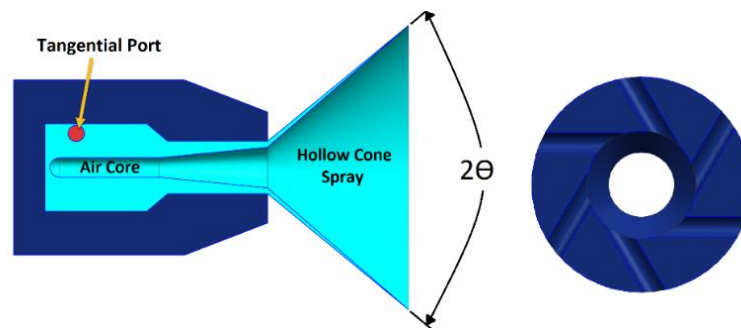


Figure 1.8. Schematic View of PSA

According to Lefebvre [4], the evolution of spray consists of five steps defined below:

- I. Liquid drips from the nozzle.
- II. Liquid flows as a “thin distorted pencil”.
- III. A cone shapes at the exit of the nozzle, but is shrunk by surface tension forces into a closed bubble as an “onion shape”.
- IV. The bubble opens into a hollow “tulip shape” terminating in an irregular edge, where the liquid breaks into big droplets.
- V. The curved surface takes shape a conical sheet. The thickness of the expanding sheet decreases, and sheet becomes unstable and breaks into small droplets and then “a fully developed hollow cone spray” occurs.

The spray development of PSA is demonstrated in Figure 1.9 as the schematic representation of Lefebvre [4].

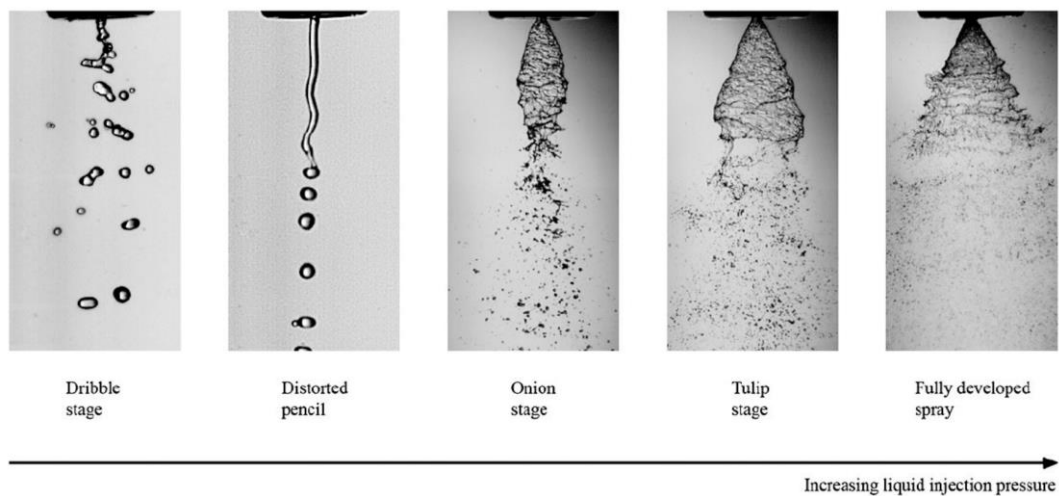


Figure 1.9. Spray Development of PSA with Increasing Injection Pressure [4]

The PSAs are categorized into two types as closed-end and open-end. Closed-end PSAs have a convergence section between the nozzle and swirl chamber. On the contrary, there is no convergence section in the open-end PSAs, and swirl chamber and nozzle diameters are identical. Schematic views of closed-end and open-end PSAs are given in Figure 1.10.

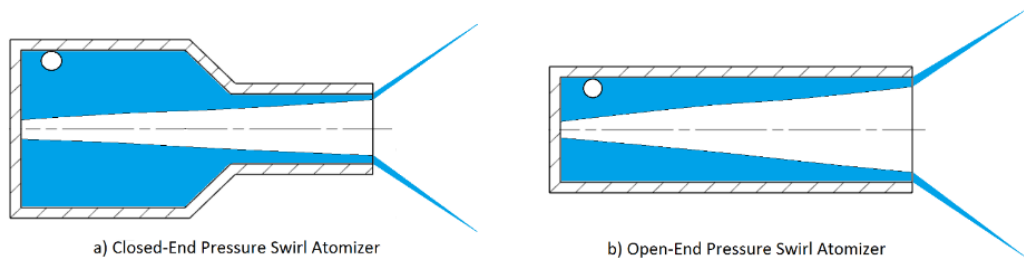


Figure 1.10. a) Closed-End PSA, b) Open-End PSA

The flow mechanisms of closed-end and open-end PSA is different as there is no convergence section in open-end one. First difference is that axial velocity in the swirl chamber is greater in open-end PSA than closed-end one. Secondly, the liquid fluctuation process of open-end PSA contains no reflected wave [8]. Open-end PSAs have no evident advantage, atomization performance of them is worse than closed-end PSAs, but they are still in use due to their effective dynamic performances [8]. Open-end and closed-end PSAs are both generally used in Russian engines because of their minor combustion instability problems [9]. In coaxial pressure swirl injectors, open-end and closed-end PSAs are generally used together as shown in Figure 1.11. Inner atomizer is selected as closed-end type to atomize the oxidizer and outer atomizer is selected as open-end type to atomize the fuel.

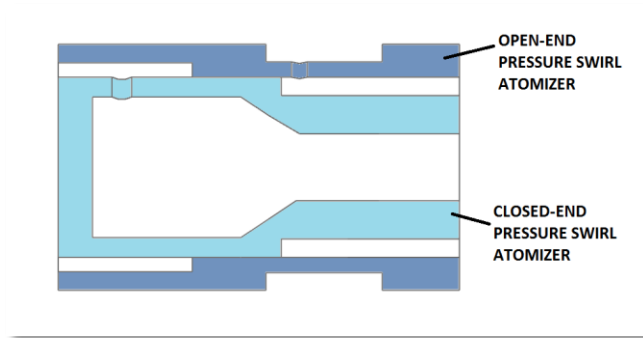


Figure 1.11. Coaxial Pressure Swirl Injector

1.2. Research Problem

Atomization and spray characteristics of a PSA highly depend on the geometrical properties. PSAs have numerous geometrical parameters affecting the combustion efficiency and stability. Among the several geometrical parameters of a PSA the leading eight geometrical parameters are swirl chamber length (L_s), swirl chamber diameter (D_s), nozzle diameter (D_o), nozzle length (L_o), tangential port diameter (D_{tp}), tangential port length (L_{tp}), tangential port number (N_{tp}), convergence section length (L_c), and convergence angle (β). The mentioned geometrical parameters are shown in Figure 1.12.

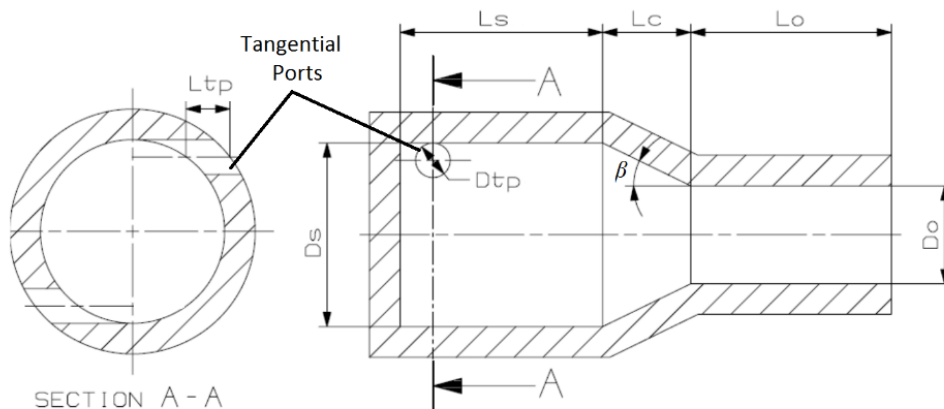


Figure 1.12. Geometrical Parameters of PSA

In order to gain knowledge about the atomization characteristic, it is necessary to study the effect of geometrical parameters on the hollow cone spray for PSA.

The effects of geometrical parameters on the microscopic properties of PSA have been studied by few researchers. Therefore, the main purpose of this thesis is the investigation of the geometrical parameters of PSA on the macroscopic and microscopic properties spray. The inner oxidizer atomizer of the bi-propellant injector of the RD-0110 rocket engine is selected as the baseline PSA for this thesis. At the beginning of the study, the macroscopic and microscopic properties of the hollow cone spray for the selected geometrical configurations of the PSA are studied experimentally with High Speed Shadowgraphy and Phase Doppler Particle Analyzer, respectively. Then, numerical simulations are carried out with baseline PSA to examine the internal flow phenomenon of the atomizer.

1.3. Literature Survey

1.3.1. Introduction

In this section, the literature is reviewed for the former works related to the PSA and its geometrical parameters effects on the hollow cone spray.

1.3.2. Research on Effect of Geometrical Parameters on Pressure Swirl Atomizer Performance

Internal and external characteristics of the PSAs are affected from the geometrical parameters. Therefore, the researchers are focused on geometrical parameters of PSAs to optimize the atomizer geometry.

Muhammad Rashad et. al. [10] studied the effects of geometrical parameters on the spray characteristics of PSA experimentally. They conducted a study to examine the effect of swirl chamber diameter to nozzle diameter ratio (D_s/D_o), length to diameter ratio of nozzle (L_o/D_o) and length to diameter ratio of swirl chamber (L_s/D_s) on the Sauter Mean Diameter (SMD) and SCA. They used a high-speed camera to measure the SCA and Malvern instruments to measure the SMD. They used water as test liquid

at injection pressure values of 0.8 MPa and 1.2 MPa and changed the D_s/D_o from 3 to 7.5, L_o/D_o from 0.81 to 2.69 and L_s/D_s from 1.25 to 5.

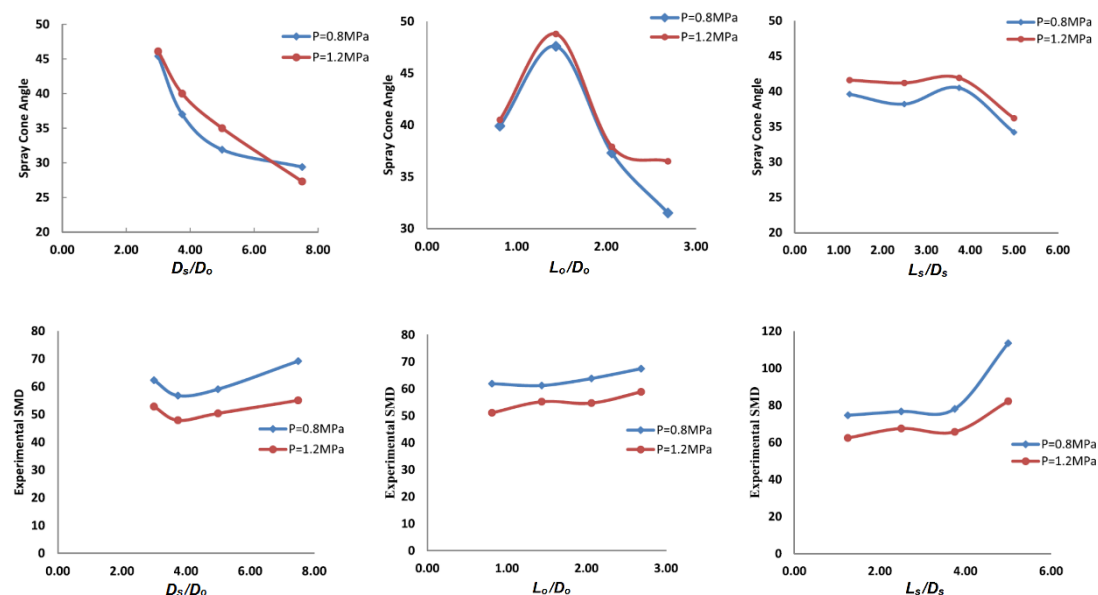


Figure 1.13. Geometrical Parameters Effects on SCA and SMD [10]

They obtained the following results which are given graphically in Figure 1.13:

- An increase in D_s/D_o leads to a decrease in SCA at both injection pressures. However, an increase in D_s/D_o from 3 to 3.75 causes a decrease in SMD and after that SMD continuously increases up to 7.5.
- An increase in L_o/D_o from 0.81 to 2.69 leads to an increase in SMD for both injection pressures. However, an optimum value of this ratio was found as 1.44 during the measurement of SCA. SCA increases with an increase in L_o/D_o up to optimal value and decreases after optimal value.
- A change in L_s/D_s between 1.25 and 3.75 does not considerably affect the SCA and SMD. However, an increase in this ratio from 3.75 to 5.0 causes a decrease in SCA and an increase in SMD.
- An increase in injection pressure results in a decrease in SMD and an improvement in the atomization quality.

Juan Liu et. al. [11] researched the geometrical parameters effect on the SCA and SMD experimentally and numerically. They studied the effects of three geometrical parameters such as D_s/D_o , L_o/D_o and divergent angle at the nozzle exit, Θ . They changed the D_s/D_o from 1.7 to 3.4, L_o/D_o from 1 to 9 and divergent angle Θ from 0° to 20° to study their effects on the hollow cone spray. They took photos with a camera (Canon Eos 40D) to measure the SCA, and used Malvern instruments to measure the SMD experimentally. They also performed numerical investigations with volume of fluid method. Both experimental and numerical investigations indicate that SCA decreases with increasing D_s/D_o , L_o/D_o and divergent angle Θ . On the contrary, increase in these parameters causes a decrease in SMD.

A. T. Sakman et. al. [12] made a numerical study to examine the nozzle geometry effects of the PSA on its performance. They examined the changes in liquid film thickness, SCA, and coefficient of discharge with the geometrical ratios of L_s/D_s , L_o/D_o and D_s/D_o using a computational model based on the arbitrary-Lagrangian-Eulerian method. This computational model was validated with experimental results. They investigated the effects of geometrical ratios using validated computational model with a constant mass flow rate through the nozzle and obtained the following results which are given graphically in Figure 1.14:

- D_s/D_o is the most effective parameter on the PSA performance.
- Increasing D_s/D_o results in a decrease in the discharge coefficient, SCA, liquid film thickness, but leads to an increase in the pressure drop in the nozzle.
- An increase in L_s/D_s , at its lower values, leads to an increase in the coefficient of discharge and liquid film thickness, while causes a slight reduction in SCA. At higher values of L_s/D_s , performance parameters become nearly constant.
- An increase in L_o/D_o , at its lower values, leads to a decrease in discharge coefficient, liquid film thickness, and SCA. At higher values of L_o/D_o , performance parameters become independent from the L_o/D_o .
- Total effect of the variation of L_o/D_o is more than that of L_s/D_s .

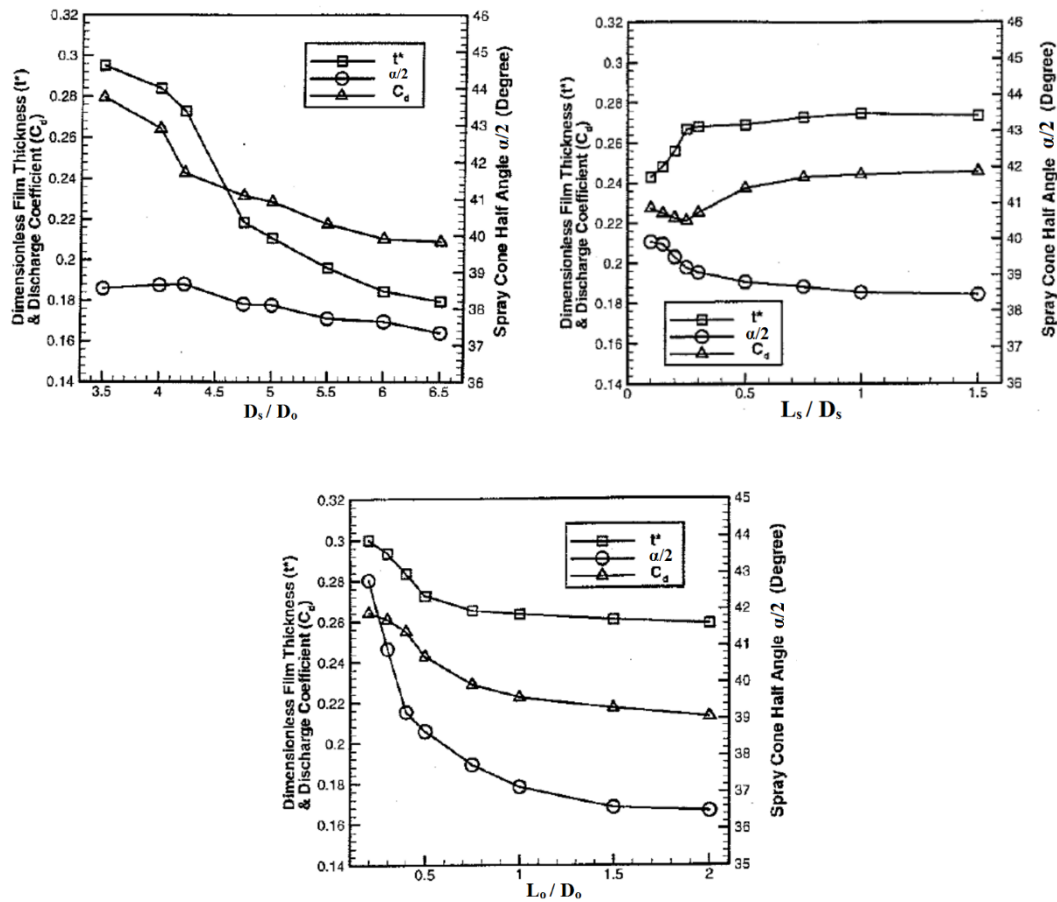


Figure 1.14. Effects of geometrical parameters of PSA on its performance [12]

J. Xue et. al. [13] performed a numerical study to investigate the effect of geometrical parameters on the flow in PSA. The effects of the atomizer constant ($K=A_p/(D_s.D_o)$), L_s/D_s , D_s/D_o , and L_o/D_o on the dimensionless liquid film thickness at the exit of the orifice ($t^*=t/(D_o/2)$), discharge coefficient, and half SCA are investigated with Arbitrary-Lagrangian-Eulerian method and they obtained the following results:

- Both discharge coefficient and dimensionless liquid film thickness at the orifice exit increase, and SCA decreases with increasing atomizer constant and L_s/D_s .
- An increase in L_o/D_o from 0.2 to 0.75 causes a decrease in t^* and t^* reaches the minimum value for $L_o/D_o=0.75$. After this point, t^* increases barely.

- Both discharge coefficient and SCA decrease with increasing L_o/D_o .
- Dimensionless liquid film thickness at the orifice exit decreases up to value of $D_s/D_o=4.5$, then increases.
- Coefficient of discharge decreases with increasing D_s/D_o and becomes nearly constant at larger values of D_s/D_o .
- SCA leads to decrease with increasing D_s/D_o .

The obtained results are depicted graphically in Figure 1.15.

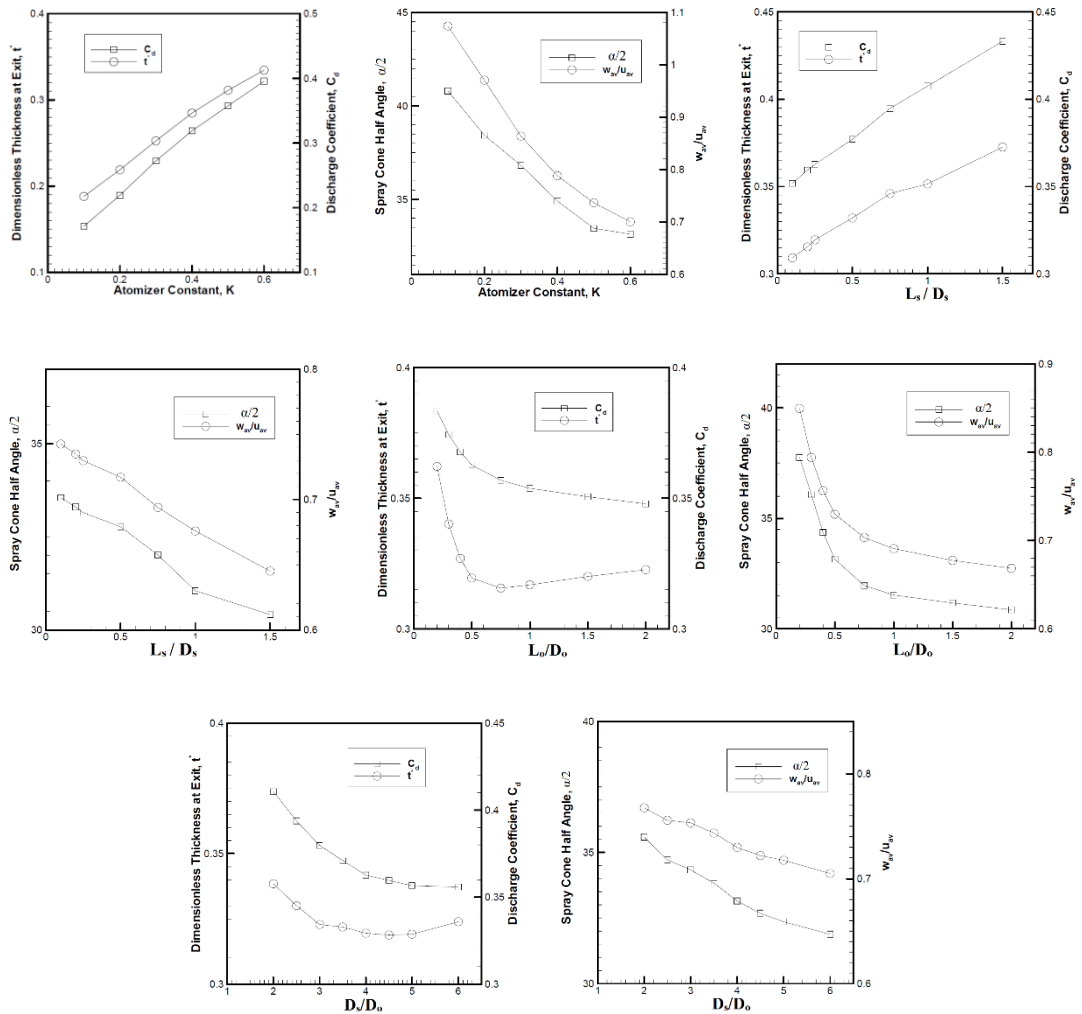


Figure 1.15. Effects of the atomizer constant, D_s/D_o , L_s/D_s , and L_o/D_o on the dimensionless liquid film thickness at the orifice exit, discharge coefficient, and half SCA [13]

S. K. Chen et. al. [14] investigated the effects of injection pressure, L_o/D_o , number of tangential ports (N_{tp}) and liquid viscosity on the SCA experimentally. Injection pressure was changed from 0.34 to 1.72 MPa, L_o/D_o was changed from 0.5 to 4, N_{tp} was changed from 1 to 3 (with constant total flow area) and finally liquid viscosity was changed from 0.001 to 0.012 kg/ms. In their study, a radial patternator is used to measure the SCA. After the study, they summarized the results below:

- A continuous increase in SCA is obtained with increasing injection pressure (Figure 1.16).
- Increase in L_o/D_o causes a decrease in SCA (Figure 1.16).
- Tangential port number has a small impact on SCA (Figure 1.16).
- Increase in liquid viscosity causes a decrease in SCA (Figure 1.16).

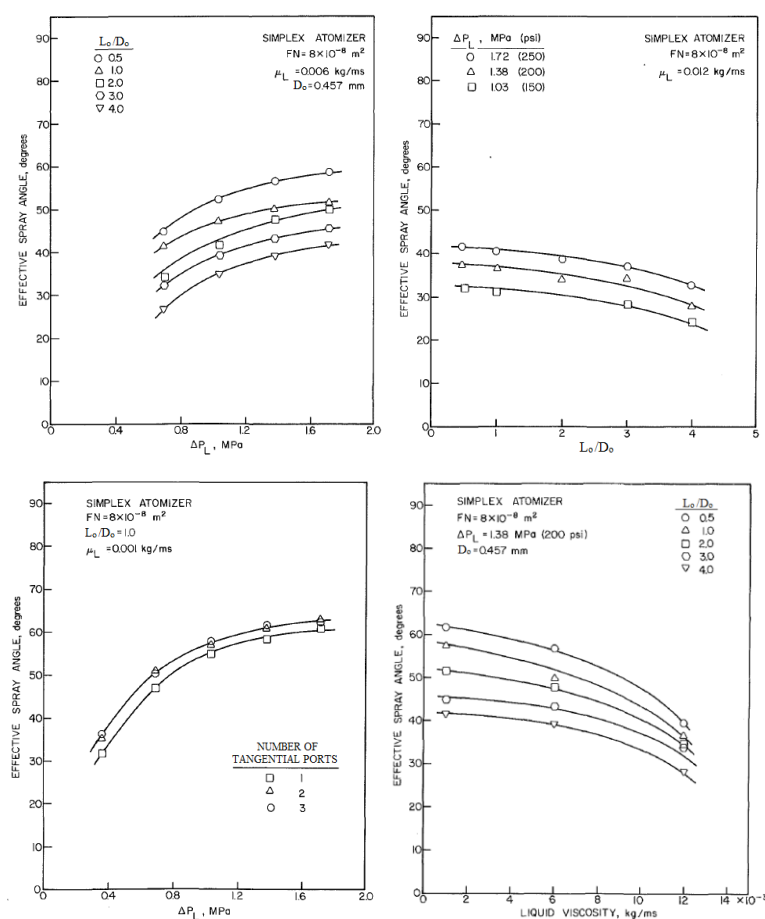


Figure 1.16. Effect of injection pressure, L_o/D_o , N_{tp} and liquid viscosity on SCA [14]

S.K. Som and S.G. Mukherjee [15] carried out theoretical and experimental studies to investigate the relationship between the geometric parameters and spray characteristics of PSA. They examine the effects of Reynolds number at the inlet (Re_i), D_o/D_s , L_s/D_s , and convergence angle, α on the discharge coefficient and SCA. They determined the discharge coefficient by measuring the flow rate of the nozzle and they measured the SCA using an angular scale. They concluded that:

- Discharge coefficient decreases with increasing Re_i . Decrease of discharge coefficient decreases more at lower Re_i values than the higher values.
- Discharge coefficient, at any constant Re_i , decreases with increasing D_o/D_s .
- Discharge coefficient, at any constant Re_i , increases with increasing L_s/D_s and decreasing convergence angle α .
- SCA slightly increases at a certain range of Re_i and then becomes independent from Re_i .
- Wider SCA is obtained with increasing D_o/D_s , α , and decreasing L_s/D_s .

A. Datta and S.K. Som [16] have made a numerical prediction of discharge coefficient, SCA, and air core diameter of PSA. They studied the flow rate, D_o , convergence angle (α), L_o and tangential port area and observed the following results:

- Increasing flow rate in nozzle, at its lower values, cause an increase in the SCA and air core diameter, but a decrease in discharge coefficient. At higher flow rates, these parameters become constant and independent from the flow rate.
- Increasing D_o results in an increase in air core diameter and SCA, but decrease in discharge coefficient.
- Increasing convergence angle leads to an increase in air core diameter and SCA, but decrease in discharge coefficient.
- Increasing tangential port area results in a decrease in SCA and air core diameter, but increase in discharge coefficient.
- There is no relationship between the L_o and these parameters.

Mohd Syazwan Firdaus Mat Rashid et. al. [17] researched the effect of tangential port number on the discharge coefficient and SCA at different injection pressure values varying from 2 to 8 bars. They changed the number of tangential ports from 2 to 5 and measured the SCA and the discharge coefficient. The flow rate was measured by a digital flow meter and a digital camera was used to capture images for SCA measurement. They observed that greater number of tangential ports results in higher discharge coefficient and wider SCA. Also, they obtained that higher injection pressure values causes lower coefficient of discharge and higher SCA. The obtained results are given in Figure 1.17.

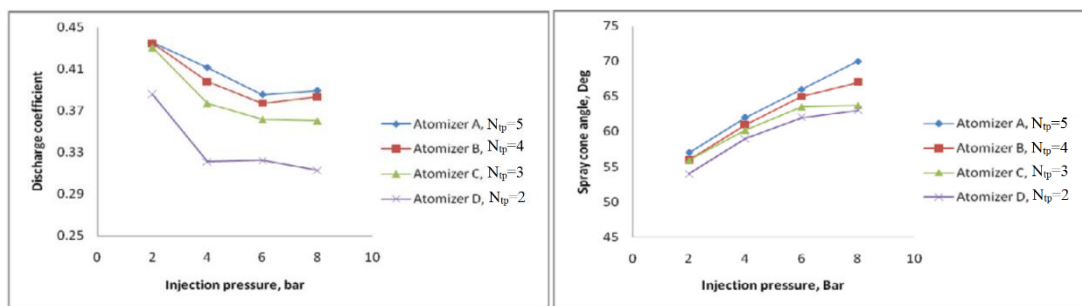


Figure 1.17. Effect of tangential port number and injection pressure on discharge coefficient and SCA [17]

Mohammad Reza Modarres-Razavi et. al. [18] examined the effects of geometrical parameters on coefficient of discharge and SCA numerically. They used volume of fluid method and investigated the effect of L_o/D_o , L_s/D_s and convergence angle on the performance of PSA. They changed L_o/D_o from 0.25 to 2, L_s/D_s from 0.1 to 2 and convergence angle from 30° to 90° . The numerical studies show that:

- A decrease in L_o/D_o leads to an increase in coefficient of discharge and SCA.
- An increase in L_s/D_s leads to an increase in coefficient of discharge and a decrease in SCA.
- An increase in convergence angle results in an increase in coefficient of discharge and a decrease in SCA.

- Optimal values of swirl chamber diameter, swirl chamber length, orifice diameter, orifice length and convergence angle are calculated as 9 mm, 6.75 mm, 3 mm, 3 mm and 60° , respectively.

Lin Yu-Jing et. al. [19] performed an experimental study to examine the effects of D_s , D_o and inlet pressure on the break-up length and the SCA. D_s was altered from 8 mm to 10 mm, D_o was altered from 2 mm to 2.5 mm and inlet pressure was changed from 0.0075 MPa to 0.5 MPa. They concluded that SCA increases with increasing injection pressure, D_s and D_o , and break-up length increases with increasing D_o and decreasing inlet pressure and D_s .

S. K. Chen et. al. [20] explored the effects of L_o/D_o on the SCA, SMD and droplet size distribution. They designed eight PSAs with L_o/D_o ratios ranging from 0.5 to 4. They used Malvern instrument to measure the mean drop sizes and a patternator to measure SCA. From measurements of spray, they obtained the results below:

- SCA declines with increasing L_o/D_o .
- The influence of L_o/D_o at lower injection pressure values is more evident, but loses its effect at higher injection pressures.
- Increasing L_o/D_o results in an increase in the uniformity of the drop size distribution in the spray.
- Increase in L_o/D_o from 0.5 to 2 leads to more uniform circumferential liquid distribution. On the contrary, an increasing from 2 to 4 has a negative effect on circumferential liquid distribution uniformity.

Xiao Wei and Huang Yong [21] established a correlation to estimate the SMD of PSA. The SMD correlations in the literature are given in Table 1.1. Most of these correlations, however, do not consider the effect of geometry on the droplet diameter. Unlike most correlations in the literature, they added the effects of three geometrical parameters, including tangential inlet, swirl chamber and nozzle diameters in their correlation given in Table 1.1.

Table 1.1. SMD Correlations [21]

References	SMD Correlation
Radcliffe [22]	$SMD = 7.3\sigma^{0.6}\mu_L^{0.2}\rho_L^{-0.2}m_L^{0.25}p_L^{-0.4}$
Jasuja [23]	$SMD = 4.4\sigma^{0.6}\mu_L^{0.16}\rho_L^{-0.16}m_L^{0.22}p_L^{-0.43}$
Ballester et. al. [24]	$SMD = 0.436\mu_L^{0.55}\rho_L^{-0.74}D_o^{-0.05}A_p^{-0.24}$
Lefebvre and Wang [25]	$SMD = 4.52(\sigma\mu_L^2/\rho_A p_L^2)^{0.25}(t \cos \alpha)^{0.25} + 0.39(\sigma\rho_L/\rho_A p_L)^{0.25}(t \cos \alpha)^{0.25}$
Couto et. al. [26]	$d_L = 0.9615 \cos \alpha \left(\frac{h_o^2 \sigma^2 \cos^2 \alpha}{\rho_A p_L U_o^4} \right)^{\frac{1}{6}} \left[1 + 2.6\mu_L \left(\frac{h_o^2 \rho_A^4 U_o^7}{72\rho_L^2 \sigma^5 \cos^8 \alpha} \right)^{\frac{1}{3}} \right]^{0.2}$
Xiao Wei and Huang Yong [21]	$SMD = C \left[\frac{K_p D_o (1 + \sqrt{X})}{(1 - X)} \right]^{1/2} \left[\frac{t^{1.17} (D_o - t)^{0.67}}{m_L^{0.67}} \right] \left(\frac{\sigma^2}{\rho_L \rho_A} \right)^{1/6}$

Additionally, they designed eighteen different PSAs and used these atomizers in the experiments to verify the improved semi-empirical model. Malvern instrument was used to measure the SMD experimentally. They used two different fluids (purified water and Jet A-1) to test the atomizer at different surface tensions and different injection pressures to obtain the effects of operating conditions. Their experiments showed that SMD increases with increasing tangential port area, increasing L_o/D_o and decreasing injection pressure as shown in Figure 1.18. After the experiments, they verified the semi-empirical correlation with the experimental results and the correlation uncertainty was calculated less than $\pm 20\%$ as given in Figure 1.19.

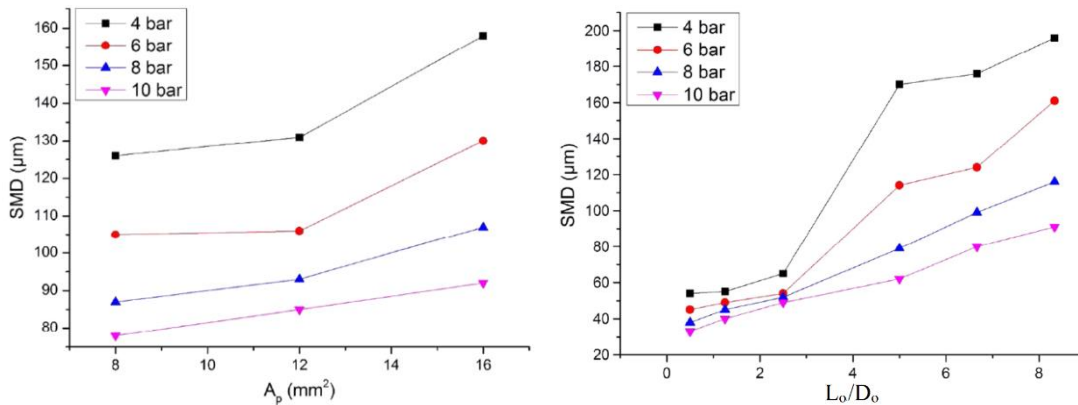


Figure 1.18. Effect of geometrical parameters on SMD [21]

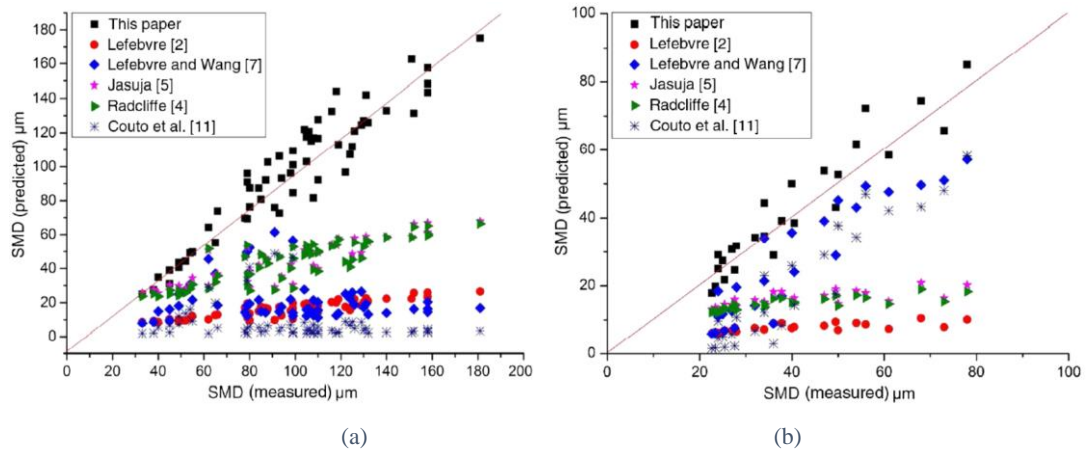


Figure 1.19. a) Comparison of measured SMD and predicted SMD for water
 b) Comparison of measured SMD and predicted SMD for Jet A-1 [21]

Yunjae Chung et. al. [27] carried out an experimental study in order to get information about the effect of swirl chamber diameter and length on the dynamic characteristics of PSA. The experimental studies show that:

- Decreasing swirl chamber diameter and increasing swirl chamber length increases the mass flow rate.
- Increasing length and decreasing diameter of swirl chamber result in smaller amplitude of mass flow rate pulsation.
- More stable combustion conditions are obtained with increasing length and decreasing diameter of swirl chamber.

The obtained results are demonstrated graphically in Figure 1.20.

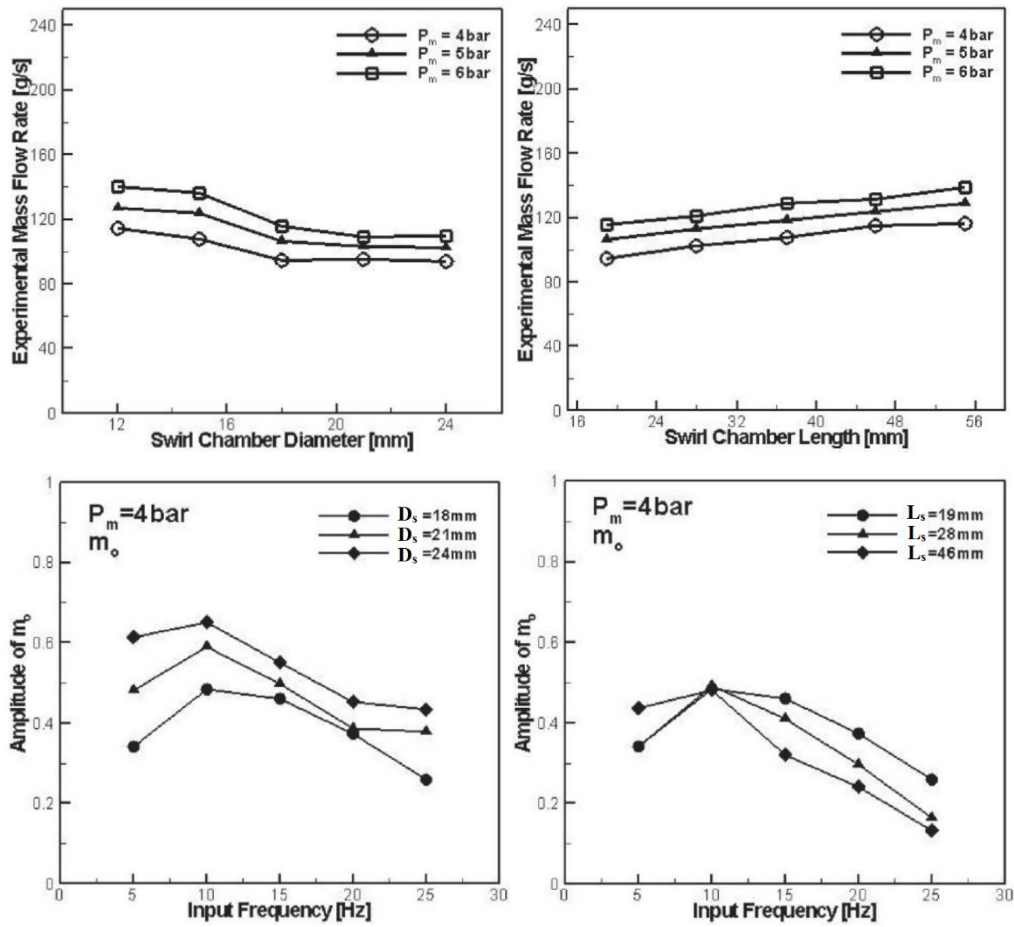


Figure 1.20. Effect of Varying Parameters on dynamic properties of PSA [27]

Chia-Chien Chu et. al. [28] performed an experimental study to explore the various parameters effects on PSA performance. Effects of D_0 and pressure on the SMD and SCA were investigated. Malvern instrument was used to measure the SMD experimentally. From the experiments, they obtained the following results:

- D_0 does not affect the droplet diameter directly for different tangential port areas.
- SCA is directly proportional to $D_0^{0.63}$ and increases with increasing D_0 .
- Pressure difference is the energy source of the system and one of the most effective parameters for the performance of atomizer. Droplet diameter reduces and SCA increases with increasing pressure drop.

Bülent Sümer [29] performed an experimental and numerical study in order to investigate the unsteady flows through the PSA. In the experimental investigations, he visualized the water flow inside the PSA and hollow cone spray by High Speed Shadowgraphy System. A powerful experimental method together with the image processing tool is developed in order to investigate the air core inside the PSA and macroscopic properties of hollow cone spray. Additionally, he used Phase Doppler Particle Analyzer in order to study the microscopic properties of hollow cone spray. Within the scope of the numerical studies, he performed 2D axisymmetric swirl and 3D flow simulations to investigate the two-phase flow through the PSA. At the end of the study, he obtained following results:

- Mean air core diameter increases with increasing mass flow rate but the shape of the air core diameter remains almost same for all mass flow rates.
- The measured SCAs change slightly with increasing mass flow rate.
- The obtained SMD distributions show that there are small droplets around the axis of the hollow cone spray and large droplets are located on the liquid jet.
- Increasing mass flow rate has a negligible effect on the SMD values.
- At the exit of the atomizer nozzle, a vortex formation is revealed and increasing mass flow rate moves the vortex towards the nozzle exit.
- Air core diameter is also obtained numerically and compared with experimental results. The comparison show that numerical results are in good agreement with experimental results.
- 2-D axisymmetric swirl simulations are sufficient in order to investigate the general flow features in a PSA.
- Both experimental and numerical investigations show that there are low and high frequency oscillations in the pressure/velocity field of the PSA. Low and high frequency oscillations are associated with the vortical structures dynamics in the water region and head end of the air core, respectively.

1.4. Content of the Thesis

In Chapter 1, LRE and atomizer types of LREs are introduced, research problem is defined, and literature survey about the research problem is presented.

In Chapter 2, experimental setup and measurement details are presented.

In Chapter 3, numerical study performed to examine the two-phase flow in the PSA is explained.

In Chapter 4, experimental results about the effect of geometrical parameters of PSA on the hollow cone spray are presented.

In Chapter 5, results of numerical simulations are presented.

In Chapter 6, experimental and numerical results are compared and obtained results are presented.

In Chapter 7, conclusions of the thesis are given.

1.5. Definitions

1.5.1. Arithmetic Mean Diameter

Droplet diameters of the particles passing through the probe volume can be summarized by mean droplet diameter. The mean droplet diameter is defined as arithmetic mean diameter ($D[1,0]$) is given below;

$$D[1,0] = \frac{\sum d}{n} \quad (1.2)$$

where d indicates the diameter of particles whilst n indicates the number of particles.

1.5.2. Sauter Mean Diameter

The Sauter Mean Diameter (SMD) is one of the most commonly used method for characterization of a spray which is also called surface-volume mean diameter. The SMD ($D[3,2]$) is given below;

$$D[3,2] = \frac{\sum d^3}{\sum d^2} \quad (1.3)$$

where d indicates the diameter of each particle.

The SMD is a frequently used value to specify the quality of spray in the heat and mass transfer applications [4]. In this thesis, the SMD is calculated so as to characterize the hollow cone spray of the atomizers.

1.5.3. Spray Cone Angle

The angle between the two edges of the spray is defined as Spray Cone Angle (SCA). A schematic of SCA is shown in Figure 1.21.

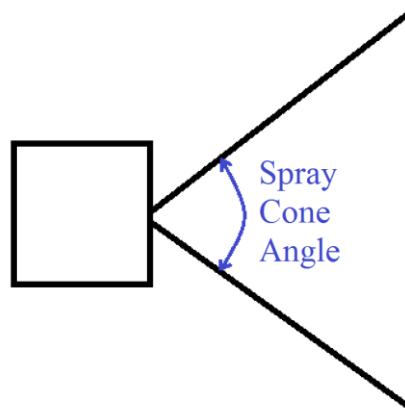


Figure 1.21. Spray Cone Angle

1.5.4. Breakup Length

The distance from the nozzle exit to the point at which rotating thin film begins to disintegrate into small droplets is defined as breakup length.

1.5.5. Discharge Coefficient

Discharge coefficient is explained as the ratio of actual and theoretical flow. The discharge coefficient is given below;

$$C_d = \frac{\dot{m}}{A_o(2\Delta P\rho)^{1/2}} \quad (1.4)$$

where \dot{m} indicates the mass flow rate, A_o indicates the cross-sectional area of nozzle orifice, ΔP indicates the pressure drop, and ρ indicates the density of liquid.

CHAPTER 2

EXPERIMENTAL SETUP & MEASUREMENT DETAILS

2.1. Introduction

The main objective of this thesis is to research the effect of geometrical parameters of PSA on the hollow cone spray experimentally. Experiments are performed with water in isothermal (non-reacting) and atmospheric pressure conditions because these indicated conditions reduce the complexity and increase the safety level of tests.

2.2. Experimental Setup

The experimental studies are carried out at the single element atmospheric cold flow experimental facility of TÜBİTAK SAGE. A schematic and a general view of the experimental setup are illustrated in Figure 2.1 and Figure 2.2, respectively.

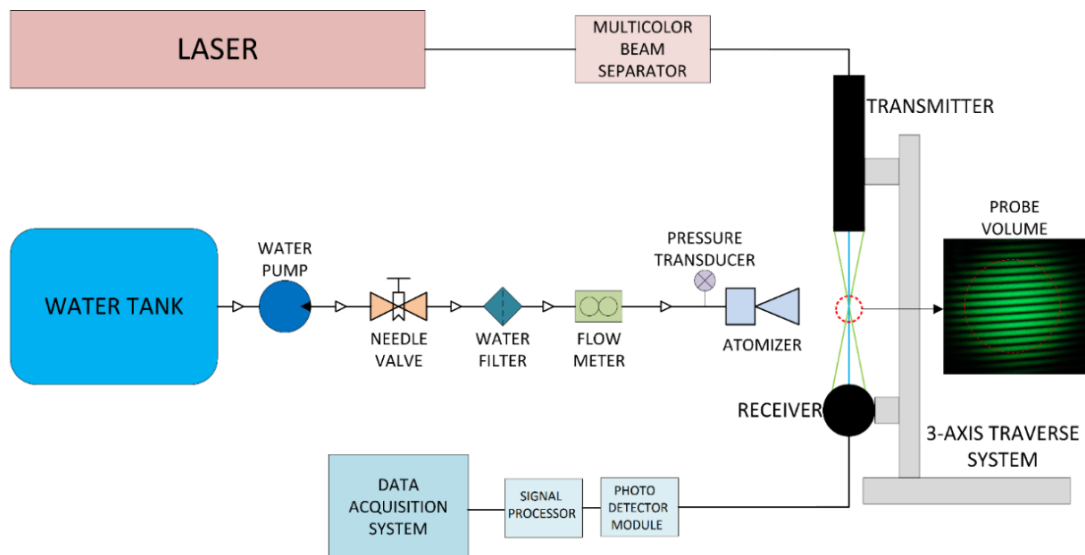


Figure 2.1. A Schematic of the Experimental Facility

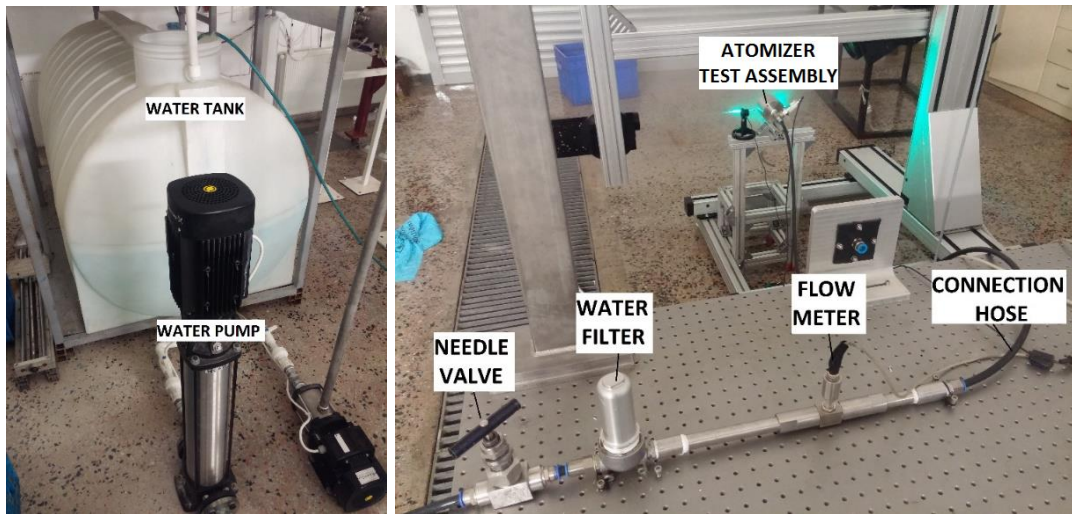


Figure 2.2. Experimental Facility

The experimental facility contains a 1 m³ water tank and a water pump at the water tank exit. The water pump takes the water from the tank and feeds it to the atomizer test assembly. Between the water pump and atomizer test assembly, the test facility includes a needle valve which controls the water flow rate, a water filter which decontaminates the water, a turbine type flow meter which measures the volume flow rate of water and connection hose which transfer the water to the atomizer test assembly.

Before each test, the water temperature is measured and it is in between 18 and 23 °C.

2.3. Atomizer Test Assembly

2.3.1. Introduction

In this section, a design study is carried out for the atomizer test assembly. Designed atomizer test assembly consists of a PSA, a blind plug, a reservoir, a cap, two O-rings, and bolts. Mechanical design of the atomizer test assembly is shown in Figure 2.3. The design of the atomizer test assembly allows testing atomizers with different geometrical parameters.

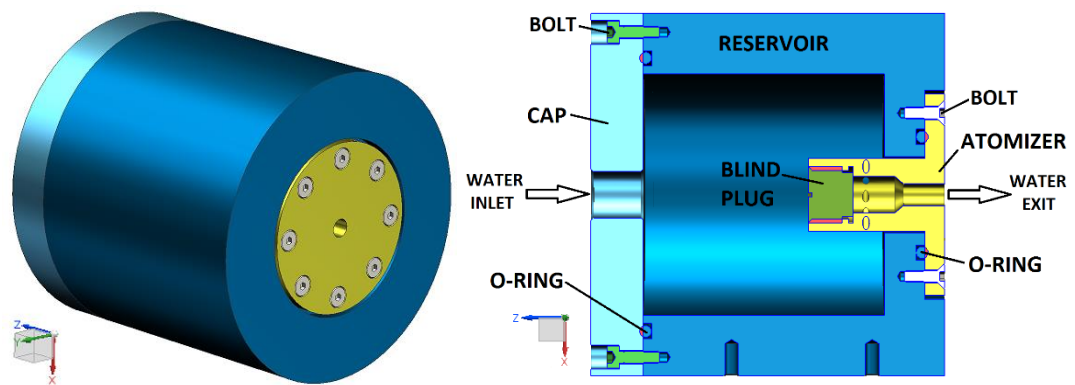


Figure 2.3. Mechanical Design of Atomizer Test Assembly

The atomizer is designed according to the geometrical parameters and the hole opened during the manufacturing of the atomizer body is closed with the blind plug. The distance from the inner face of the blind plug to the tangential inlet ports are the same for all tested atomizers. The reservoir is designed to feed the tangential ports of the PSA uniformly. The atomizer is connected to the reservoir with eight bolts. By using these bolts, test atomizers of different geometrical parameters are assembled into the reservoir. Between the reservoir and the atomizer, an O-ring is used in order to prevent the leakage. A cap is designed to close the reservoir and water flows into the reservoir through a hole placed on the cap. The cap is connected to the reservoir with eight bolts and an O-ring is used to prevent the leakage between the cap and reservoir.

Water is fed to the atomizer test assembly with a hose, which is connected to the cap. The reservoir is filled with water through the hole on the cap and the water is transferred to the tangential ports of atomizer via the reservoir. Water passes through the tangential ports, flows through the atomizer and exits from the nozzle of the atomizer as a hollow cone spray.

2.3.2. Pressure Swirl Atomizer

The technical drawing of the baseline PSA is given in Figure 2.4. The baseline PSA has the same geometric properties as the inner oxidizer atomizer of the bi-propellant injector used in the RD-0110 rocket engine [9].

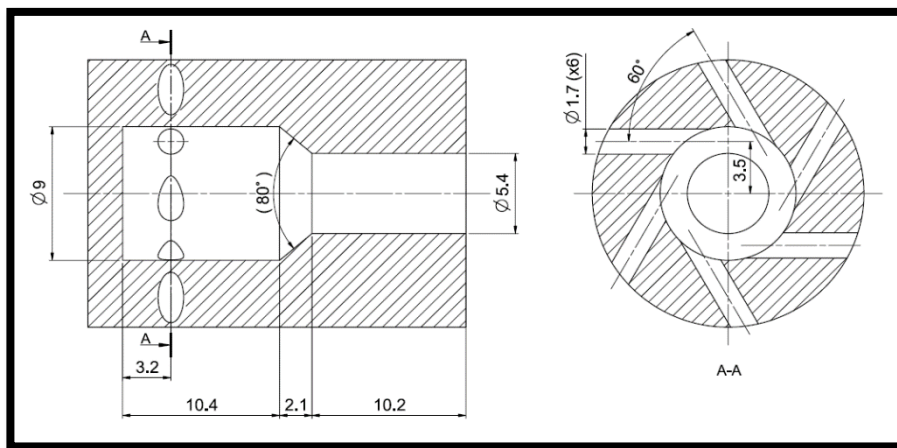


Figure 2.4. The technical drawing of the baseline PSA

The length of nozzle, swirl chamber and the atomizer are 10.2 mm, 10.4 mm and 22.75 mm, respectively. The nozzle and swirl chamber diameters are 5.4 mm and 9 mm, respectively. Water enters the swirl chamber through six tangential ports whose diameters are 1.7 mm.

In the present experimental study, effects of the nozzle diameter, number of tangential ports and nozzle length on the hollow cone spray are examined for varying mass flow rates. Other geometrical parameters except the changed one are kept constant. For the experimental study, seven test atomizers are determined and the geometrical parameters of these atomizers are given in Table 2.1. When designing the A-4 and A-5, total tangential port inlet area is kept the same as the A-1 (Baseline PSA), and only the number of tangential ports is changed.

Table 2.1. Selected Test Atomizers

	Dimensional Parameters						Non-Dimensional Parameters		
	D_s [mm]	L_s [mm]	D_o [mm]	L_o [mm]	D_{tp} [mm]	N_{tp}	L_o/D_o	L_s/D_s	D_s/D_o
A-1 (BASELINE)	9	10.4	5.4	10.2	1.7	6	1.89	1.16	1.67
A-2	9	10.4	4.1	10.2	1.7	6	2.49	1.16	2.20
A-3	9	10.4	6.8	10.2	1.7	6	1.50	1.16	1.32
A-4	9	10.4	5.4	10.2	1.7	4	1.89	1.16	1.67
A-5	9	10.4	5.4	10.2	1.7	2	1.89	1.16	1.67
A-6	9	10.4	5.4	8.1	1.7	6	1.50	1.16	1.67
A-7	9	10.4	5.4	13.5	1.7	6	2.50	1.16	1.67

All of the test atomizers are manufactured from stainless steel by machining. After manufacturing, dimensional quality controls of all atomizers are performed and obtained results show that atomizers are manufactured in right dimensions. A sample manufactured PSA is shown in Figure 2.5.



Figure 2.5. A Sample Manufactured PSA

2.3.3. Reservoir

2.3.3.1. Introduction

The reservoir is designed to feed the tangential ports of the PSA with water. A properly designed reservoir shall distribute the water equally to the tangential ports. In this section, a numerical study is performed in order to examine the distribution of water to the tangential ports and check the reservoir design using Flow-3D software. Detailed information about the Flow-3D software is given in Section 2.3.3.2.

2.3.3.2. Verification of Reservoir Design

In order to investigate the distribution of water to the tangential ports and check the reservoir design, a numerical study is carried out using Flow-3D software. Flow-3D software uses a simple grid of rectangular elements, so grid generation is relatively easy [30]. Besides that, this software has improved numerical accuracy, saves solution times, and requires very little memory storage [30]. Firstly, a simple model of the atomizer test assembly is generated and imported to the software. Then, boundary conditions are determined. Mass flow inlet is selected as left-hand side of the simulation domain and pressure outlet is selected as the nozzle exit. Simple model of the atomizer test assembly and boundary conditions are demonstrated in Figure 2.6.

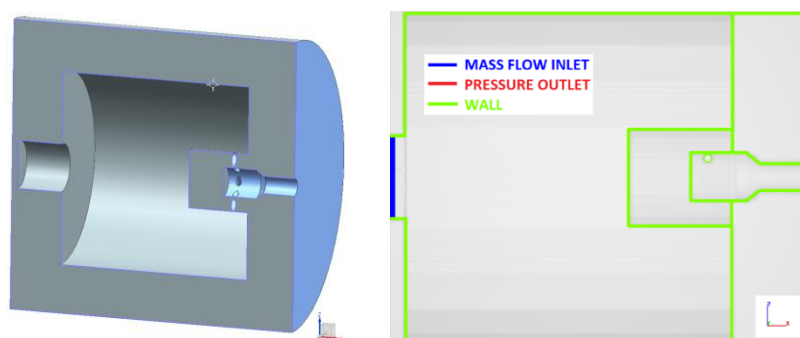


Figure 2.6. Simple Analysis Model and Boundary Conditions

Finally, the average water mass flow rates through the reservoir inlet and tangential ports of the atomizer are calculated. The internal flow of the reservoir is defined by the equations given in Section 3.2 (Equation (3.1), Equation (3.2), and Equation (3.3)).

Grid resolution is an important parameter in the modeling of reservoir and investigation of the water distribution in tangential ports. In order to model the reservoir correctly, four different grids are generated and shown together in Figure 2.7. Each grid consists of two mesh blocks. The use of two mesh blocks provides local refinement in interest areas and remarkably decreases computational resources required for a given simulation [30]. Tangential inlet ports of the atomizer are so small compared to the reservoir size, therefore the region close to the atomizer is modeled using Mesh Block 2 which has a higher resolution than Mesh Block 1. Two mesh blocks of computational domain are shown in Figure 2.8. In order to generate the four grids, the number of cells is increased by keeping the cell size ratios between the mesh blocks constant.

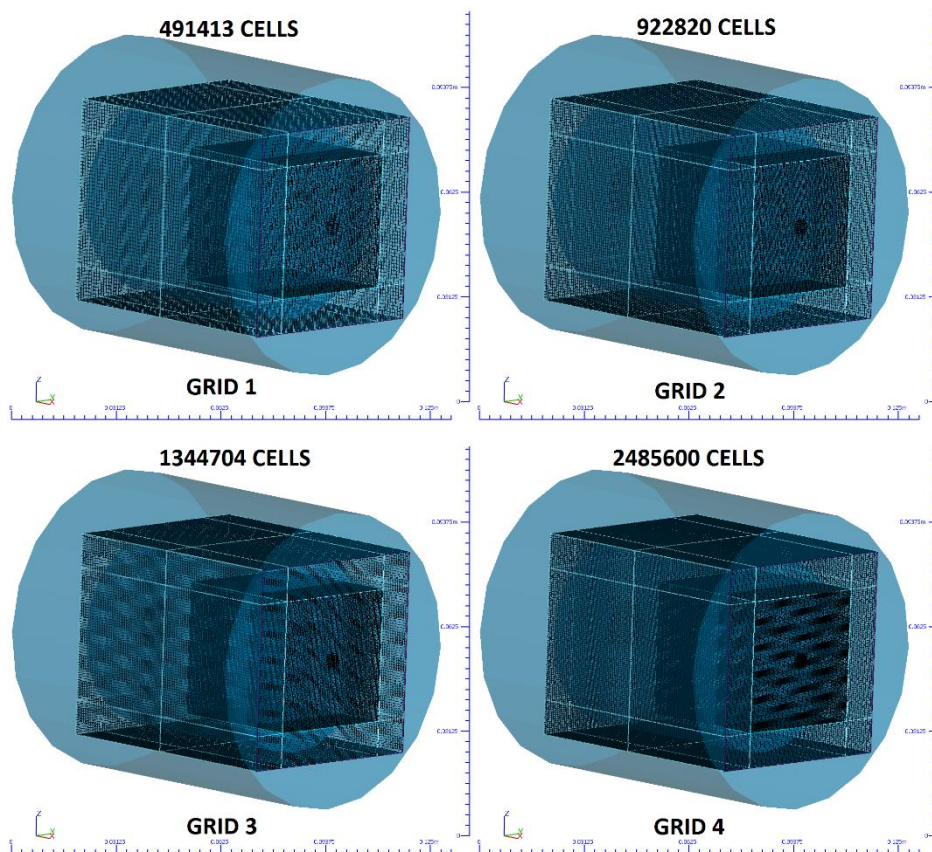


Figure 2.7. Generated Four Grids

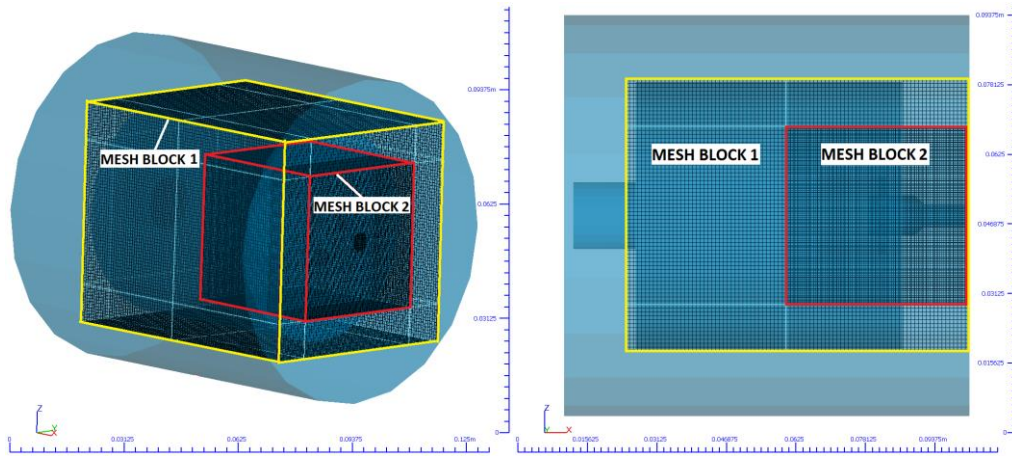


Figure 2.8. Mesh Blocks of Computational Domain

In order to examine the modelling of tangential ports for each grid, render mode of the software is used. The render mode demonstrates how the tangential ports appear with the selected grid. The render mode is run for four different grids and obtained images are given in Figure 2.9 and Figure 2.10.

As shown in Figure 2.9 and Figure 2.10, the tangential ports cannot be correctly modeled due to the low grid resolution for GRID1. On the contrary, it is seen that the resolutions of the GRID2, GRID3 and GRID4 are sufficient for modelling of tangential ports. In order to obtain more accurate results, numerical simulations are performed using GRID4.

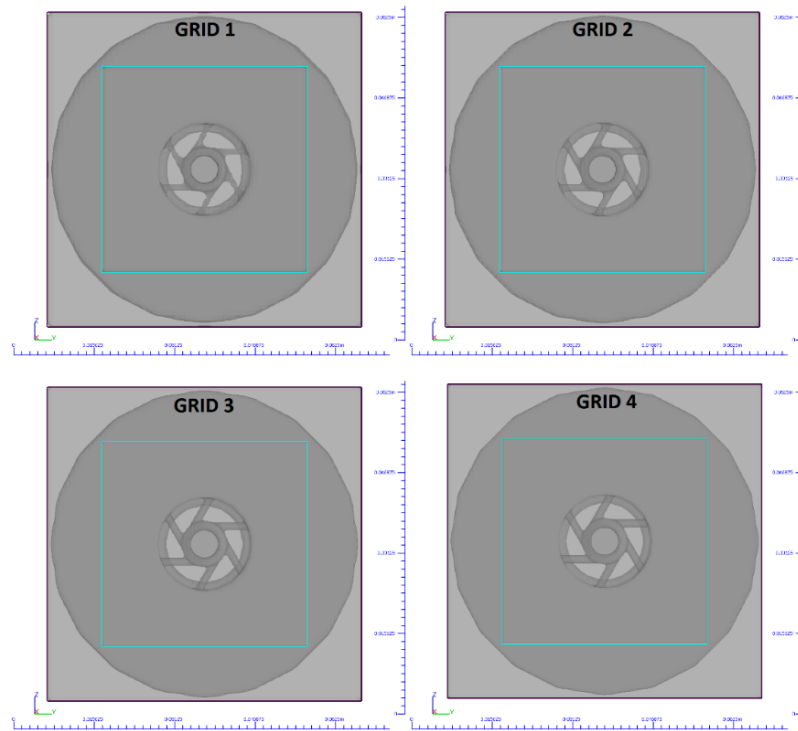


Figure 2.9. Tangential Ports with Render Mode for Computational Domains

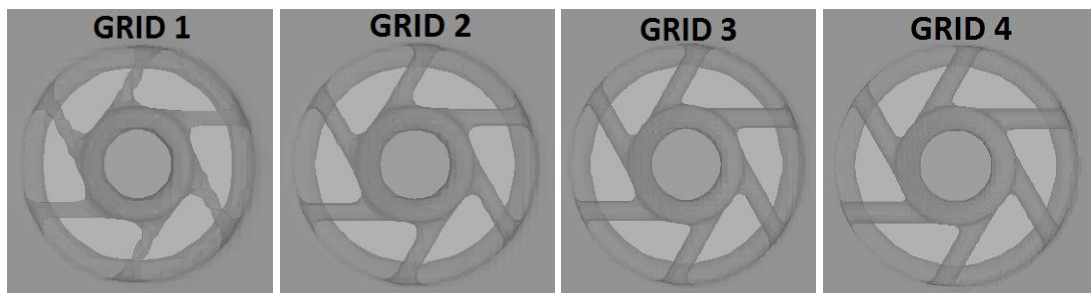


Figure 2.10. Close View of Tangential Ports with Render Mode for Computational Domains

2.3.3.3. Simulation Results

In order to verify the reservoir design, numerical simulations are performed in this section and the calculated mass flow rate of water passing through the inlet of the reservoir and the tangential ports are given in Table 2.2. Reference value in Table 2.2 is calculated by dividing the mass flow rate of reservoir inlet by the number of the tangential ports.

Table 2.2. Mass Flow Rates at Measurement Locations

	Reservoir Inlet Mean MFR [kg/s]	Reference MFR [kg/s]	TP1 Mean MFR [kg/s]	TP2 Mean MFR [kg/s]	TP3 Mean MFR [kg/s]	TP4 Mean MFR [kg/s]	TP5 Mean MFR [kg/s]	TP6 Mean MFR [kg/s]
GRID 4	0.173	0.02883	0.02919	0.02864	0.02880	0.02882	0.02876	0.02886

Deviation calculations are done for each tangential port using the mass flow rate values given in Table 2.2 and results are given in Table 2.3. Deviation of the mass flow rate of water through each tangential port from the reference mass flow rate value is calculated using Equation (2.1).

$$D \% = \frac{|Reference\ MFR - Mean\ MFR\ at\ Tangential\ Port|}{Reference\ MFR} \times 100 \quad (2.1)$$

Table 2.3. Calculated Deviations for Tangential Ports

	TP1 Deviation %	TP2 Deviation %	TP3 Deviation %	TP4 Deviation %	TP5 Deviation %	TP6 Deviation %
GRID4	1.21	0.72	0.16	0.09	0.29	0.07

2.3.3.4. Conclusion

A numerical study is performed to check the reservoir design by using Flow-3D software. Four different computational domains are formed and tangential port models are examined for all domains. GRID1 is not a true domain to model the tangential ports, but GRID2, GRID3 and GRID4 have enough grid resolution for modeling. In order to obtain more accurate results, GRID4 is selected for numerical simulations. The simulation results show that the maximum deviation of mass flow rates of tangential ports from the reference value is 1.21% for GRID4. This deviation value is considered acceptable and reservoir design is proper to distribute the water equally to the tangential ports.

2.4. Experimental Method

2.4.1. High Speed Shadowgraphy System

High Speed Shadowgraphy System (HSSS) is used to examine the hollow cone spray. A Photron SA-X2 type high speed camera is preferred for the visualization. The settings of high-speed camera are given in Table 2.4.

Table 2.4. *Settings of High-Speed Camera for SCA Measurement.*

Parameter	Setting
Image Recording Rate	20000 fps
Recording Time	500 ms
Width of Image	784 pixels
Height of Image	880 pixels

The captured image of the hollow cone spray is given in Figure 2.11. The captured image shows that the edges of the hollow cone spray are darker than the other regions. The angle between the edges can be calculated by finding out the two edges of the spray and measuring the distance between them. It can also be seen from Figure 2.11 that rotating thin film disintegrates into small droplets after a certain distance from the nozzle exit. The distance of disintegration can be measured using captured images.

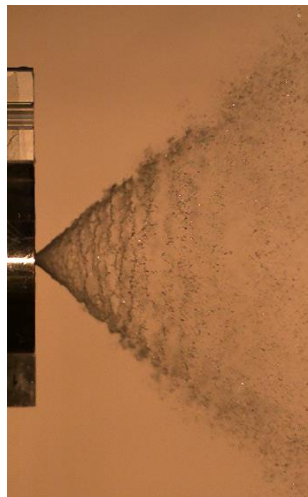


Figure 2.11. Captured Images of the Hollow Cone Spray

2.4.1.1. Image Processing

In order to detect the edges of captured images and measure the distance between the edges, an image processing code which is written in MATLAB, of which details are given in [29], is used. By using this program, the spray images obtained by high speed camera are firstly converted to gray scale images, then Sobel edge detector is applied to the images and finally intensity distribution on a line positioned perpendicular to the centerline of the atomizer is computed for processed images. A sample image obtained by the application of Sobel edge detector is given in Figure 2.12.

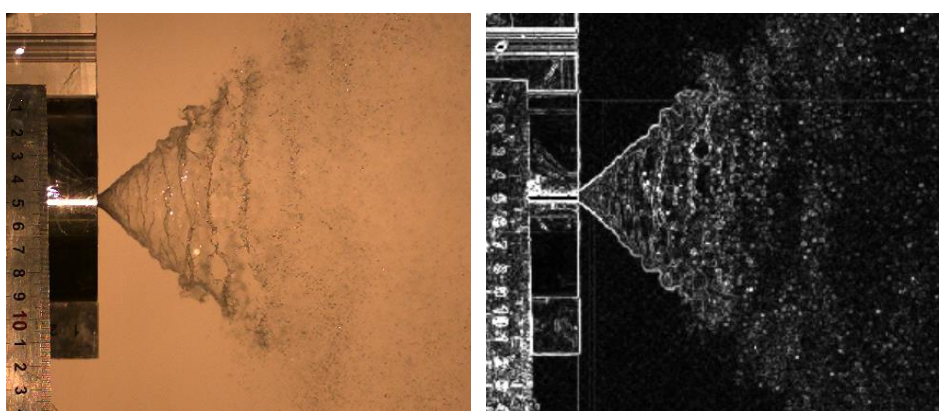


Figure 2.12. Application of Sobel Edge Detector

The sample intensity distribution on a line positioned perpendicular to the atomizer centerline is given in Figure 2.13.

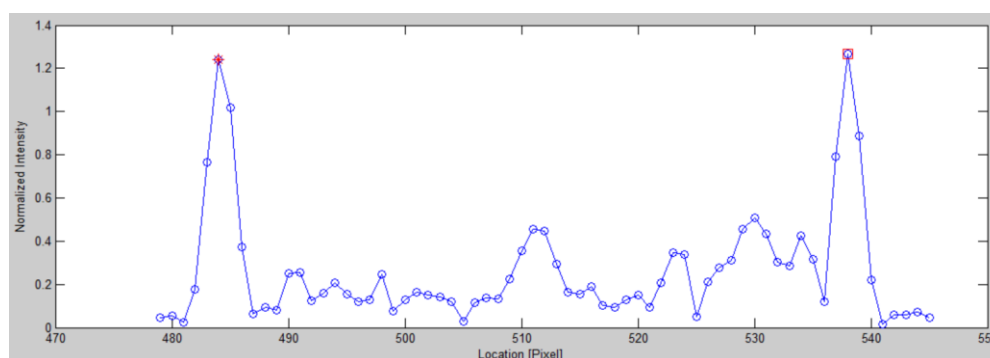


Figure 2.13. Intensity Distribution on a Line at $x=275$ pixel

As shown in Figure 2.13, the intensity reaches the first peak value at 484 pixels and second peak value at 538 pixels. The length between two peaks is calculated as 54 pixels, which is the distance between two edges of hollow cone spray on the positioned line. The measurement of the distance between two edges is ± 1 pixel uncertainty level.

2.4.1.2. Pixel Coordinates Conversion to Physical Coordinates

The length between two edges of the hollow cone spray and the distance of disintegration are defined in pixel coordinates. In order to convert the measured distances in pixel coordinates to distance in physical coordinates, two rulers are used as demonstrated in Figure 2.14.

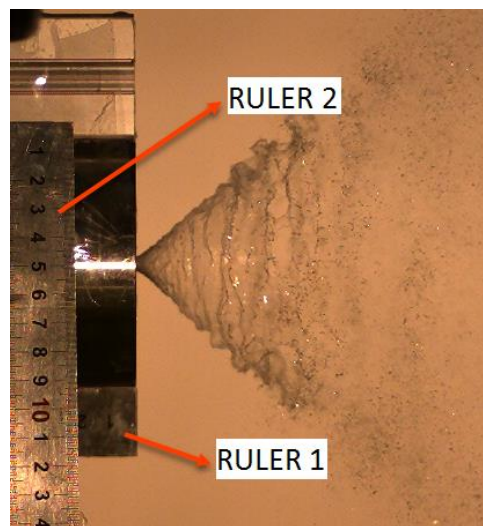


Figure 2.14. Position of Rulers

The effective area of the obtained images with high speed camera is 784x880 pixels. Using the Ruler 1, the distance between two pixels in horizontal axis is measured as mm. To measure the distance between two pixels in vertical axis as mm, Ruler 2 is used. By this method, pixel coordinates of the effective image area are converted to physical coordinates.

2.4.2. Phase Doppler Particle Analyzer

TSI two-component Phase Doppler Particle Analyzer (PDPA) system is used in experimental study to measure the velocity and the size of the particles . A schematic view of the PDPA system is illustrated in Figure 2.15.

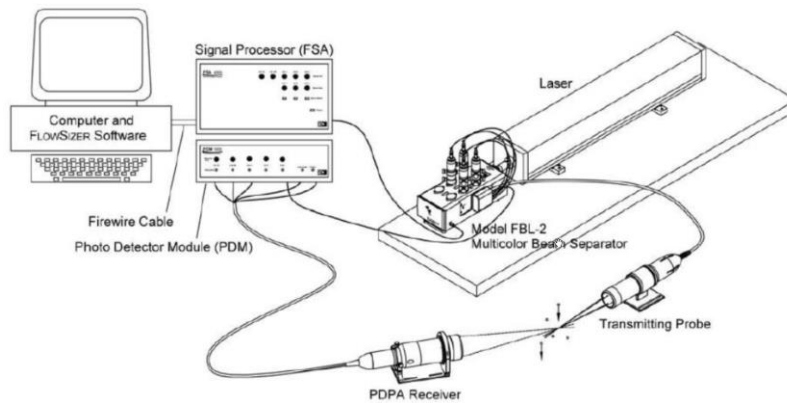


Figure 2.15. A Schematic of TSI Two-Component PDPA System [31]

PDPA system consists of a 5 Watt Argon-Ion Laser, a Multicolor Beam Separator, a Transmitter, a Receiver, a Photo Detector Module, a Signal Processor, a Computer Software and a Power Meter. Major components of PDPA are illustrated in Figure 2.16.

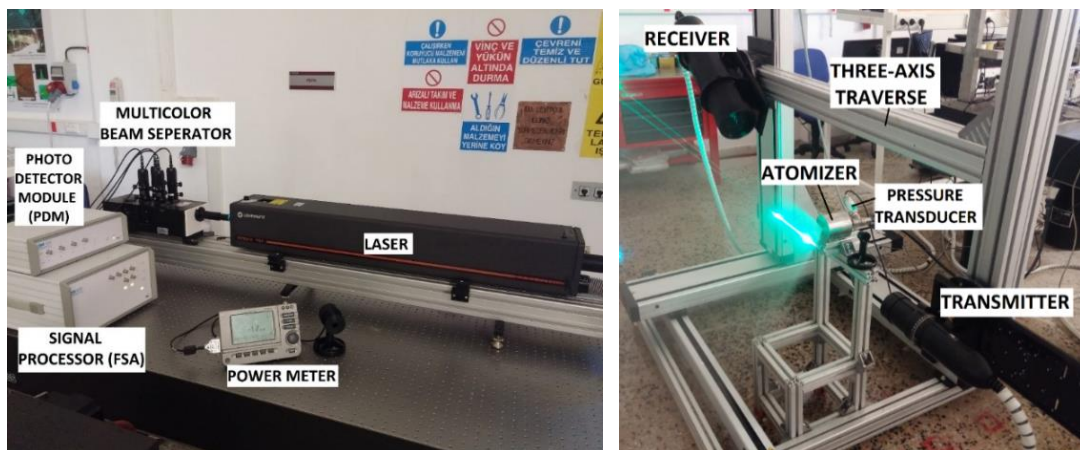


Figure 2.16. TSI Two-Component PDPA System in Facility

5 Watt Argon-Ion Laser (Coherent Innova 70-5) generates multiline blue/green laser beam and transmits it to the Multicolor Beam Separator.

Multicolor Beam Separator receives the multiline laser and first separates it into two colors, green ($\lambda=514.5$ nm) and blue ($\lambda=488$ nm). Then, both green and blue laser beams are separated into two laser beams (unshifted and shifted) by optics inside the Multicolor Beam Separator.

Transmitter takes the shifted and unshifted green/blue laser beams from the Multicolor Beam Separator and transmits it to the experimental area. The crossing of shifted and unshifted laser beams creates the probe volume. Probe Volume is a measurement region consisting of bright and dark fringes as shown in Figure 2.17. Particles passing through the probe volume scatter light at bright fringe and no light at dark fringe. The particle scatters light with a frequency proportional to its velocity in probe volume. Mentioned frequency is called as the Doppler shift frequency. PDPA use the Doppler shift frequency to measure the particle velocity. Probe volume of green laser beams is used to measure the axial velocity and the droplet size of the particles. Probe volume of blue laser beams is used to measure the radial velocity of the particles.

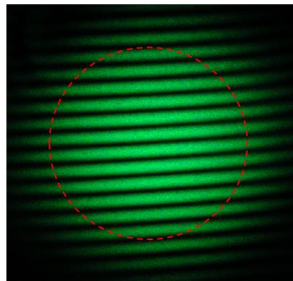


Figure 2.17. Probe Volume [32]

Particles passing through the probe volume scatter light. Receiver collects reflection and refraction waves coming from the particles and transfers them to the Photo Detector Module.

Photo Detector Module converts the transmitted waves to electrical signal (voltage). Signal Processor filters the electrical signal and sends the filtered data to the computer. Computer software collects the data and presents to the user. Power Meter measures the power of the green/blue laser beam.

The receiver and the transmitter are placed on a remote controlled traverse system to scan the spray in three axes as shown in Figure 2.16.

2.4.2.1. Verification of PDPA System Measurement

2.4.2.1.1. Verification of Droplet Size Measurement

A device called Monosize Droplet Generator (MDG) is used to verify the droplet size measurements and determine the accuracy for PDPA System,. A schematic of MDG is illustrated in Figure 2.18.

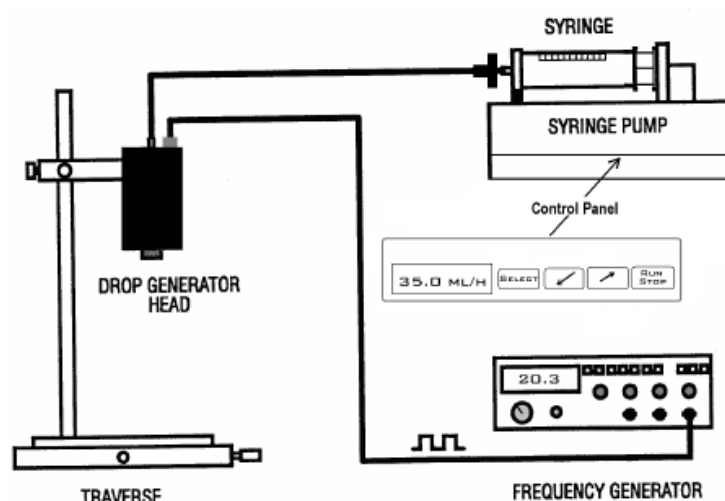


Figure 2.18. Monosize Droplet Generator [33]

The MDG mainly consists of a drop generator head, a syringe, a syringe pump, a frequency generator, and a traverse. Drop generator head has a liquid reservoir, piezoelectric crystals, and an orifice. The liquid reservoir of the drop generator is fed with water via a syringe. Water is forced out of the syringe at a constant rate using a

syringe pump. A frequency generator is used to drive the piezoelectric crystals in the drop generator head and break up the water stream into droplets of identical size. A general view of the MDG is given in Figure 2.19.

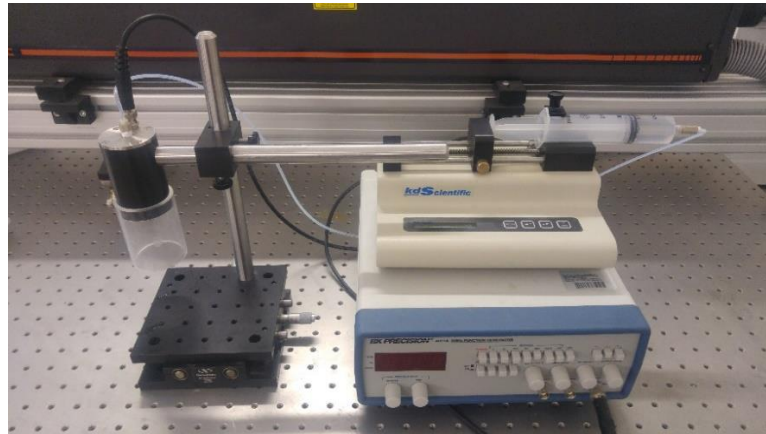


Figure 2.19. A general view of MDG

The liquid reservoir of the MDG supply a laminar jet. The MDG applies periodic excitation to the liquid reservoir and the laminar jet breaks up when the excitation frequency is equal to a resonant frequency. As a result of that, the MDG forms uniform droplets. By using the flow rate and the excitation frequency values, droplets size is calculated by using the equation below;

$$D = 317 \left[\frac{Q}{f} \right]^{1/3} \quad (2.2)$$

where D indicates the diameter of droplet (μm), Q indicates the liquid flow rate (cc/s) and f indicates the excitation frequency (kHz).

The MDG is used with three different orifices which have 20 μm , 50 μm , and 100 μm diameter. Recommended flow rates and excitation frequency values for these orifices are given in the user manual of the MDG. The 20 μm orifice is used for a flow rate of

35 ml/hr and excitation frequency range from 30 to 110 kHz, the 50 μm orifice is used for a flow rate of 66 ml/hr and excitation frequency range from 5 to 25 kHz, and the 100 μm orifice is used for a flow rate of 133 ml/hr and excitation frequency range from 5 to 15 kHz [33].

In the experiment, MDG is set to flow rates and excitation frequencies which are given in Table 2.5, and theoretical droplet diameters are calculated using Equation (2.2). Then, the droplet diameter for each case is measured three times with PDPA system, and results are given in Table 2.5. The obtained results indicate that uncertainty of the diameter measurement is less than 5%.

Table 2.5. Comparison of Theoretical Values and MDG Measurement Results.

Orifice Diameter [μm]	Flow Rate [ml/hr]	Excitation Frequency [kHz]	Theoretical Diameter [μm]	Measured Diameter [μm]			Max. Error %
				1	2	3	
20	35	105.80	56.0019	53.9124	55.1668	55.3444	3.73
	35	54.17	70.0022	68.1376	72.7757	67.5654	3.96
	35	30.25	85.0073	88.0144	84.9812	88.2216	3.78
50	66	24.94	112.0017	111.0104	112.8384	111.8548	0.89
	66	19.52	121.5337	118.3156	118.9121	116.6588	4.01
	66	15.94	130.0252	128.2233	133.7363	129.4123	2.29
	66	10.38	150.0114	154.4713	154.0111	153.2730	2.97
	66	6.00	180.0831	186.7321	186.6676	187.6812	4.22
100	133	8.82	200.0491	203.7867	200.0354	199.3231	1.87
	133	6.63	220.0163	226.6291	228.1814	228.2882	3.76
	133	5.10	240.1242	244.9881	245.3342	243.9323	2.17

2.4.2.1.2. Verification of Velocity Measurement

In order to verify the velocity measurements and determine the accuracy for PDPA System, the MDG is used again. The MDG generates droplets with a constant velocity. Firstly, actual velocity of the droplets is measured using HSSS as shown in Figure 2.20. Secondly, velocity of droplets is measured with PDPA system. Then, measured velocity is compared with actual velocity and uncertainty of velocity measurement is calculated.

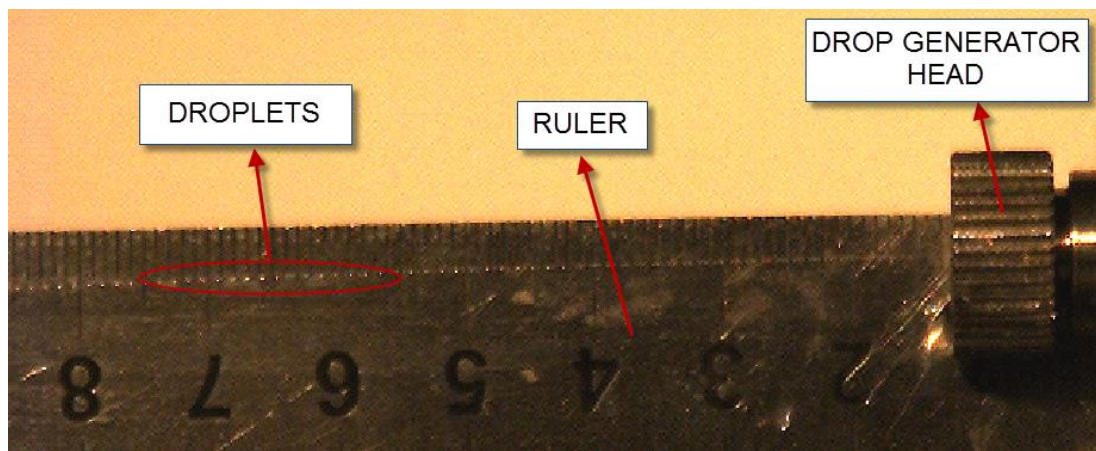


Figure 2.20. Velocity Measurement with HSSS

In order to measure the actual velocity of droplets, a droplet is marked and tracked in successive images visually. The distance taken by droplets in certain time periods is observed by ruler, and actual velocity is calculated using Equation (2.3).

$$V_{\text{act}} = \frac{\Delta x}{\Delta t} \quad (2.3)$$

where V_{act} is the actual velocity of droplets, x is the distance taken by droplets, and t is the time period.

Droplet velocity is measured for 100 μm orifice diameter and results are given in Table 2.6. Recommended mass flow rate in user manual are adjusted for the orifice diameter.

A sample of actual velocity calculation for orifice diameter of 100 μm is given in Figure 2.21. The marked droplet is at $x=70\text{ mm}$ at $t=0.021775\text{ s}$ and at $x=75\text{ mm}$ at $t=0.022600\text{ s}$. The marked droplet moves 5 mm in a time period of $8.25 \times 10^{-4}\text{ s}$ and actual velocity of droplet is calculated as 6.06 m/s.

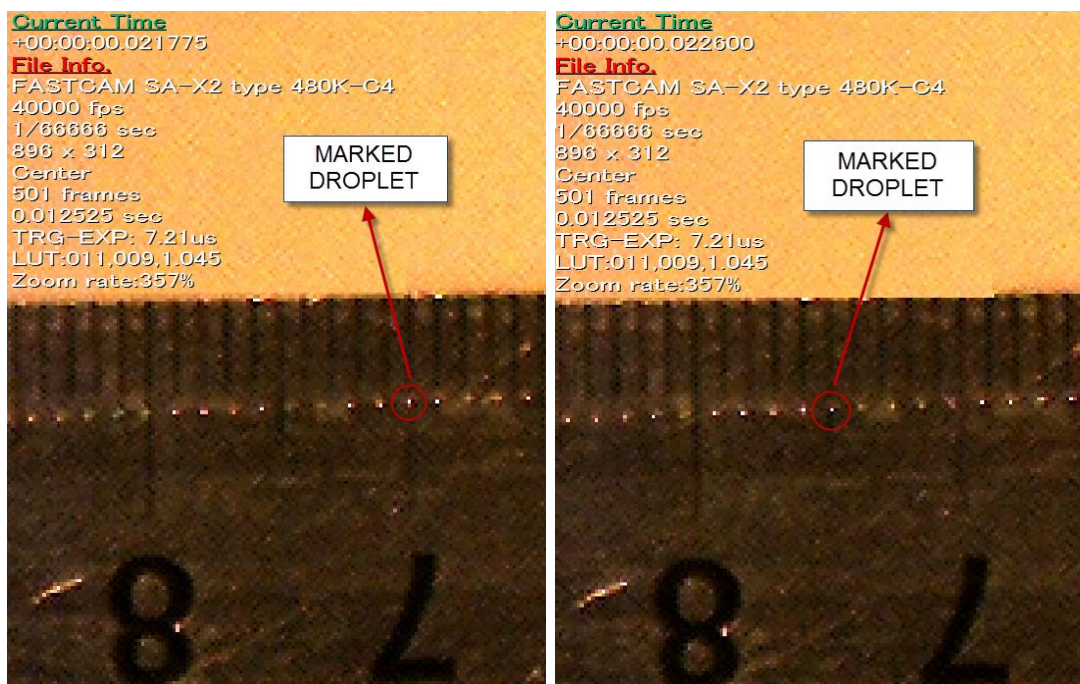


Figure 2.21. Actual Velocity Calculation

Table 2.6. Comparison of Theoretical Values and MDG Measurement Results

Orifice Diameter [μm]	Mass Flow Rate [ml/hr]	Actual Velocity [m/s]	Measured Velocity [m/s]			Max. Error %
			1	2	3	
100	133	6.06	6.32	6.36	6.22	4.95

The results show that uncertainty of the velocity measurement is less than 5%.

2.5. Experimental Investigation of the Hollow Cone Spray

In this section, macroscopic and microscopic properties of the hollow cone spray are examined for seven atomizers which have different geometrical parameters at three different flow rates. The hollow cone spray of the baseline PSA (A-1) for flow rates of $Q_1=0.100$ kg/s, $Q_2=0.173$ kg/s and $Q_3=0.240$ kg/s are given in Figure 2.22.

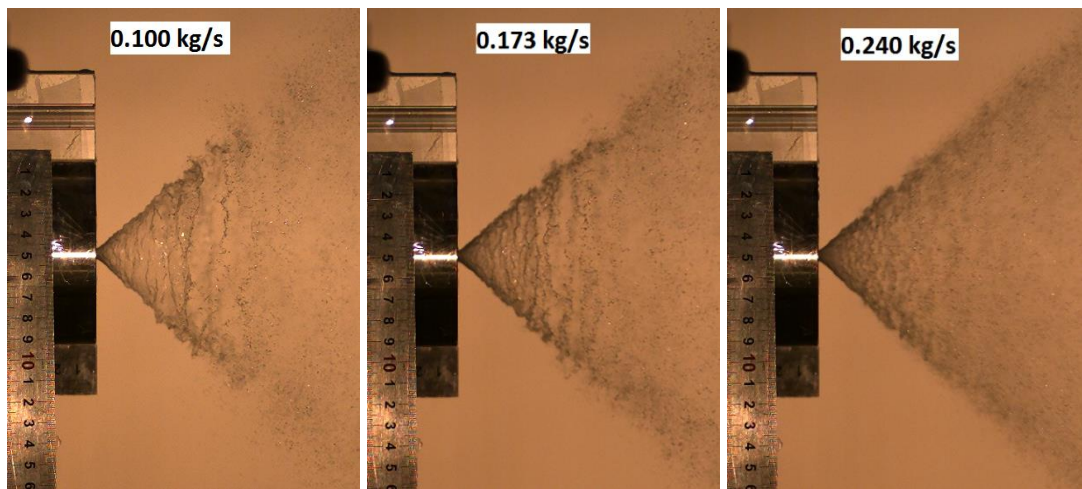


Figure 2.22. Hollow Cone Spray of Baseline PSA (A-1) for Different Flow Rates

Firstly, the SCAs of atomizers are calculated with image processing. Then, velocity distribution and droplet size of atomizer are obtained using two-component PDPA.

2.5.1. Macroscopic Properties

2.5.1.1. Spray Cone Angle

The SCA is described as an angle between the edges of the hollow cone spray. The ratio of the radial and axial velocity components of the spray gives the theoretical value of the SCA as expressed below [34]:

$$\tan \frac{\alpha}{2} = \frac{V_r}{V_a} \quad (2.4)$$

where α indicates the SCA whilst V_r indicates the radial velocity component, and V_a indicates the axial velocity component.

Figure 2.23 shows the calculation method of the SCA. Firstly, the distances between the two edges of hollow cone spray (Y_1 & Y_2) are measured at two different locations and then the horizontal distance between the measurement locations (X) is measured.

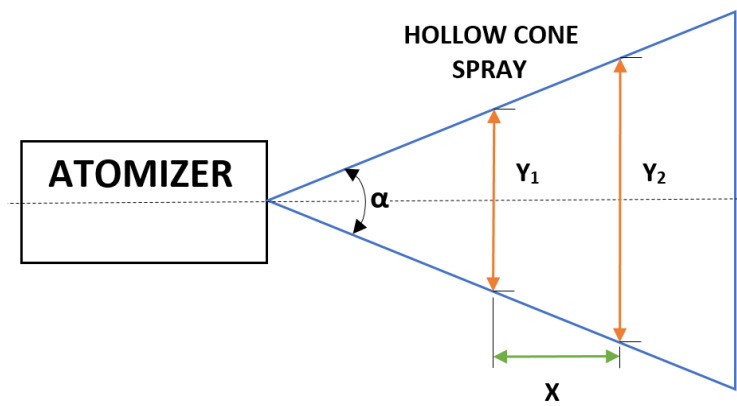


Figure 2.23. Calculation Method of SCA

In order to calculate the SCA, the following equation is used;

$$\alpha = 2 \tan^{-1} \left[\frac{(Y_2 - Y_1)/2}{X} \right] \quad (2.5)$$

Calculation method of SCA is applied to each captured image during the test. Then, mean value of calculated SCAs is defined as mean SCA.

2.5.1.2. Breakup Length

At a specific distance away from the exit of the nozzle, the momentum of turbulent fluctuations in the liquid jet overcomes the surface tension force and droplets can be formed [35], [36]. The distance from the nozzle exit to the point at which rotating thin film begins to disintegrate into small droplets is defined as breakup length. The breakup length is demonstrated in Figure 2.24.

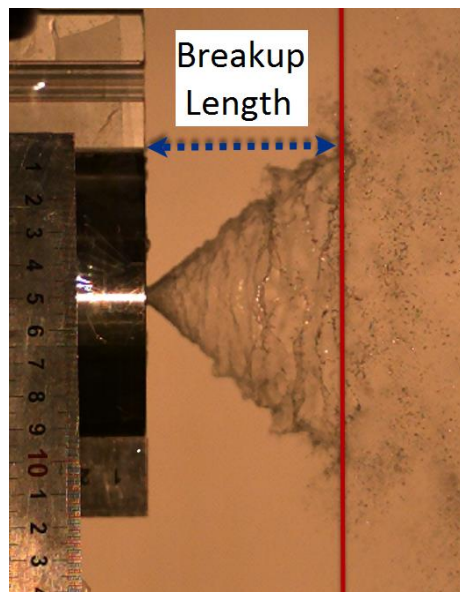


Figure 2.24. Demonstration of Breakup Length

2.5.2. Microscopic Properties

Microscopic properties of spray are velocity and droplet size distributions. The spray is investigated microscopically with PDPA system at 216 measurement points given in Figure 2.25 and field graphics of microscopic properties are plotted using Tecplot 360 software. The first axial measurement line is selected 20 mm away from the nozzle exit, because for shorter distance, the liquid is so dense that no signal can be detected by the receiver. The horizontal and vertical distances between the measurement points are 10 mm.

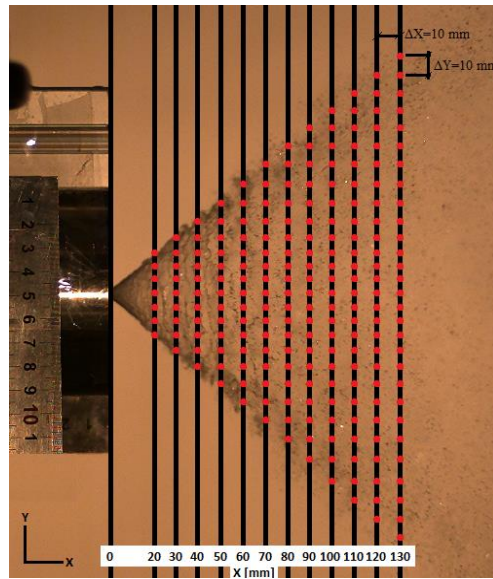


Figure 2.25. Measurement Points of Velocity Distribution and SMD

At each measurement point, the microscopic properties of selected seven atomizers are measured for flow rates of Q_1 , Q_2 and Q_3 . Snapshots of hollow cone spray and velocity-droplet size measurement with PDPA are given in Figure 2.26.

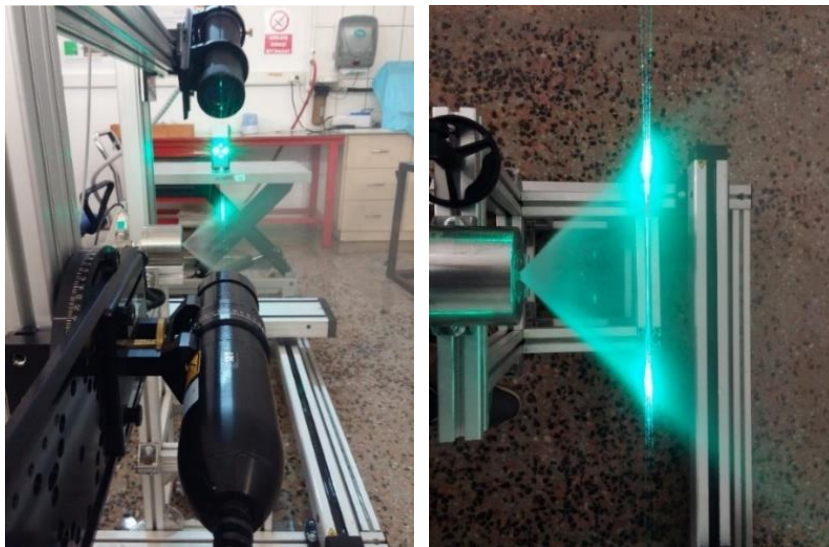


Figure 2.26. Snapshots of Hollow Cone Spray and Velocity-Droplet Size Measurement with PDPA

2.6. Pressure Drop Measurement

Pressure drop through the atomizer is measured with a pressure transducer which has a 0.5% error margin is placed at the inlet of the atomizer test assembly as shown in Figure 2.27. Inlet pressure of the atomizer test assembly is measured by the pressure transducer and difference between the measured inlet pressure and exit (atmospheric) pressure gives the pressure drop of the atomizer test assembly.

Atomizer test assembly total pressure drop is calculated by summing up the pressure drops of the reservoir and atomizer.

$$\Delta P_{\text{atomizer test assembly}} = \Delta P_{\text{reservoir}} + \Delta P_{\text{atomizer}} \quad (2.6)$$

Pressure drop of the reservoir is constant for all atomizers and pressure drop of atomizer test assembly changes only with changing atomizer pressure drop. Pressure drop values of atomizer test assembly are measured during the tests and mean pressure drop values are calculated to compare the pressure drops of atomizers.

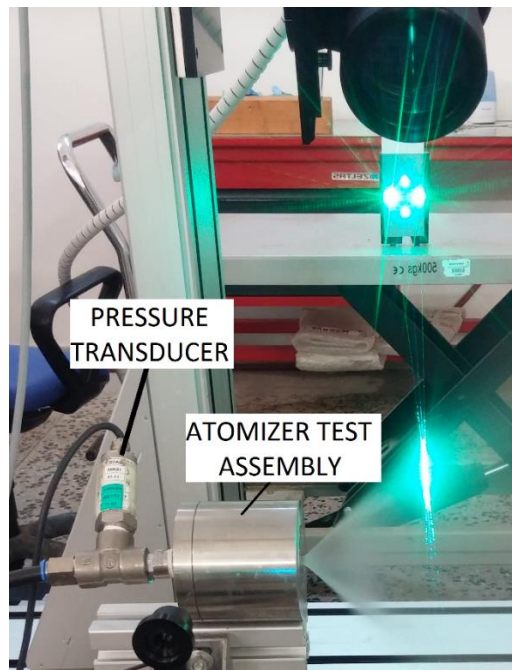


Figure 2.27. Location of Pressure Transducer

CHAPTER 3

NUMERICAL SIMULATIONS

3.1. Introduction

In this chapter, solution method of numerical simulations for baseline PSA is introduced. Internal physical phenomenon of the PSA is more complex than the estimations with simple correlations. Numerical simulations are performed to investigate the complex two-phase flow in the baseline PSA. In the numerical study, ANSYS-FLUENT software is used and Volume of Fluid (VOF) method is selected to model the multiphase interactions.

3.2. Method of Numerical Solution

The Volume of Fluid (VOF) is a widely used method for solving free surface flows [37]. In numerical simulations, VOF model is selected in order to model and solve the two-phase flow field. The flow field is assumed to be 2-D axisymmetric swirl because there are 2-D axisymmetric swirl CFD simulations for PSAs which are consistent with experimental results in the literature [38], [39], and [40].

In simulations, an implicit Pressure Based solver is used with first order implicit time discretization and VOF model is applied for multiphase interactions. Phase-1 is selected as the denser fluid water and Phase-2 is selected as air to increase the stability of simulations, as it is recommended in the software user manual [41]. The Phase-1 and Phase-2 are both considered incompressible. The internal flow of PSA is defined by the continuity equation (Equation (3.1)), unsteady state Navier-Stokes equations (Equation (3.2)), and advection equation (Equation (3.3)) [42].

$$\frac{\partial \rho}{\partial t} + \nabla(\rho \vec{V}) = 0 \quad (3.1)$$

$$\frac{\partial(\rho\vec{V})}{\partial t} + \nabla \cdot (\rho\vec{V}\vec{V}) = -\nabla p + \nabla \cdot [\mu(\nabla\vec{V} + \nabla\vec{V}^T)] + \rho\vec{g} + \vec{F}_{vol} \quad (3.2)$$

$$\frac{\partial\alpha_i}{\partial t} + \vec{V} \cdot \nabla\alpha_i = 0 \quad (3.3)$$

Energy term in Navier-Stokes equation is neglected because of small heat transfer assumption. The flow in the tangential direction with the ratio of swirl to axial velocity is dominant within the PSA, so the turbulent flow is ineffective compared to the magnitude of swirl velocity. Furthermore, the internal flow of the atomizer is accepted as laminar similar to the claims in [39], [40], and [43]. For the discretization, PRESTO scheme is used for pressure and Modified HRIC [44] is used for volume fraction calculations. Time step is defined to be 1 μ s for all simulations.

3.2.1. Boundary Conditions

Boundary conditions of the numerical model are given in Figure 3.1. Pressure outlet boundary condition is defined as right hand side and upper boundary of the simulation domain. Axis boundary condition is defined as bottom line for the axisymmetric solutions. Modelling of tangential port is impossible for axisymmetric simulations, so velocity inlet with radial and tangential components is applied to upper left corner of the PSA by means of axisymmetric swirl modeling of software. Radial component of velocity is adjusted to satisfying the mass flow rate value. Tangential component of velocity is adjusted to the mean velocity in the tangential ports to satisfy the angular momentum that enters the atomizer [29], [45], [46]. Boundary condition of velocity inlet is set to a line which has 1.7 mm length. The length of the velocity inlet line is set to be equal to the tangential port diameter (D_{tp}). Hence, the radial velocity at tangential ports can be calculated by satisfying the conservation of total mass flow rate using Equation (3.4), and the tangential velocity at tangential ports can be calculated by satisfying the angular momentum using Equation (3.5) [46].

$$V_r = Q/(2\rho\pi R_{sc}D_{tp}) \quad (3.4)$$

$$V_t = 4Q(R_{sc} - R_{tp})/(\rho\pi R_{sc}D_{tp}^2) \quad (3.5)$$

where Q indicates the mass flow rate, ρ indicates the fluid density, R_{sc} indicates the radius of swirl chamber, D_{tp} indicates the tangential port diameter, and R_{tp} indicates the radius of the tangential port. In the present simulations, mass flow rate is defined as $Q_1=0.100$ kg/s, $Q_2=0.173$ kg/s, and $Q_3=0.240$ kg/s, respectively.



Figure 3.1. Boundary Conditions

3.2.2. Measurement Locations

In order to calculate the SCA and air core diameter 14 different measurement lines are defined, and they are shown in Figure 3.2. The first 12 lines are located to calculate the air core diameter through the atomizer, and the rest of the lines are located to measure the SCA. The first line is 2 mm away from the beginning of the swirl chamber. The distances between the lines up to the line 11 are kept constant as 2 mm, and line 12 is located at the nozzle exit. The line 13 and line 14 is 2 mm and 4 mm away from the nozzle exit, respectively.

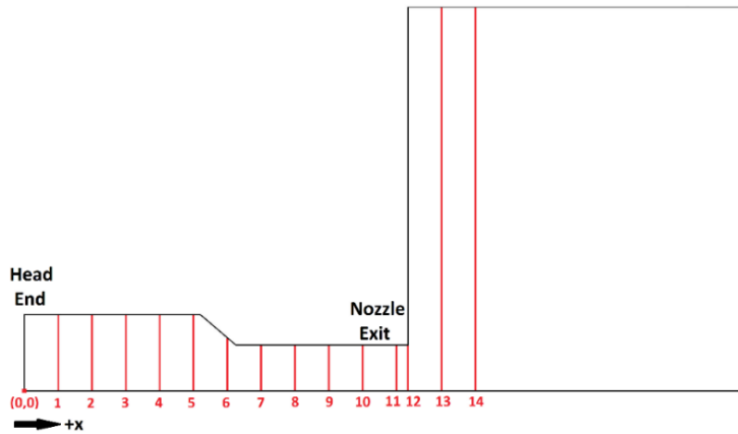


Figure 3.2. Measurement Locations

3.2.3. Grid Sensitivity Study

Grid resolution has an important effect for the analyzing of the flow field in the atomizer. Four different grid structures are generated to study the grid resolution effect on the results. These four different grids and cell numbers are shown together in Figure 3.3.

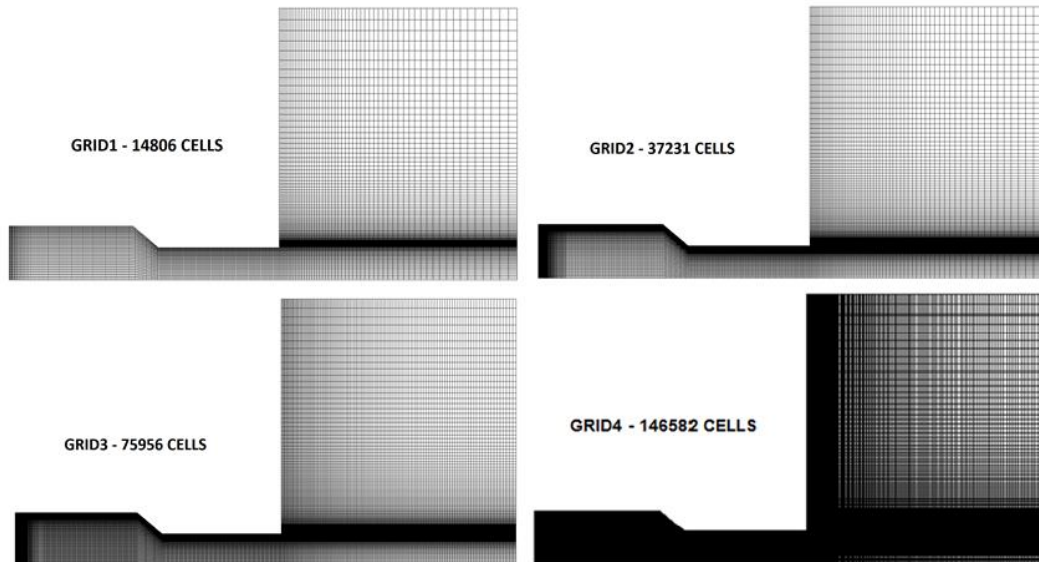


Figure 3.3. Grid Sensitivity

GRID1, GRID2, GRID3 and GRID4 contain 14806, 37231, 75956 and 146582 cells, respectively.

3.2.3.1. Grid Sensitivity Simulations Results

Numerical simulations are performed with GRID1, GRID2, GRID3 and GRID4. Two dimensional, axisymmetric, and unsteady flow simulations are repeated for each grid structure, respectively. The time step is selected as 1 μ s (fixed) for all simulations. Evolutions of air volume fraction of air through the baseline PSA with time are given in Figure 3.4 for four solution domains for the first 7 ms.

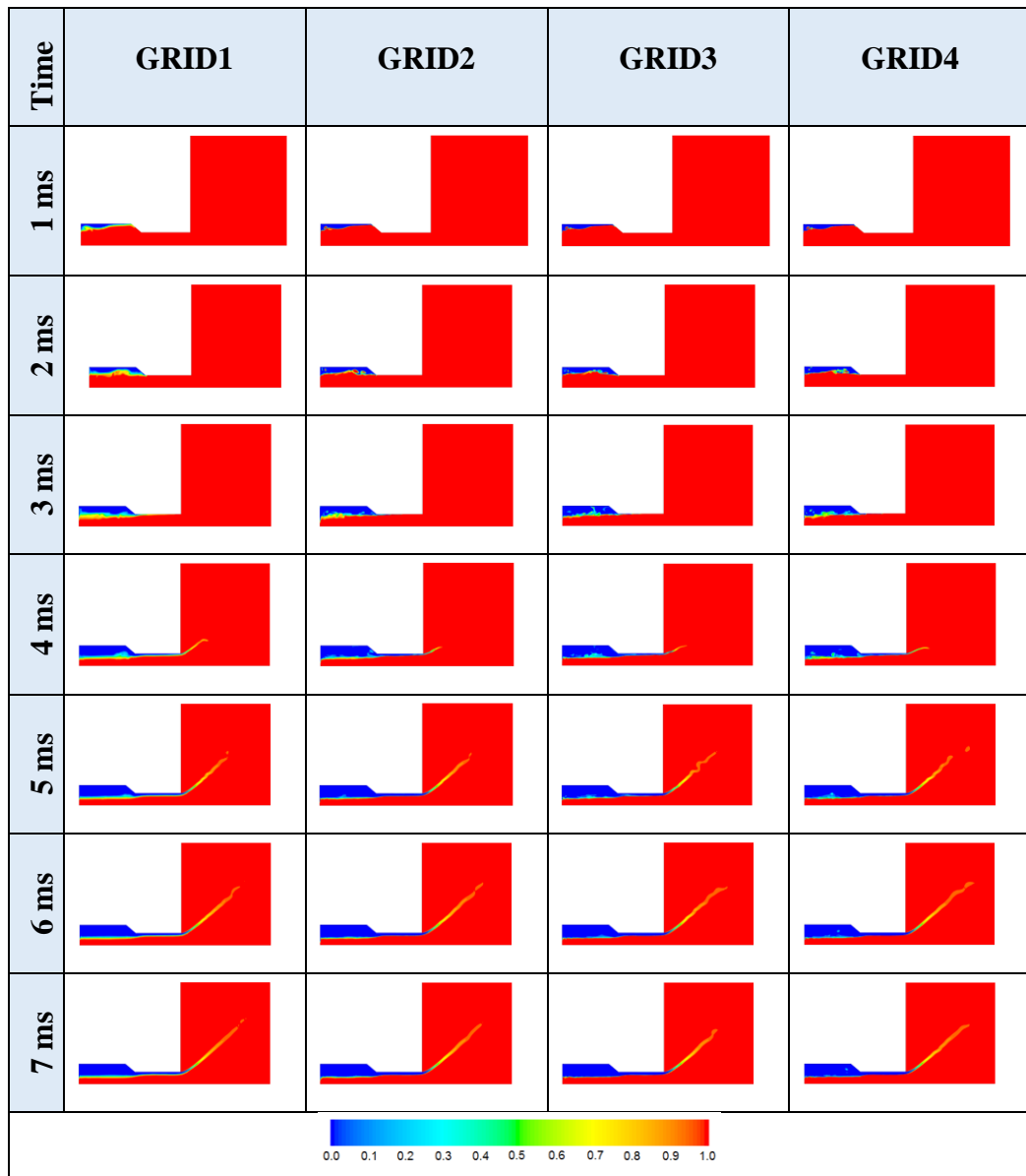


Figure 3.4. Evolution of air volume fraction contours for GRID1, GRID2, GRID3 and GRID4

Water exits from the nozzle of the atomizer at about 4 ms and starts to become stable after 6 ms as shown in Figure 3.4. After 6 ms, numerical simulations are continued until 30 ms and flow statistical properties are obtained. Mean values of volume fraction, static pressure, swirl velocity, and axial velocity are calculated by averaging of the mentioned properties between 6 ms and 30 ms.

The contours of mean volume fraction for air are given in Figure 3.5.

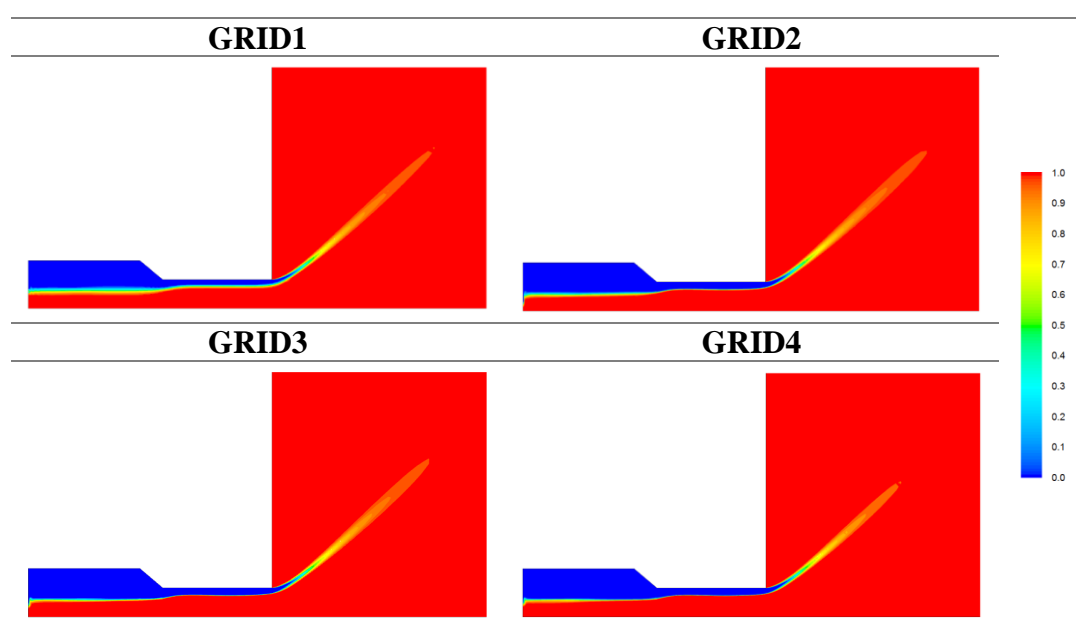


Figure 3.5. Contours of Mean Volume Fraction for Air

When the contours of mean volume fraction for air are analyzed, it is seen that there is a difference in the shape at the head of the atomizer, which is in agreement previous works [29] and [47]. As shown in Figure 3.6, a constant air core diameter is observed through the swirl chamber for GRID1, a smaller air core diameter is obtained at the beginning of the swirl chamber for the rest of the grids. The shape of the interface at the beginning of the swirl chamber for GRID2 has a different geometrical shape than GRID3 and GRID4, whereas the shape is nearly the same for GRID3 and GRID4.

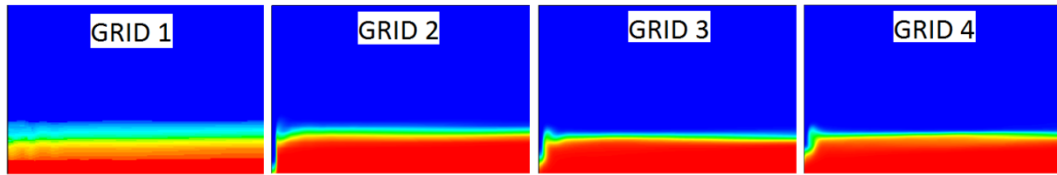


Figure 3.6. Contours of Mean volume fraction for air at the beginning of the swirl chamber

The mean static pressure contours for four grids are given in Figure 3.7. As seen from the contours, at the upside of the swirl chamber the mean static pressure reaches its maximum. The maximum mean static pressure values obtained from the numerical solutions are 4.70 bars, 4.61 bars, 4.67 bars, and 4.73 bars for GRID1, GRID2, GRID3 and GRID4, respectively.

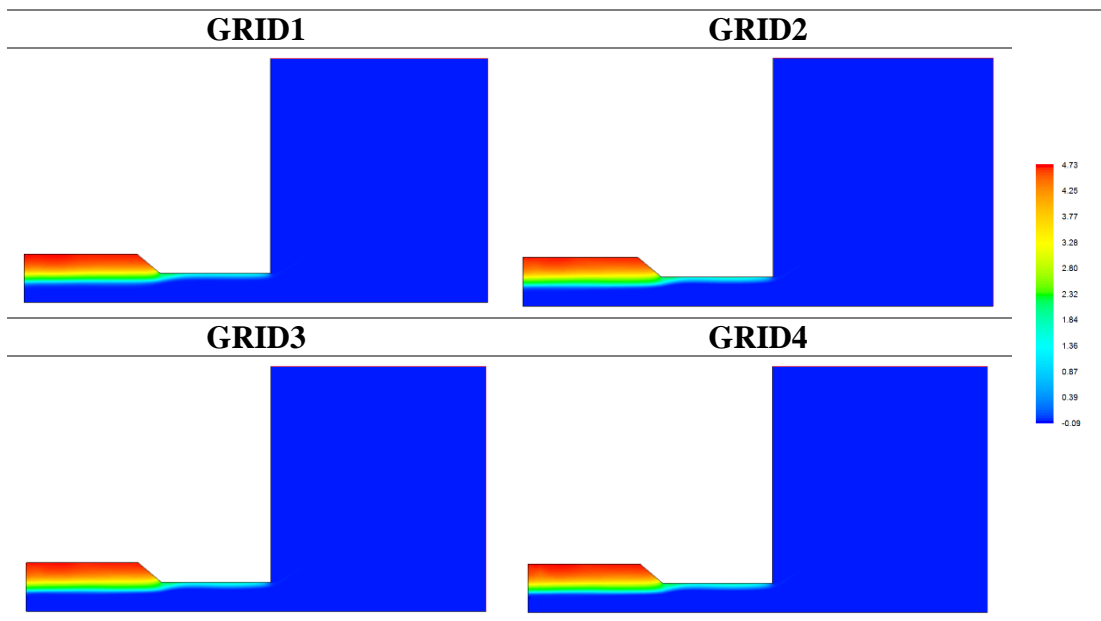


Figure 3.7. Contours of Mean Static Pressure [bars]

The minimum values of mean static pressure at the air core are obtained as 0.02 bars, 0.01 bars, 0.08 bars and 0.09 bars below the ambient pressure for GRID1, GRID2, GRID3 and GRID4, respectively.

The mean axial velocity contours for four solution domains are given in Figure 3.8. As seen from the contours, at the atomizer exit the mean axial velocity approaches its maximum. The maximum values of mean axial velocity are 24.22 m/s, 23.98 m/s, 24.01 m/s and 24.01 m/s for GRID1, GRID2, GRID3 and GRID4, respectively.

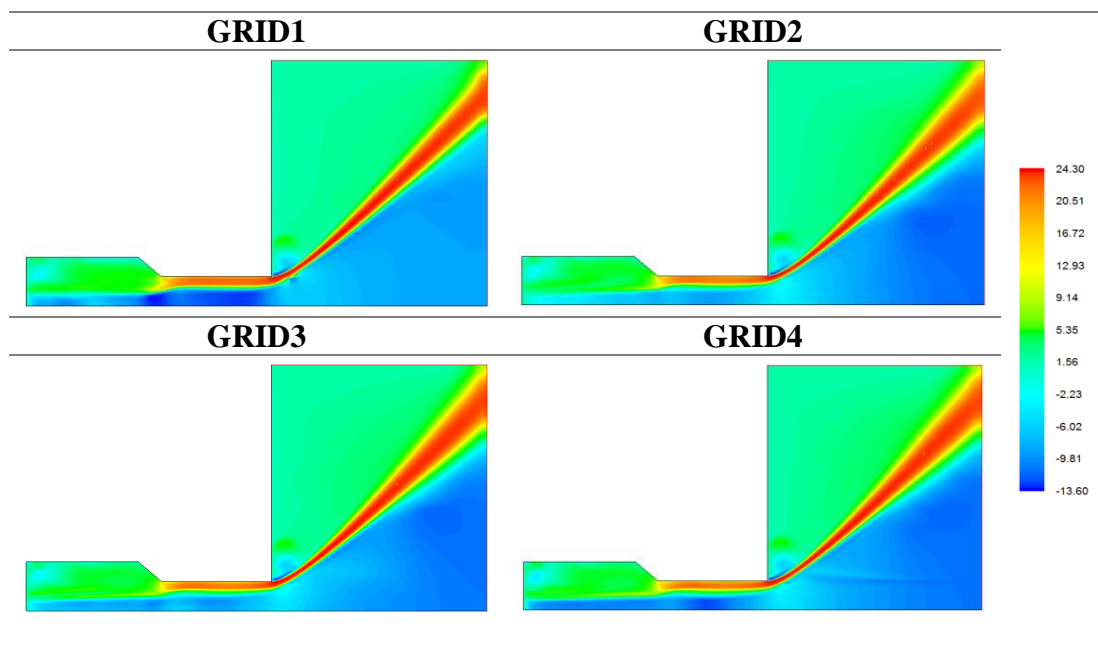


Figure 3.8. Contours of Mean Axial Velocity Contours [m/s]

The minimum mean axial velocities -13.51 m/s, -12.42 m/s, -12.21 m/s and -12.40 m/s for GRID1, GRID2, GRID3 and GRID4, respectively.

The mean swirl velocity contours for four solution domains are given in Figure 3.9. As seen from the contours, the mean swirl velocity reaches its maximum value near the air core of the atomizer. The maximum values of mean swirl velocity are 28.18 m/s, 29.10 m/s, 29.37 m/s and 29.34 m/s for GRID1, GRID2, GRID3 and GRID4, respectively.

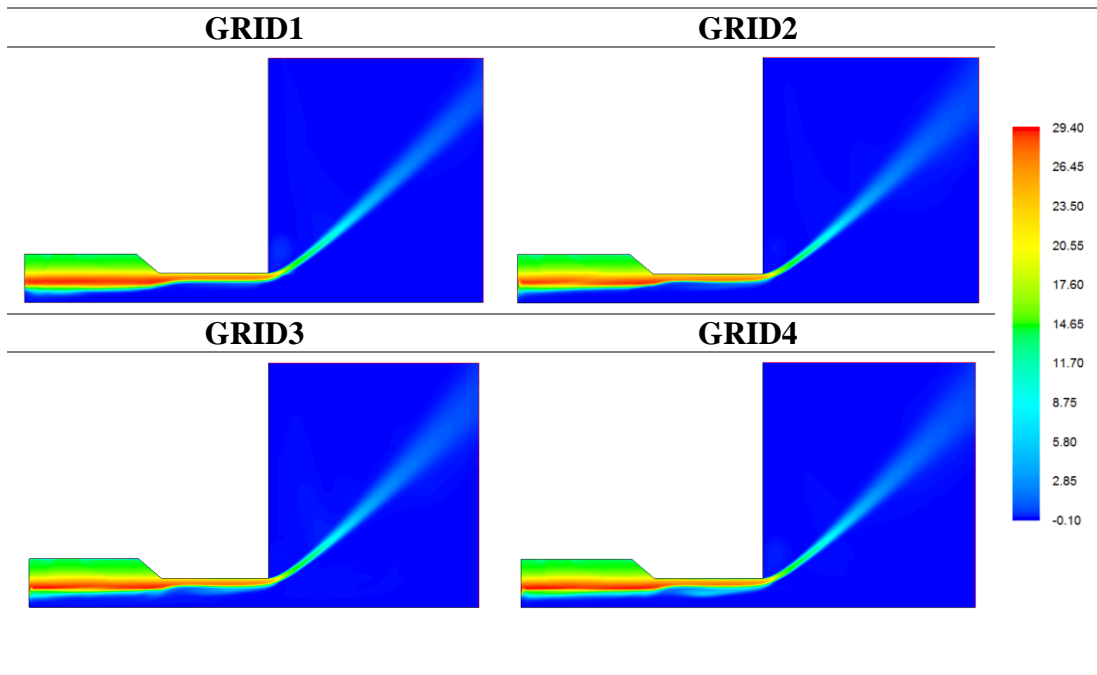


Figure 3.9. Contours of Mean Swirl Velocity [m/s]

The oscillation at the beginning of the swirl chamber could not be captured with GRID1 and GRID2 as shown in Figure 3.6, therefore these two grids are eliminated. To make a selection between GRID3 and GRID4, the mean static pressure, mean axial velocity and mean swirl velocity distributions at designated lines are investigated.

The mean static pressures at four different measurement lines for GRID3 and GRID4 are given in Figure 3.10. The mean static pressure standard deviation is shown as error bars in Figure 3.10.

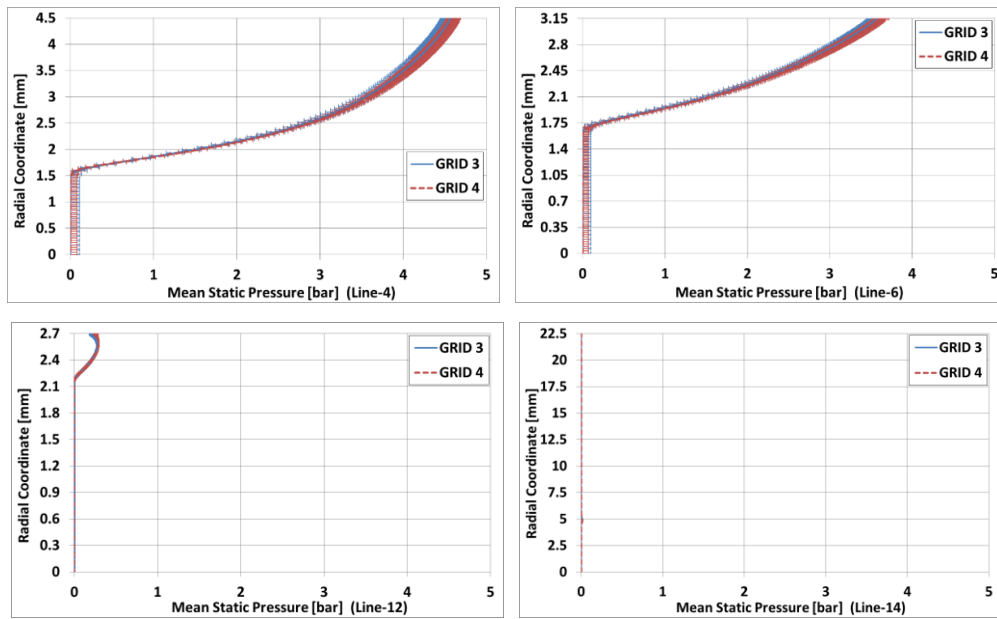


Figure 3.10. Mean Static Pressure at Designated Lines

The mean axial velocities at four different measurement lines for GRID3 and GRID4 are given in Figure 3.11. The mean axial velocity standard deviation is shown as error bars in Figure 3.11.

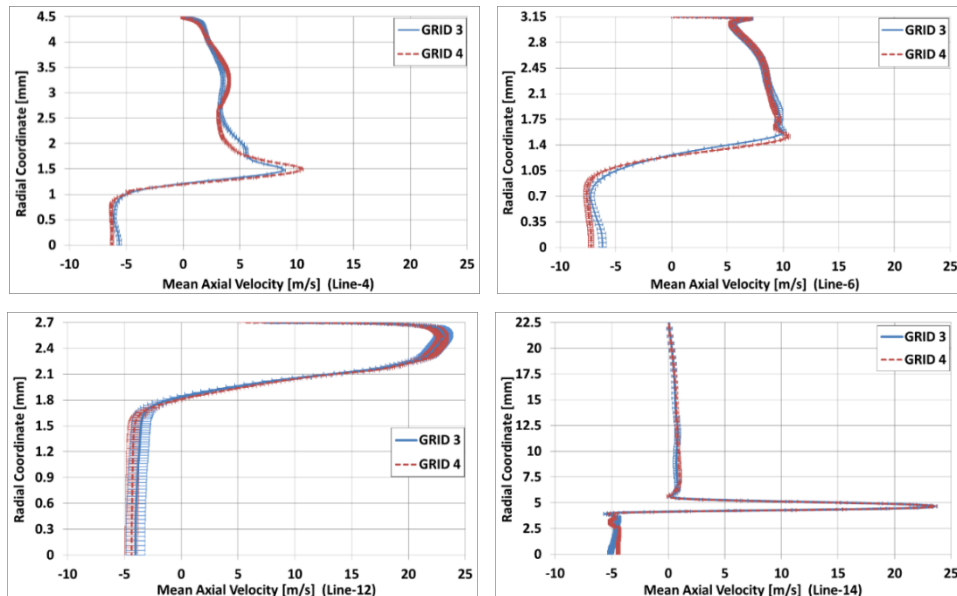


Figure 3.11. Mean Axial Velocities at Designated Lines

The mean swirl velocities at four different measurement lines for GRID3 and GRID4 are given in Figure 3.12. The mean swirl velocity standard deviation is shown as error bars in Figure 3.12.

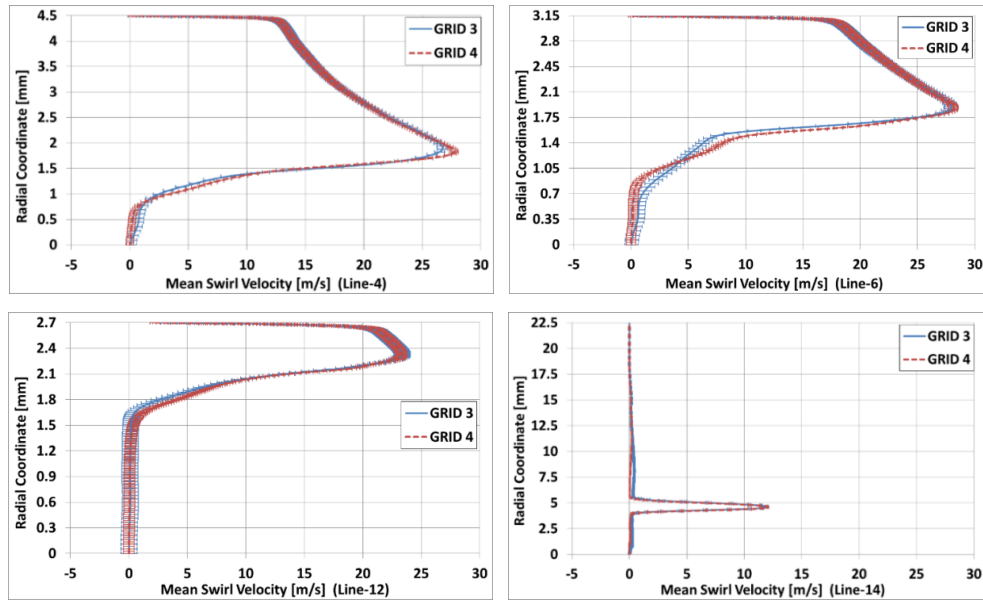


Figure 3.12. Mean Swirl Velocities at Designated Lines

3.2.3.2. Conclusion

To examine the grid resolution effect on the numerical results, four grid structures are generated and numerical simulations are performed. The simulation results indicate that grid resolution has an important effect in order to model the flow features of the atomizer correctly. The flow features in the PSA cannot be detected with GRID1 and GRID2, however, oscillations at the beginning of the swirl chamber are realized with GRID3 and GRID4. Mean static pressures, mean swirl velocities, and mean axial velocities are compared for GRID3 and GRID4, and it is obtained that the mean values are very close to each other. However, the computation time for the GRID4 is two times longer than the GRID3.

As a result of grid sensitivity study, GRID3 was selected in order to investigate the two-dimensional axis-symmetric swirl simulations of PSA.

3.2.4. Spray Cone Angle Calculation

SCAs of numerical simulations are calculated with the image processing program defined in Section 2.4.1.1 and calculation method, details of which was given in Section 2.5.1. A sample image obtained by the Sobel edge detector application is given in Figure 3.13.

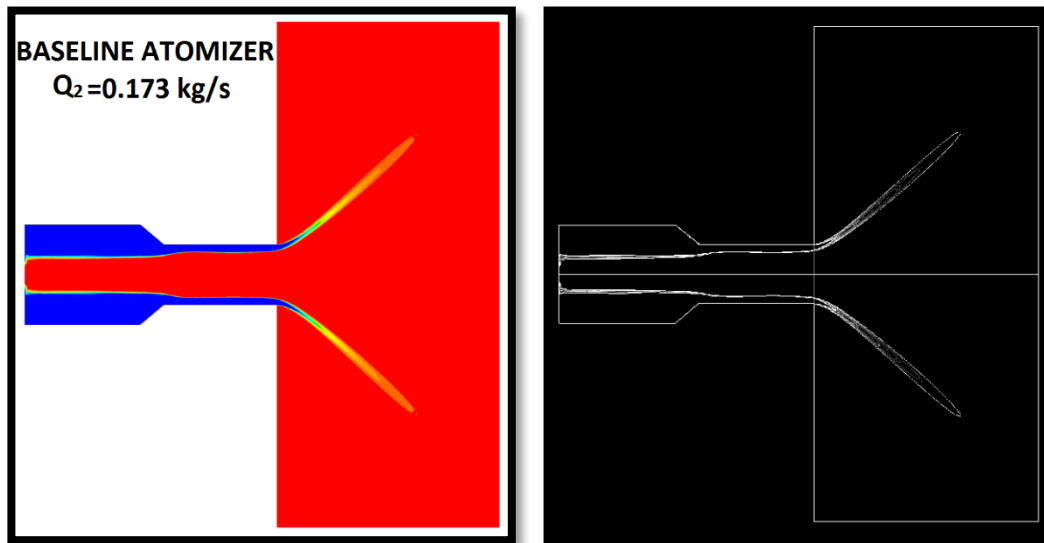


Figure 3.13. Sobel Edge Detector Application for Numerical Simulations

CHAPTER 4

RESULT OF EXPERIMENTAL STUDY

4.1. Results of Macroscopic Properties

4.1.1. Results of Spray Cone Angle Measurements

Mean SCA of A-1 at a flow rate of 0.100 kg/s is calculated for 100, 200 and 500 captured images, respectively. The calculated mean SCAs are given in Table 4.1.

Table 4.1. *Image Quantity Dependency*

	100 images	250 images	500 images
A-1 (Baseline PSA) (0.100 kg/s)	83.0°	83.2°	83.1°

The results show that the mean SCAs calculated for different image quantities are very close to each other. Therefore, the rest of the mean SCA calculations are done for quantity of 100 images to shorten the calculation time.

In order to examine the nozzle diameter effect on SCA, mean SCAs of A-1, A-2, and A-3 are calculated and results are given in Table 4.2 for these three atomizers at three different mass flow rates.

Table 4.2. *Calculated Mean SCAs for Selected Atomizers*

	Mean SCA		
	Q ₁	Q ₂	Q ₃
A-2 (D_o=4.1 mm)	74.3°	76.4°	75.9°
A-1 (D_o=5.4 mm)	83.0°	81.1°	85.8°
A-3 (D_o=6.8 mm)	85.8°	87.6°	87.6°

In order to research the tangential port number effect on SCA, mean SCAs of A-1, A-4, and A-5 are calculated and results are given in Table 4.3 for these three atomizers at three different mass flow rates.

Table 4.3. *Calculated Mean SCAs for Selected Atomizers*

	Mean SCA		
	Q ₁	Q ₂	Q ₃
A-5 (N_{tp}=2)	77.1°	82.3°	85.4°
A-4 (N_{tp}=4)	81.2°	83.5°	85.1°
A-1 (N_{tp}=6)	83.0°	81.1°	85.8°

In order to examine the nozzle length effect on SCA, mean SCAs of A-1, A-6, and A-7 are calculated and results are given in Table 4.4 for these three atomizers at three different mass flow rates.

Table 4.4. *Calculated Mean SCAs for Selected Atomizers*

	Mean SCA		
	Q ₁	Q ₂	Q ₃
A-6 (L_o=8.1 mm)	81.2°	82.1°	84.4°
A-1 (L_o=10.2 mm)	83.0°	81.1°	85.8°
A-7 (L_o=13.5 mm)	79.1°	80.2°	82.1°

As mentioned in Section 2.4.1.1, the uncertainty level for the measurement of the length between two edges of the hollow cone spray is ± 1 pixel and this uncertainty causes maximum 3° deviation in SCA measurements. Therefore, all calculated mean SCAs have an uncertainty less than $\pm 3^\circ$.

The results show that mass flow rate has no evident effect on the mean SCA. When mass flow rate increases, the radial and axial velocity components increase, too. But the ratio of radial to axial velocity remains nearly the same. Therefore, mass flow rate has negligible effect on SCA. The radial and axial velocity components of baseline PSA for three mass flow rates are shown in Table 4.5.

Table 4.5. Radial and Axial Velocity Components of Baseline PSA.

	Q₁	Q₂	Q₃
Radial Velocity [m/s]	8.64	15.54	20.52
Axial Velocity [m/s]	10.49	18.70	24.88
Ratio of Radial Velocity to Axial Velocity	0.824	0.831	0.825

Also it is obtained from the results that mean SCA increases with increasing nozzle diameter, which agrees with the trend defined in [16]. Especially, a significant increase is observed as the nozzle diameter is increased from 4.1 mm to 5.4 mm. The physical explanation for this increment is the decrease in nozzle strength. A decline in the nozzle resistance because of the increase in nozzle diameter decreases the swirling strength of flow in the nozzle and causes a larger value of swirl velocity. An increase in the ratio of swirl to axial velocity components results in a larger SCA.

SCA is also insensitive to the tangential port number. For the atomizers A-1, A-4, and A-5 only the tangential port number is changed, the total flow area of tangential ports is kept constant. Therefore, tangential port number has a negligible effect on velocity components and SCA, which is in agreement with previous work [14].

The results also show that nozzle length has little impact on SCA because of its little influence on velocity components. It can be also shown in results that a small increase in the nozzle length has insignificant effect on SCA but a further increase results in more energy losses due to friction which cause a decrease in SCA. The behavior of the SCA with nozzle length agrees with the investigations in [48].

The results finally show that calculated SCA value of baseline PSA for $Q_2=0.173$ kg/s is very close to the SCA value of RD-0110 inner atomizer for the same mass flow rate. The calculated angle differs only 1.1° from the given value in [9].

4.1.2. Results of Breakup Length Measurements

In order to investigate the nozzle diameter effect on breakup length, breakup lengths of A-1, A-2, and A-3 are measured at different mass flow rates. The obtained results are given in Table 4.6.

Table 4.6. Measured Breakup Lengths for Selected Atomizers

	Breakup Length [mm]		
	Q ₁	Q ₂	Q ₃
A-2 (D_o=4.1 mm)	49.8	29.6	18.4
A-1 (D_o=5.4 mm)	60.5	49.3	35.4
A-3 (D_o=6.8 mm)	73.1	56.9	50.2

In order to examine the tangential port number effect on the breakup length, breakup lengths of A-1, A-4, and A-5 are measured at different mass flow rates. The obtained results are given in Table 4.7.

Table 4.7. Measured Breakup Lengths for Selected Atomizers

	Breakup Length [mm]		
	Q ₁	Q ₂	Q ₃
A-5 (N_{tp}=2)	58.3	52.5	33.6
A-4 (N_{tp}=4)	57.4	46.2	37.8
A-1 (N_{tp}=6)	60.5	49.3	35.4

In order to investigate the nozzle length effect on breakup length, breakup lengths of A-1, A-6, and A-7 are measured at different mass flow rates. The obtained results are given in Table 4.8.

Table 4.8. Measured Breakup Lengths for Selected Atomizers

	Breakup Length [mm]		
	Q ₁	Q ₂	Q ₃
A-6 (L_o=8.1 mm)	62.3	49.3	36.8
A-1 (L_o=10.2 mm)	60.5	49.3	35.4
A-7 (L_o=13.5 mm)	62.9	47.9	35.9

The uncertainty level for the measurement of the breakup length is ± 1 pixel and this uncertainty causes maximum 0.5 mm deviation in breakup length measurements. Therefore, all measured breakup length values have an uncertainty less than ± 0.5 mm.

The results show that increasing mass flow rate and decreasing nozzle diameter cause the thin film to disintegrate at a shorter distance and shorten the breakup length. On the other hand, nozzle length and tangential port number have little effect on breakup length.

4.2. Results of Microscopic Measurements

The hollow cone spray is investigated microscopically with two-component PDPA System for seven test atomizers.

The X-Velocity histograms of baseline PSA (A-1) for $Q_2=0.173$ kg/s are given in Figure 4.1. The X-Velocity of point (x=40 mm, y=0 mm) is measured as -11.6 m/s. As shown in histogram, X-Velocity of droplets is negative at point (x=40 mm, y=0 mm), since droplets move in the opposite direction to the water flow because of the reverse air flow at the center of the hollow cone spray. The X-Velocity of point (x=40 mm, y=40 mm) is measured as 13.8 m/s. The X-Velocity of droplets at the same axial coordinate value (x=40 mm) changes sign with increasing radial coordinate and reaches maximum value on the liquid jet.

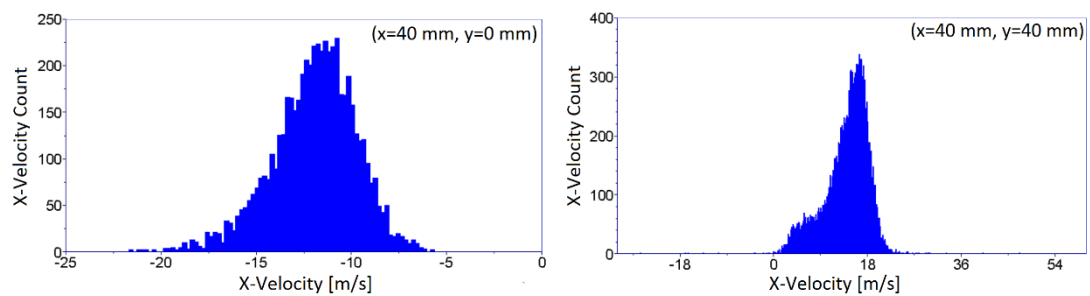


Figure 4.1. X-Velocity Histograms at designated locations (A-1)

The Y-Velocity histograms of baseline PSA (A-1) for $Q_2=0.173$ kg/s are given in Figure 4.2. The Y-Velocity of point (x=40 mm, y=0 mm) is measured as -0.2 m/s. This result shows that there is no rotating flow at the center of the hollow cone spray. The Y-Velocity of point (x=40 mm, y=40 mm) is measured as 11.3 m/s. The Y-Velocity of droplets at the same axial coordinate (x=40 mm) increases with increasing radial coordinate and reaches maximum value on the liquid jet.

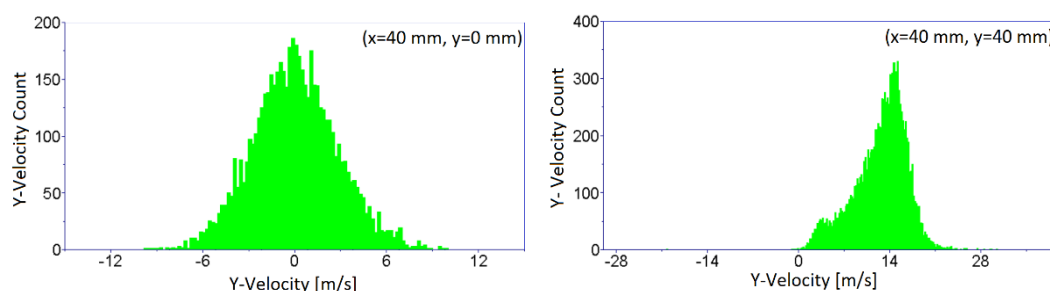


Figure 4.2. Y-Velocity Histograms at designated locations (A-1)

The diameter histograms of baseline PSA (A-1) for $Q_2=0.173$ kg/s are given in Figure 4.3. The SMD values of point (x=40 mm, y=0 mm) and point (x=40 mm, y=40 mm) are 56 and 198, respectively. The histograms show that smaller particles are located at the center of the hollow cone spray, and particle diameter increase with increasing radial coordinate. Diameter of particles reaches maximum value on the liquid jet.

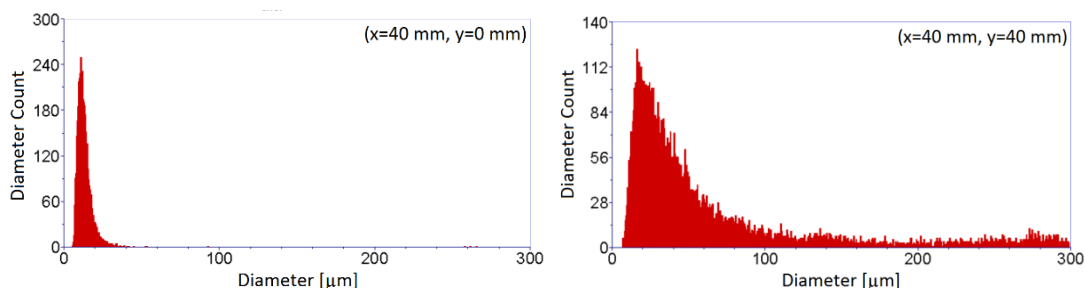


Figure 4.3. Diameter Histograms at designated locations (A-1)

4.2.1. Nozzle Diameter Effects on the Microscopic Properties

In order to investigate the nozzle diameter effect on the microscopic properties experimental studies are performed with A-2 ($D_o=4.1$ mm), A-1 ($D_o=5.4$ mm), and A-3 ($D_o=6.8$ mm), and results are given in Figure 4.4, Figure 4.5, and Figure 4.6 for Q_1 , Q_2 , and Q_3 , respectively. The contours and streamlines are plotted from at $x=20$ mm.

As shown in contours of mean velocity given in Figure 4.4, a vortex revealed at the exit of the atomizer for all three nozzle diameters. As the nozzle diameter increases the mean velocities of the droplets decrease, the vortex expands and moves away from the atomizer. At the nozzle exit, small water particles which are close to the x-axis are affected from the air flow and move with the air flow.

Mean x velocity contours of A-2, A-1, and A-3 for $Q_1=0.100$ kg/s are given in Figure 4.4. As shown in the figure, mean x velocity of the particles tends to decrease with increasing nozzle diameter. The maximum mean x velocity is measured as 15.70 m/s, 10.49 m/s, and 7.79 m/s for A-2, A-1, and A-3, respectively. It is also observed that the mean x velocity of droplets decreases with increasing x-coordinate for each nozzle diameter.

Mean y velocity contours of A-2, A-1, and A-3 for $Q_1=0.100$ kg/s are given in Figure 4.4. Increasing nozzle diameter has a reducing effect on droplets mean y velocity. The maximum mean y velocity is measured as 9.56 m/s, 8.65 m/s, and 7.39 m/s for A-2, A-1, and A-3, respectively. For each nozzle diameter, the mean y velocity of droplets tends to decrease with increasing x-coordinate.

The SMD contours of A-2, A-1, and A-3 for $Q_1=0.100$ kg/s are given in Figure 4.4. As shown in the figure, the small droplets are positioned in the center of the spray, and an increase is shown in SMD with y coordinate and reaches the maximum value on the liquid jet. Increasing nozzle diameter leads to a decrease in velocity, energy and angular momentum of the liquid. As a result of that the SMD of the particles on the liquid jet increases. Increasing nozzle diameter also leads to a reduction in

instability of the waves on the surface of the hollow cone spray. Obtained results show that breakup occurs further away from the nozzle exit.

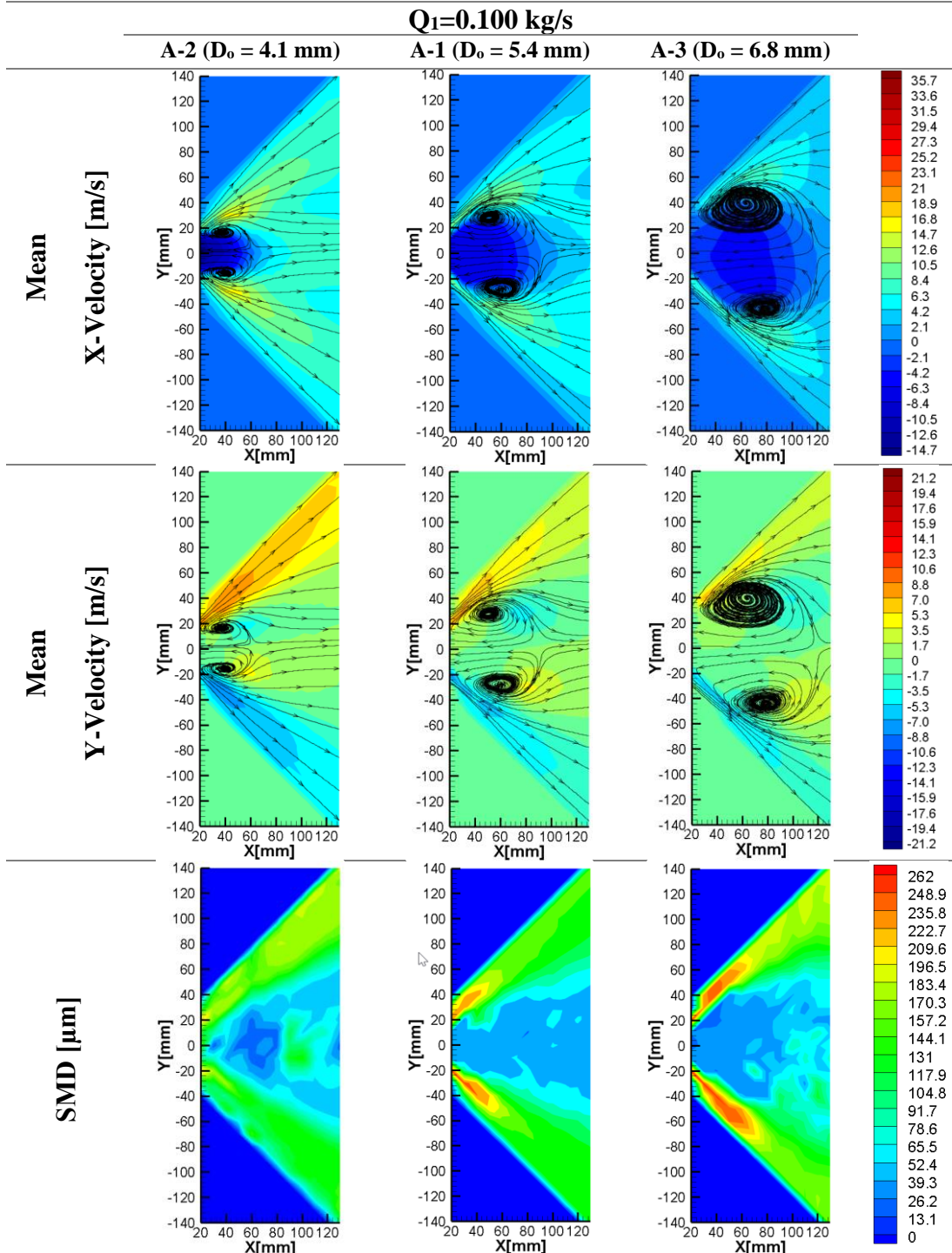


Figure 4.4. Nozzle Diameter Effect on the Microscopic Properties for Q_1

In order to investigate the nozzle diameter effect at different mass flow rates experiments are repeated for Q_2 and Q_3 , and results are demonstrated in Figure 4.5 and Figure 4.6, respectively. As shown in mean velocity and SMD contours, when the mass flow rate is increased, the change in nozzle diameter leads to similar effects on the microscopic properties as the flow rate is Q_1 .

Mean x velocity and mean y velocity tend to decrease with increasing nozzle diameter. The maximum mean x velocity of the particles is measured as 28.70 m/s, 18.70 m/s, and 13.43 m/s, and the maximum mean y velocity of the particles is measured as 17.97 m/s, 15.54 m/s, and 12.15 m/s for A-2, A-1, and A-3 at $Q_2=0.173$ kg/s, respectively. The maximum mean x velocity of the particles is 35.67 m/s, 24.88 m/s, and 19.00 m/s, and the maximum mean y velocity of the particles is 21.14 m/s, 20.52 m/s, and 15.16 m/s for A-2, A-1, and A-3 at $Q_3=0.240$ kg/s, respectively.

As shown in the SMD contours for Q_2 and Q_3 , increasing nozzle diameter has a reducing effect on the velocity, energy and angular momentum of liquid. As a result of that, as in the flow rate of Q_1 , SMD values of the droplets increase and breakup occurs further away from the nozzle exit.

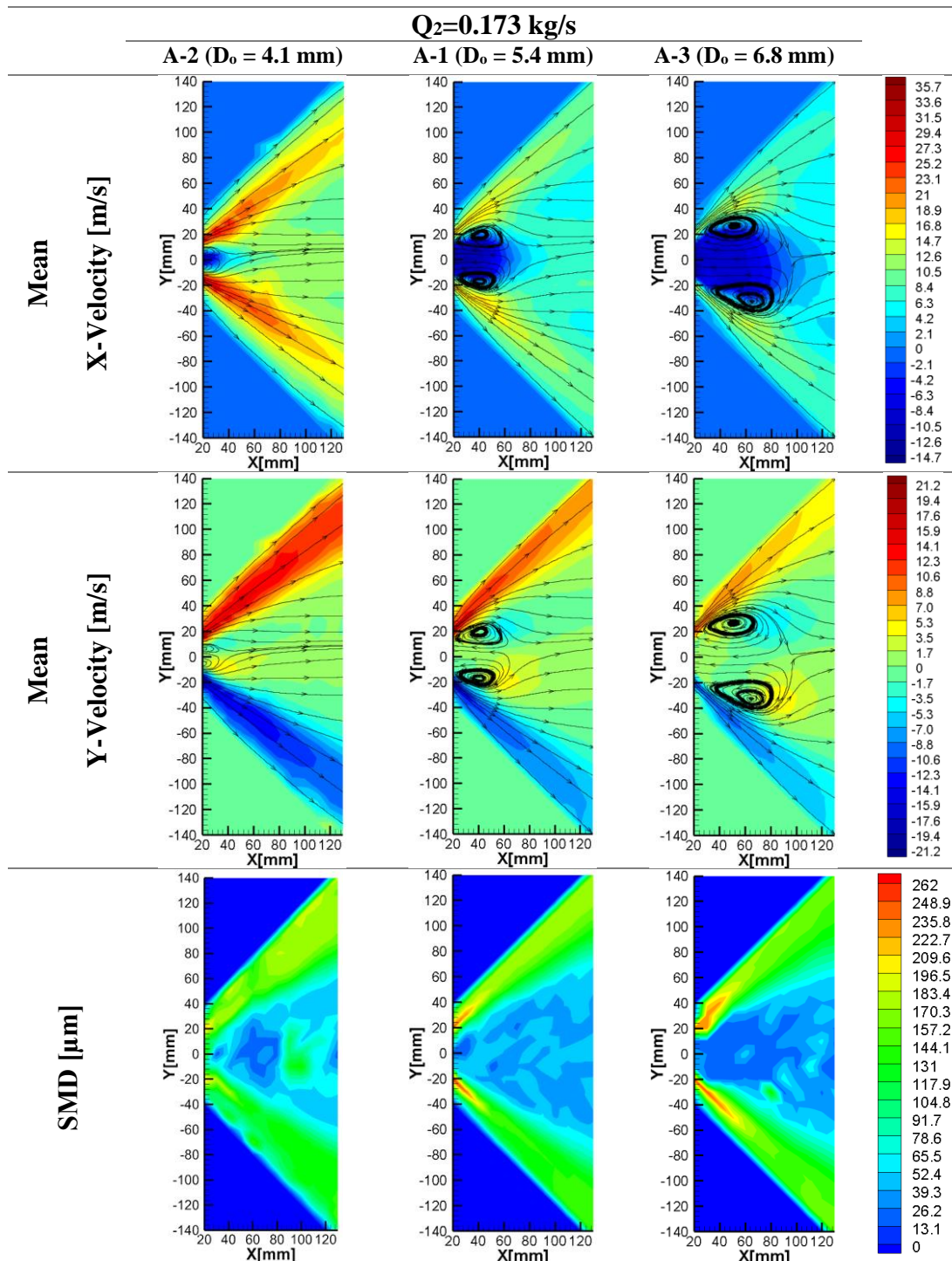


Figure 4.5. Nozzle Diameter Effect on the Microscopic Properties for Q_2

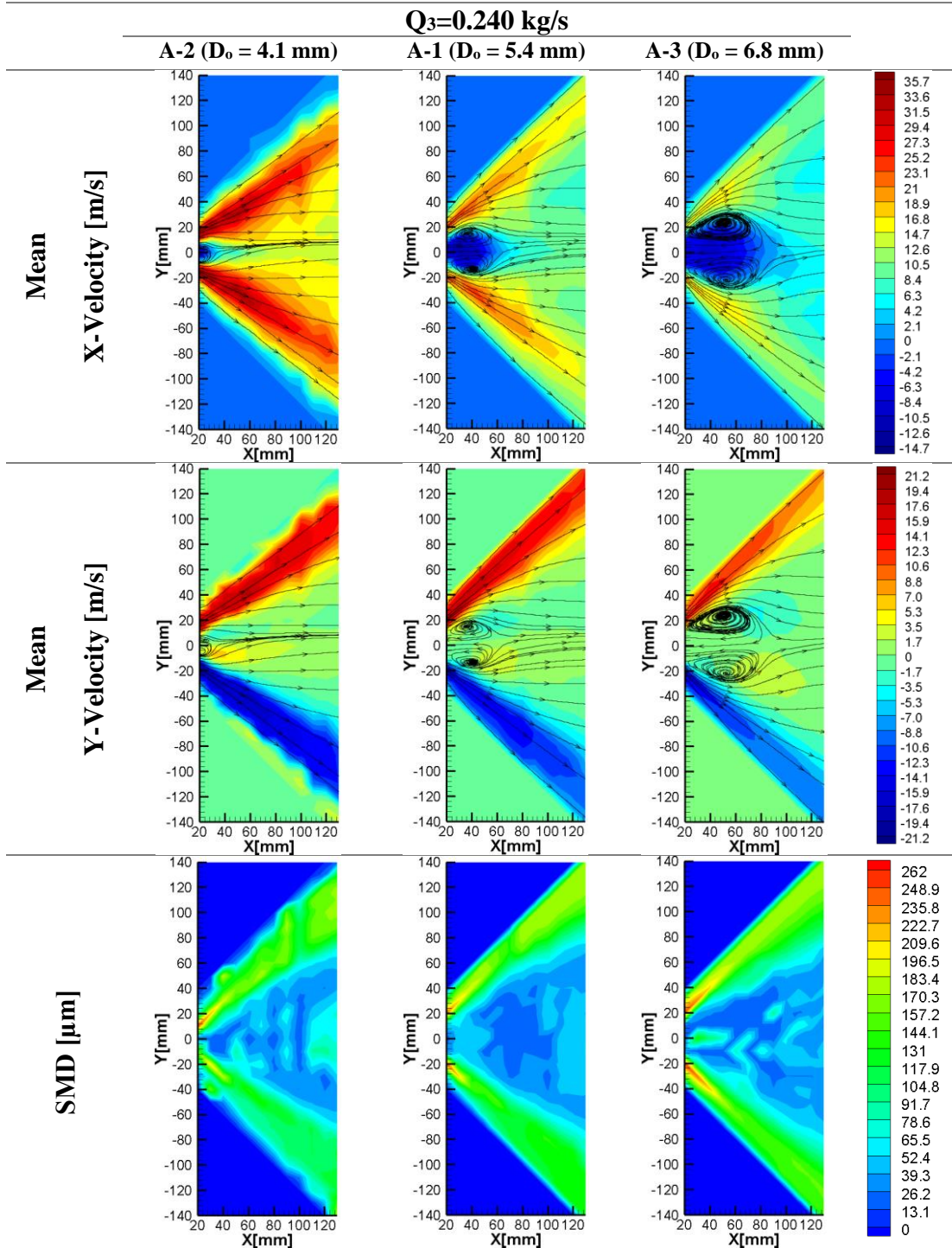


Figure 4.6. Nozzle Diameter Effect on the Microscopic Properties for Q_3

In order to compare the results, mean x velocity, mean y velocity, and SMD values at $x=40$ mm, 80 mm, and 120 mm are plotted for A-2, A-1, and A-3. Comparison graphics are given in Figure 4.7, Figure 4.8, and Figure 4.9 for Q_1 , Q_2 , and Q_3 , respectively.

As shown in the velocity graphics plotted for designated x locations, magnitudes of mean x velocity and mean y velocity on the spray increase with increasing nozzle diameter. In the center of the spray, mean x velocities are in negative values in the revealed vortex, and magnitude of mean x velocity decrease with increasing nozzle diameter. Out of the vortex, particles change direction and mean x velocity takes on positive values and increasing nozzle diameter leads to decrease in mean x velocity. In the center of the spray, mean y velocity decreases to zero and reach maximum value on the liquid jet.

As shown in comparison graphics of SMD, increasing nozzle diameter results in an increase in SMD values at x coordinates near the nozzle exit. But, effect of increasing nozzle diameter losses its strength on SMD for increasing x coordinates.

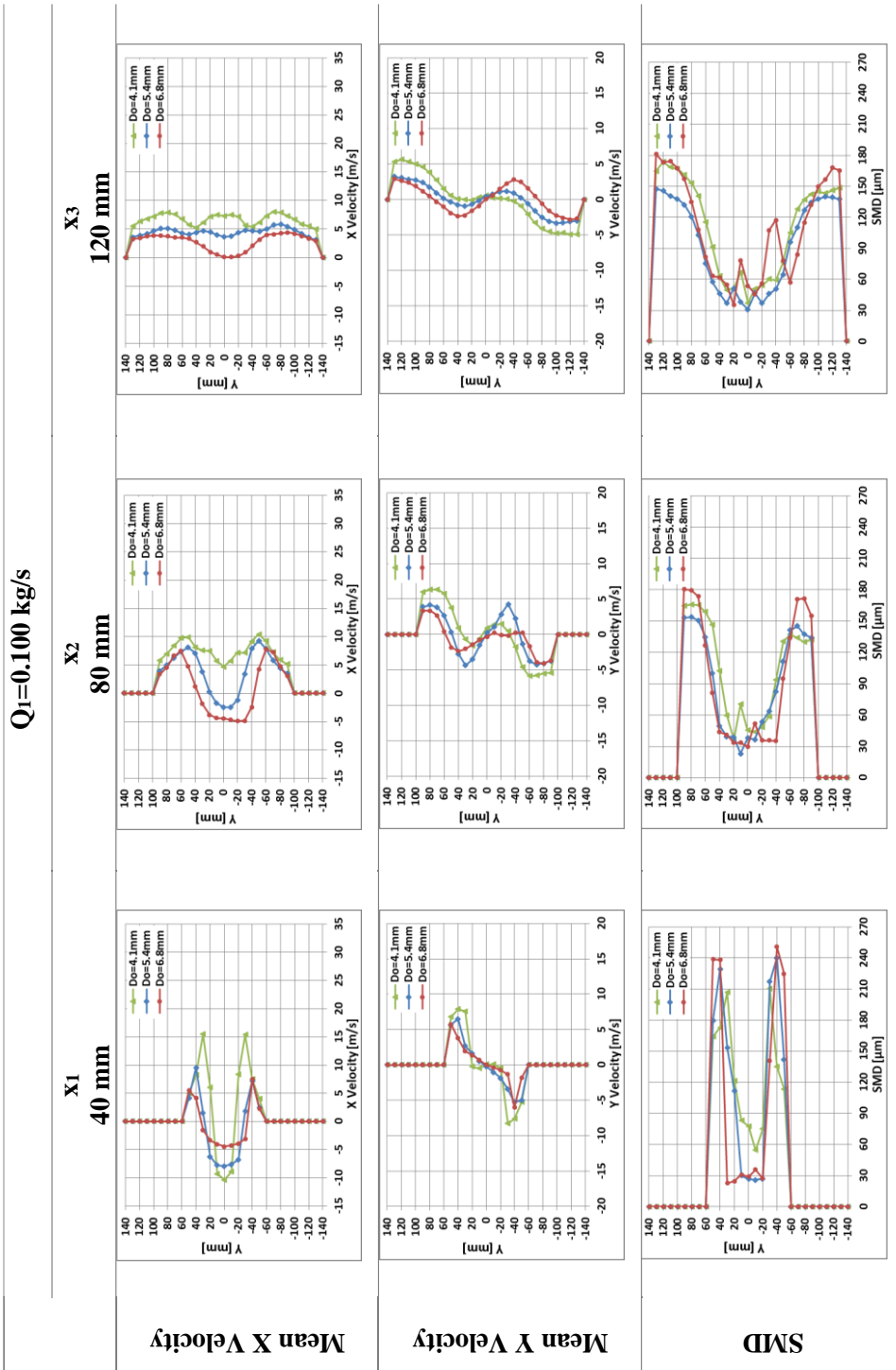


Figure 4.7. Comparison of the Effect of Nozzle Diameter on the Microscopic Properties for $Q_1=0.100 \text{ kg/s}$ at Specified x Coordinates.

$Q_2=0.173 \text{ kg/s}$

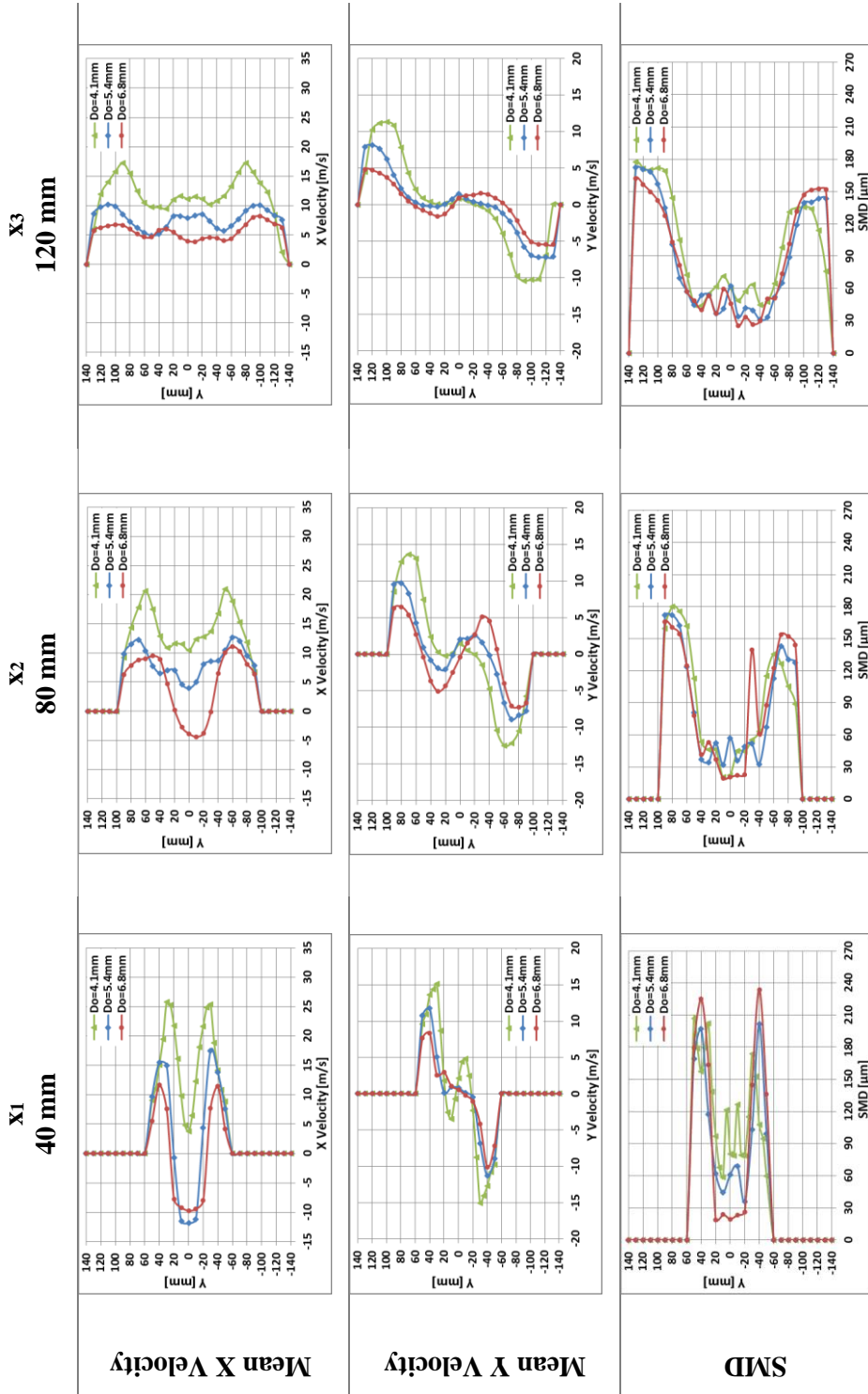


Figure 4.8. Comparison of the Effect of Nozzle Diameter on the Microscopic Properties for $Q_2=0.173 \text{ kg/s}$ at Specified x Coordinates.

$Q_3=0.240$ kg/s

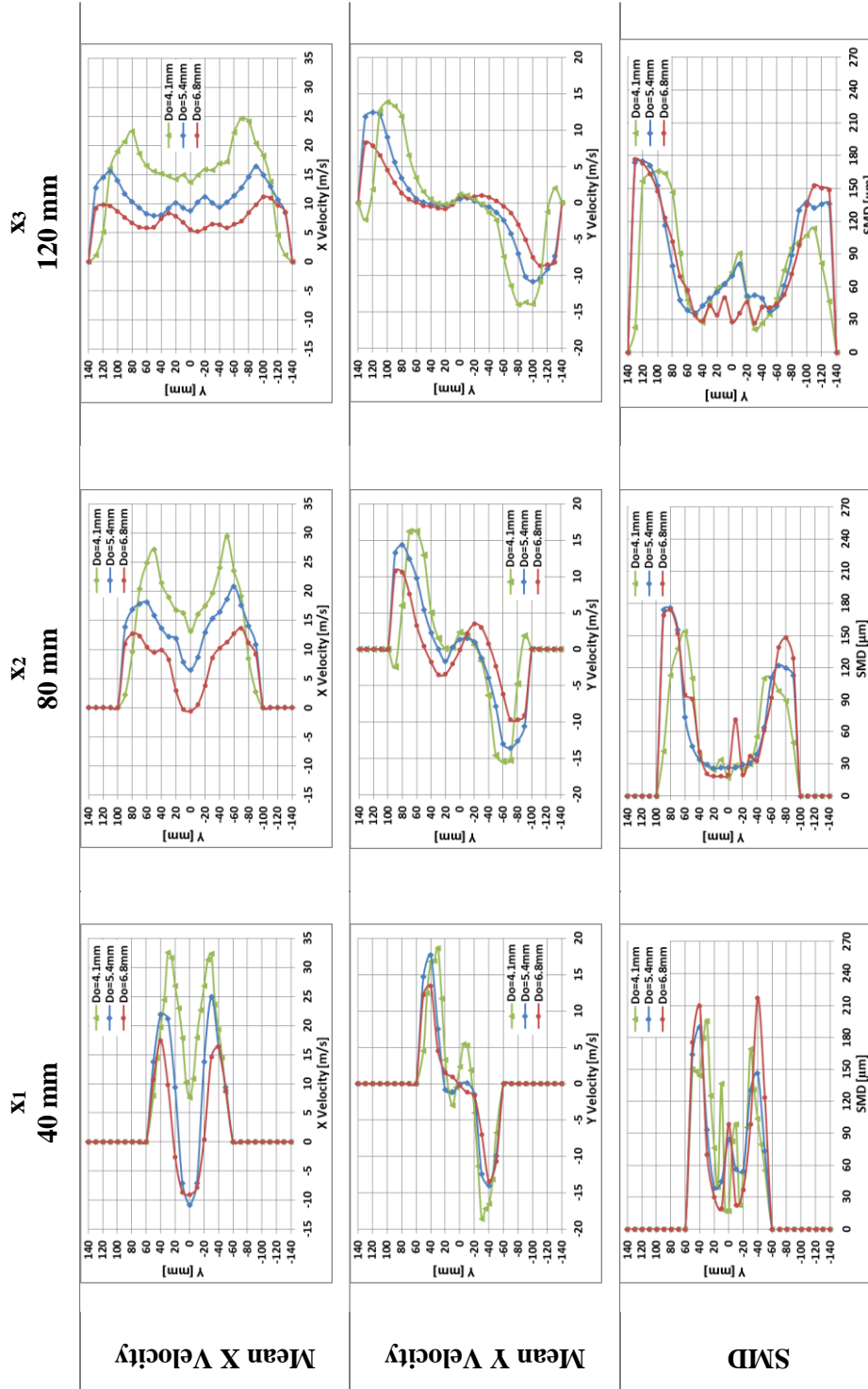


Figure 4.9. Comparison of the Effect of Nozzle Diameter on the Microscopic Properties for $Q_3=0.240$ kg/s at Specified x Coordinates

4.2.2. Nozzle Length Effect on the Microscopic Properties

In order to research the effect of nozzle length on the microscopic properties experimental studies are performed with A-6 ($L_o=8.1$ mm), A-1 ($L_o=10.2$ mm), and A-7 ($L_o=13.5$ mm), and results are given in Figure 4.10, Figure 4.11, and Figure 4.12 for Q_1 , Q_2 , and Q_3 , respectively. The contours and streamlines are plotted from at $x=20$ mm.

As shown in contours of mean velocity, revealed vortex at the exit of the atomizer remains almost the same for three different nozzle lengths.

Mean x velocity contours of A-6, A-1, and A-7 for $Q_1=0.100$ kg/s are given in Figure 4.10. Mean x velocity of the droplets does not change with increasing nozzle length. The maximum mean x velocity is measured as 10.65 m/s, 10.49 m/s, and 10.17 m/s for A-6, A-1, and A-7, respectively. For each nozzle length, increasing x-coordinate leads to a decrease in the mean x velocity of droplets.

Mean y velocity contours of A-6, A-1, and A-7 for $Q_1=0.100$ kg/s are given in Figure 4.10. As shown in figure, increasing nozzle length has no significant effect on mean y velocity of the droplets. The maximum value of mean y velocity is measured as 9.12 m/s, 8.65 m/s, and 8.92 m/s for A-6, A-1, and A-7, respectively. Also, a decrease is observed in the mean y velocity of droplets with increasing x-coordinate for each nozzle length.

The SMD contours of A-6, A-1, and A-7 for $Q_1=0.100$ kg/s are given in Figure 4.10. As shown in the SMD contours, the small droplets, which have small SMD values, are positioned in the center of the spray, and an increase is obtained in SMD with y coordinate and reaches the maximum value on the liquid jet. Increasing nozzle length increases the frictional losses of the nozzle and decreases the energy of liquid due to the more interaction between the liquid and nozzle wall. But it is observed from the results that variation of the nozzle length between 8.1 mm and 13.5 mm has very little influence on the SMD values of spray.

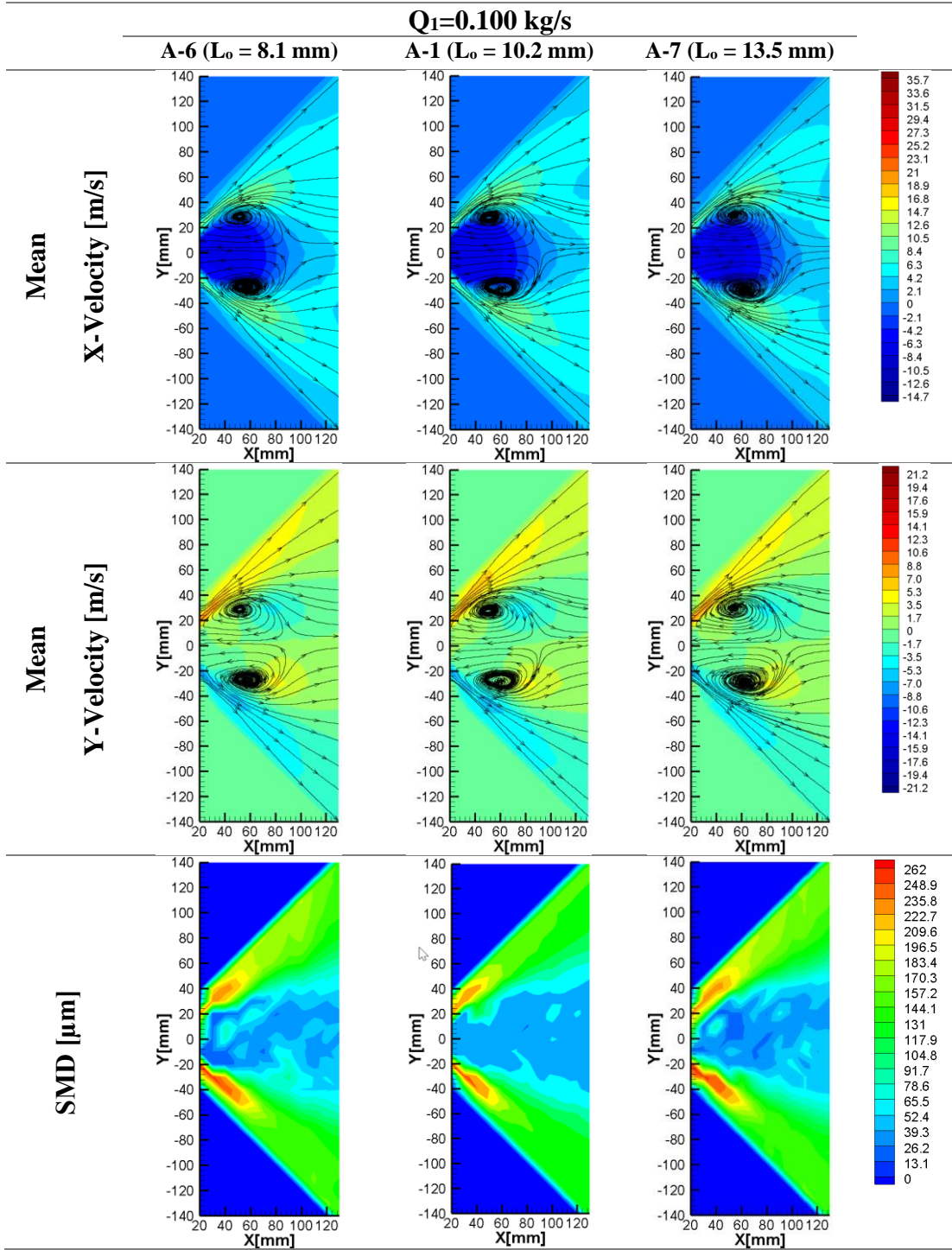


Figure 4.10. Nozzle Length Effect on the Microscopic Properties for Q_1

In order to investigate the nozzle length effect at different mass flow rates, experiments are repeated for Q_2 and Q_3 , and results are given in Figure 4.11 and Figure 4.12. As shown in mean velocity and SMD contours, it is obtained that increasing nozzle length has no significant effect on the microscopic properties at increased mass flow rates.

The measured mean x velocity and mean y velocity values remain almost the same with increasing nozzle length for different mass flow rates. The maximum mean x velocity of the particles is 18.28 m/s, 18.70 m/s, and 17.67 m/s, and the maximum mean y velocity of the particles is 15.28 m/s, 15.54 m/s, and 14.90 m/s for A-6, A-1, and A-7 at $Q_2=0.173$ kg/s, respectively. The maximum mean x velocity of the particles is 25.17 m/s, 24.88 m/s, and 24.45 m/s, and the maximum mean y velocity of the particles is 20.74 m/s, 20.52 m/s, and 20.65 m/s for A-6, A-1, and A-7 at $Q_3=0.240$ kg/s, respectively.

As given in the SMD contours, change of the nozzle length between 8.1 mm and 13.5 mm has very little influence on the SMD values of spray for Q_2 and Q_3 .

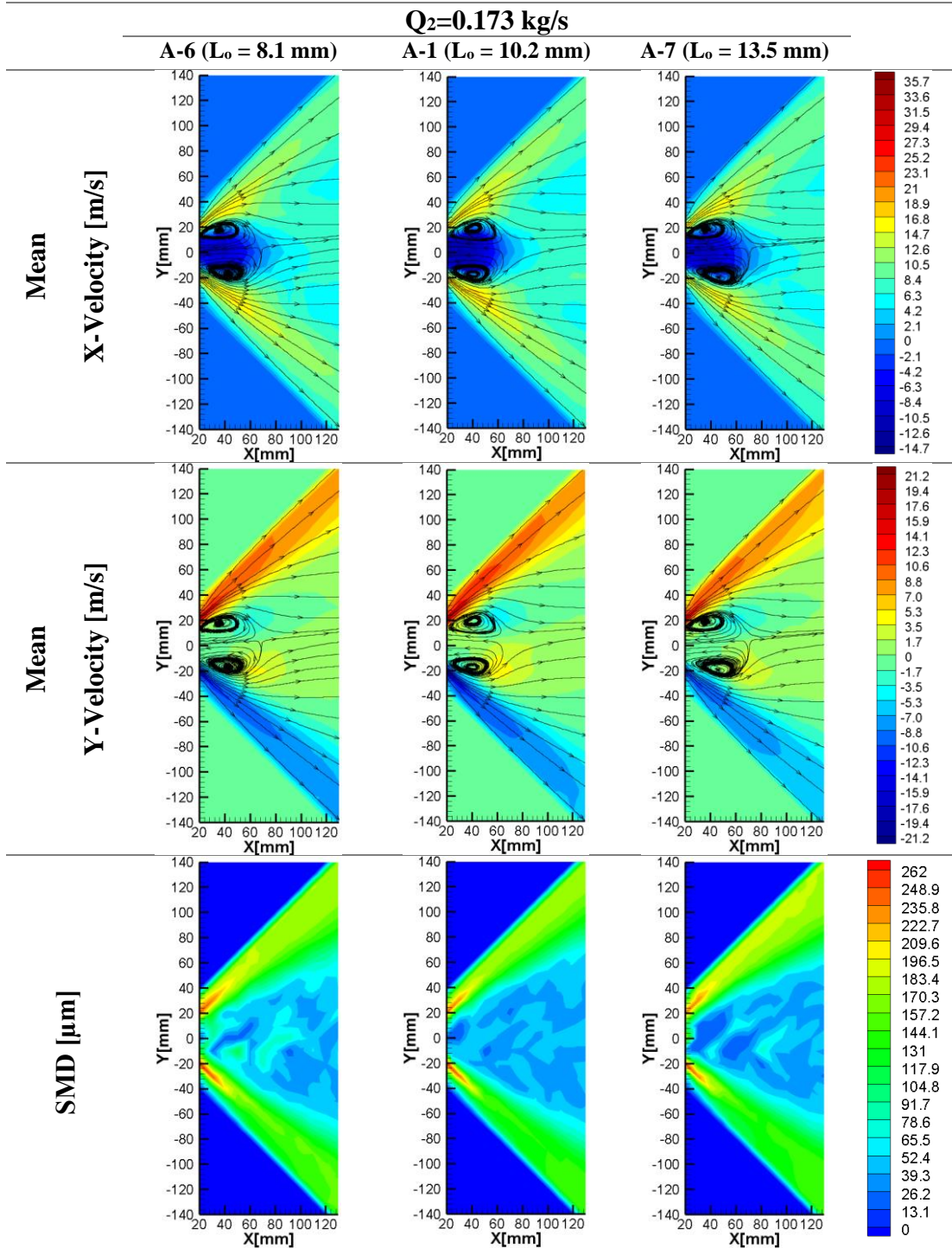


Figure 4.11. Nozzle Length Effect on the Microscopic Properties for Q_2

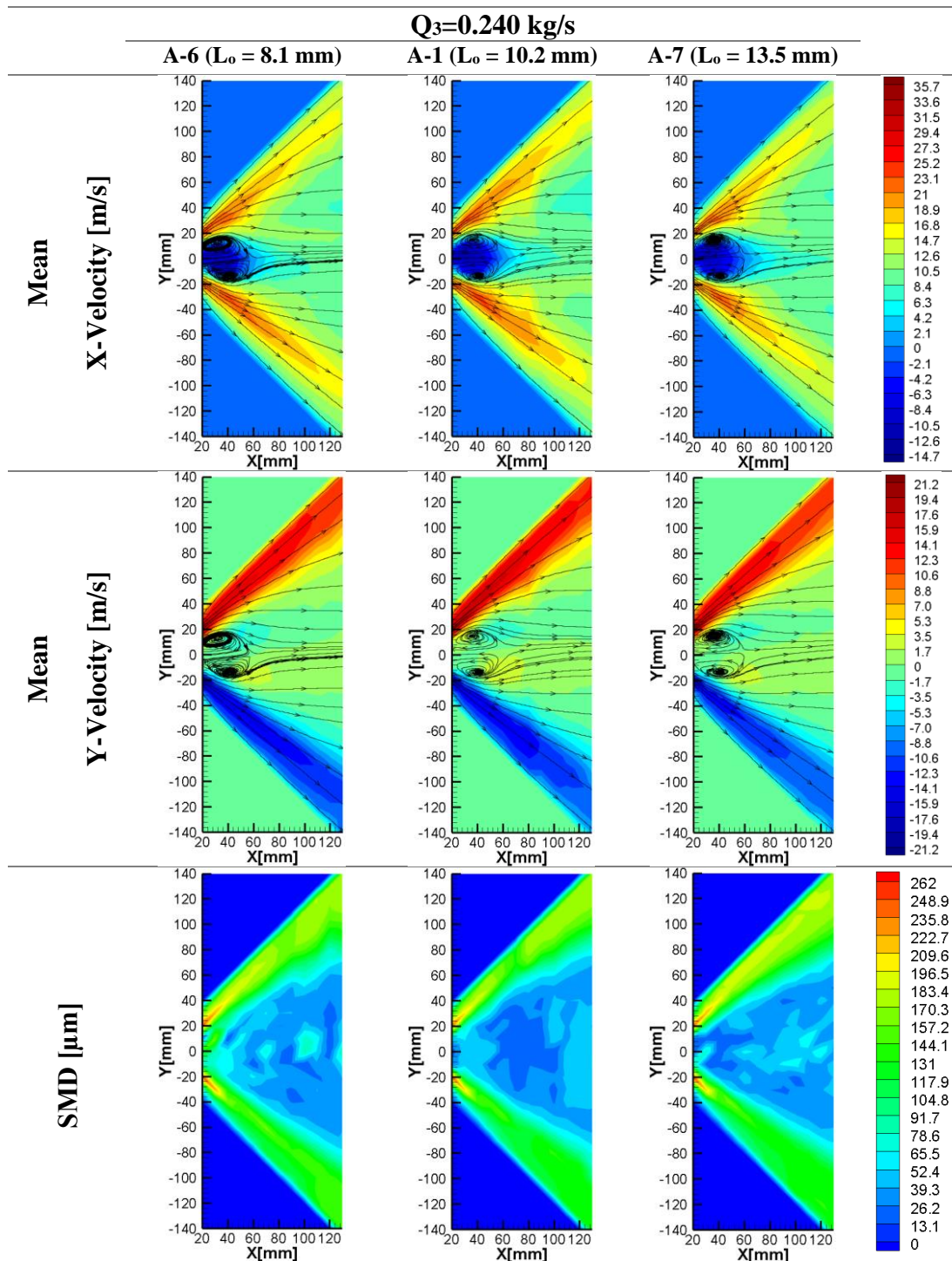


Figure 4.12 Nozzle Length Effect on the Microscopic Properties for Q_3

In order to compare the results, mean x velocity, mean y velocity, and SMD values at $x=40$ mm, 80 mm, and 120 mm are plotted for A-6, A-1, and A-7. Comparison graphics are given in Figure 4.13, Figure 4.14, and Figure 4.15 for Q_1 , Q_2 , and Q_3 , respectively. As shown in the graphics, velocity and SMD plots are almost the same at designated x locations for three different nozzle length. Therefore, it can be said that nozzle length has no significant effect on microscopic properties.

$Q_1=0.100 \text{ kg/s}$

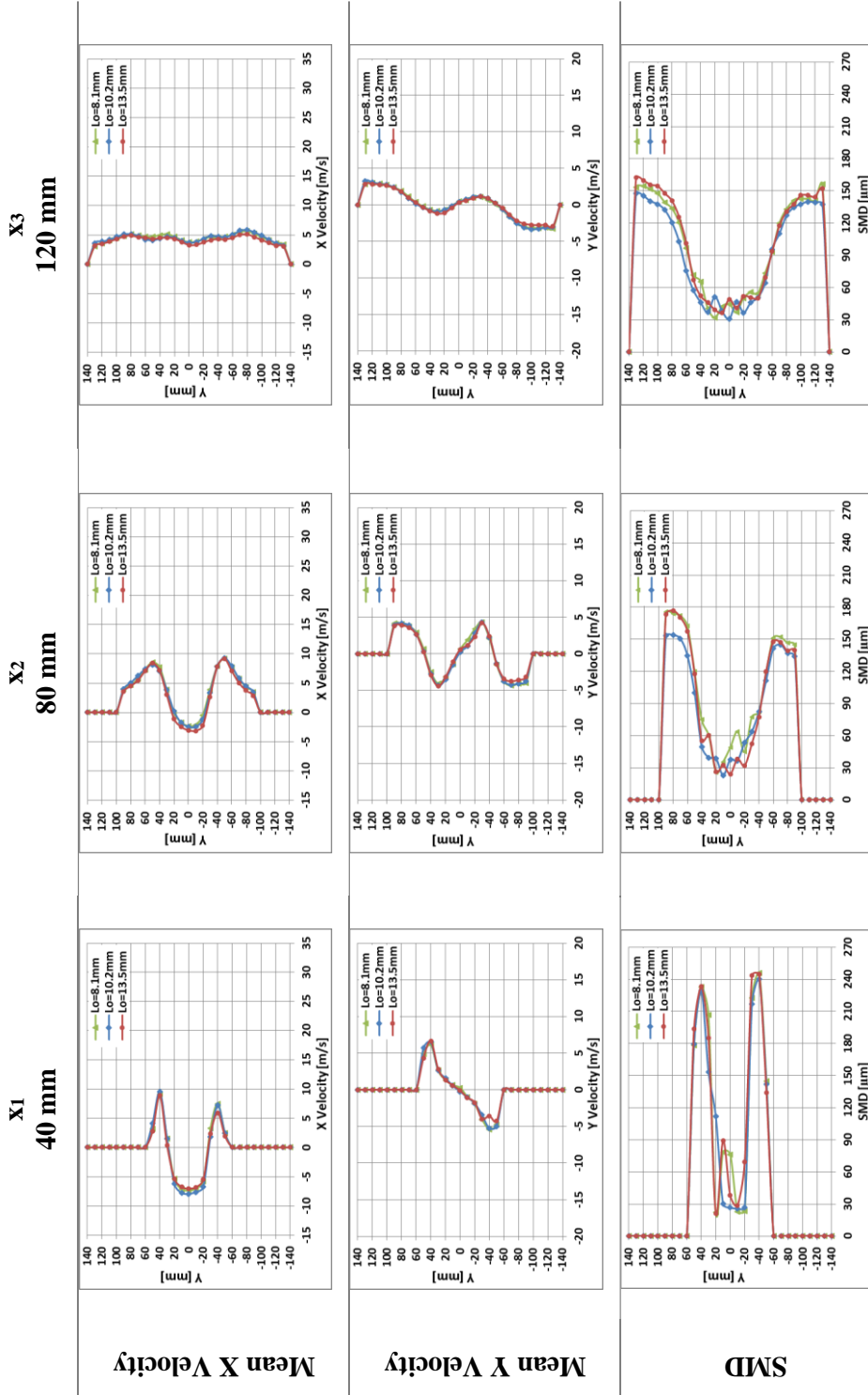


Figure 4.13. Comparison of the Nozzle Length Effect on the Microscopic Properties for $Q_1=0.100 \text{ kg/s}$ at Specified x Coordinates.

$Q_2=0.173 \text{ kg/s}$

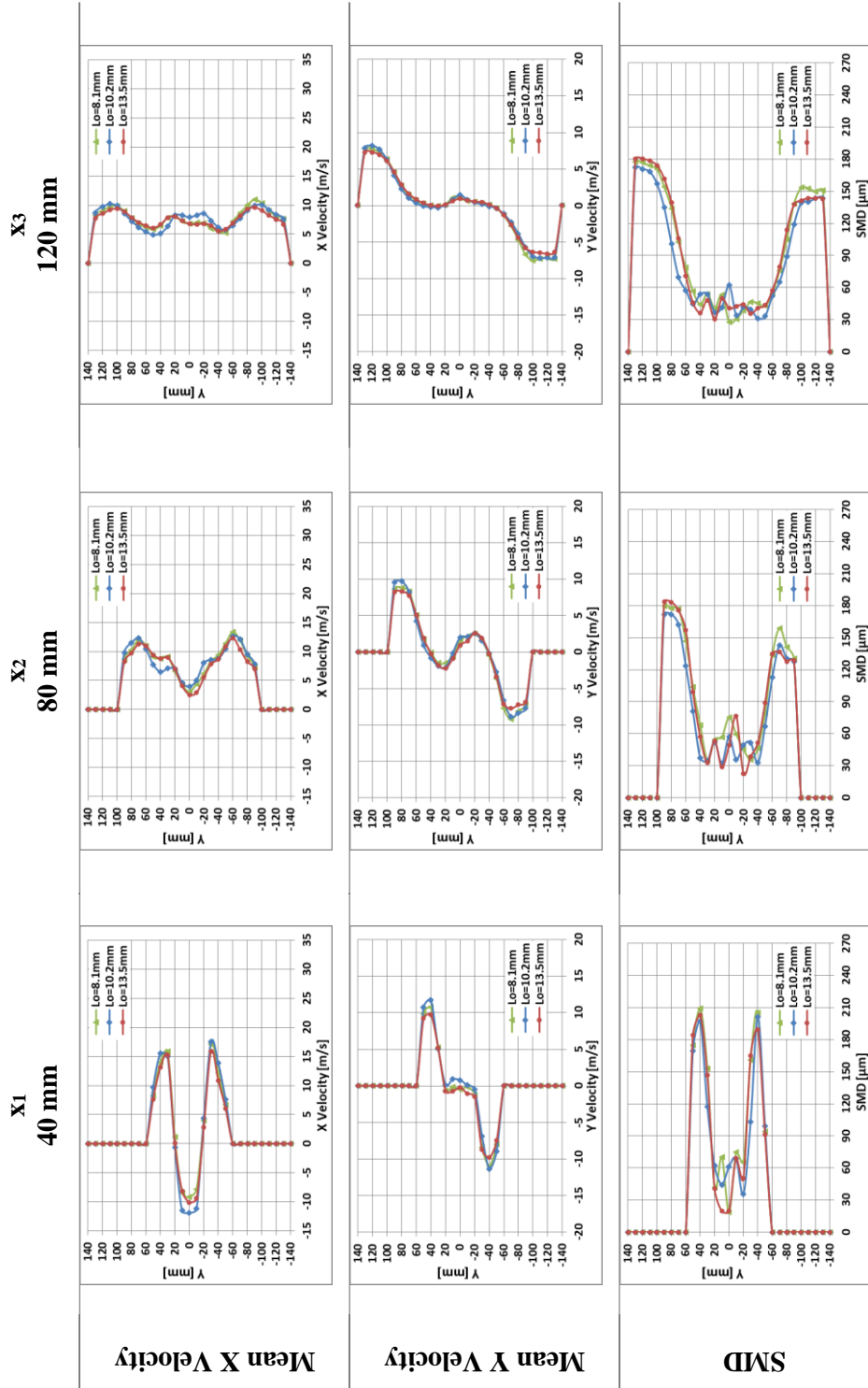


Figure 4.14. Comparison of Nozzle Length Effect on the Microscopic Properties for $Q_2=0.173 \text{ kg/s}$ at Specified x Coordinates.

$Q_3=0.240 \text{ kg/s}$

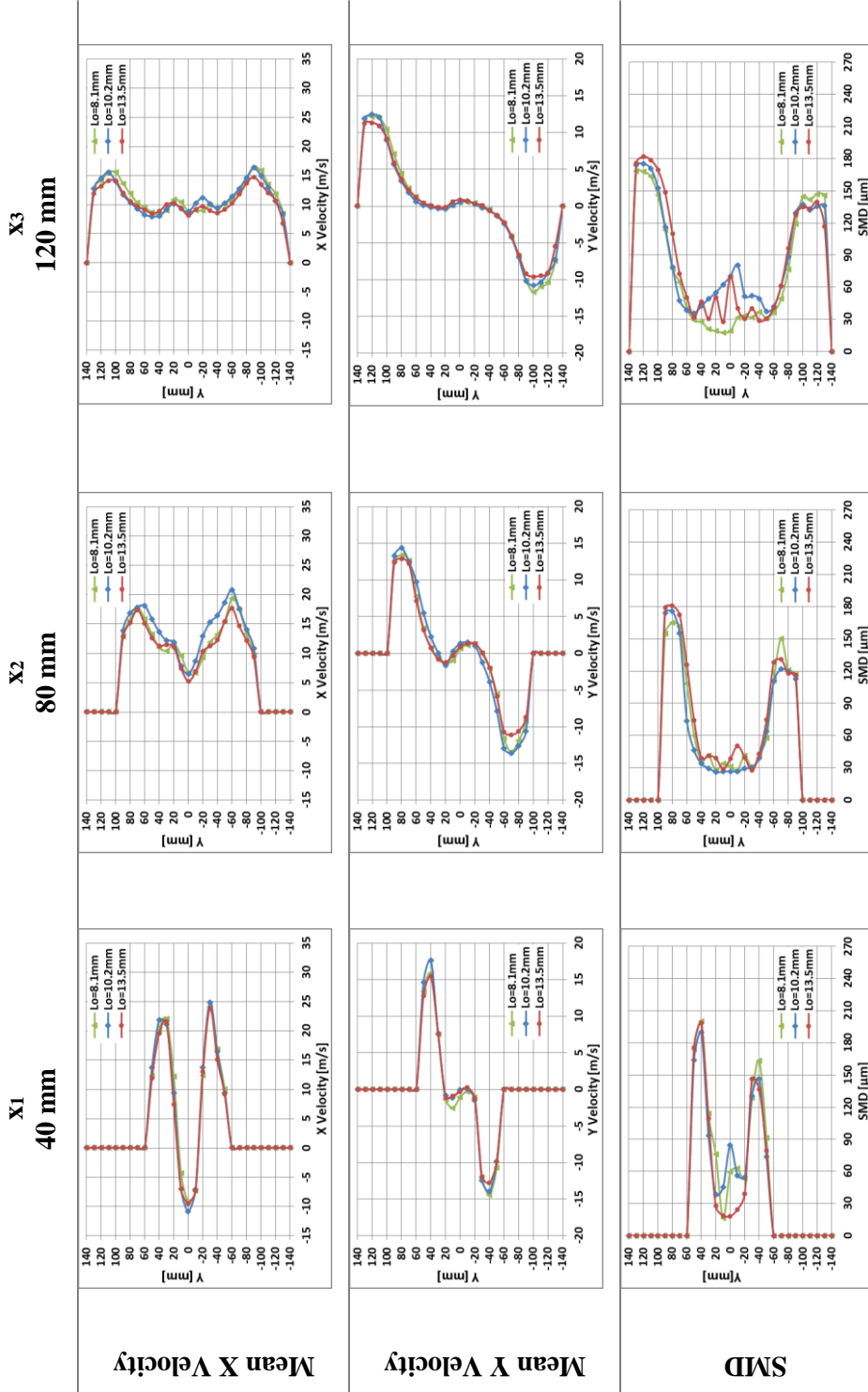


Figure 4.15. Comparison of Nozzle Length Effect on the Microscopic Properties for $Q_3=0.240 \text{ kg/s}$ at Specified x Coordinates.

4.2.3. Tangential Port Number Effect on the Microscopic Properties

In order to study the effect of tangential port number on the microscopic properties, experimental studies are performed with A-5 ($N_{tp}=2$), A-4 ($N_{tp}=4$), and A-1 ($N_{tp}=6$), and results are denoted in Figure 4.16, Figure 4.17, and Figure 4.18 for Q_1 , Q_2 , and Q_3 , respectively. The contours and streamlines are plotted from at $x=20$ mm.

As shown in contours of mean velocity, change of tangential port number has no significant effect on revealed vortex at the exit of the atomizer. The revealed vortex remains almost the same for three different tangential port numbers.

Mean x velocity contours of A-5, A-4, and A-1 for $Q_1=0.100$ kg/s are given in Figure 4.16. As shown in the figure, increasing tangential port number does not significantly change the mean x velocity of the particles. The maximum mean x velocity is measured as 10.36 m/s, 11.17 m/s, and 10.49 m/s for A-5, A-4, and A-1, respectively. It is also obtained that; the mean x velocity of particles decreases with increasing x-coordinate for each tangential port number.

Mean y velocity contours of A-5, A-4, and A-1 for $Q_1=0.100$ kg/s are given in Figure 4.16. Mean y velocity of the droplets does not significantly change with increasing tangential port number. The maximum mean y velocity is measured as 8.57 m/s, 8.28 m/s, and 8.65 m/s for A-5, A-4, and A-1, respectively. The mean y velocity of particles decreases with increasing x-coordinate for each tangential port number.

The SMD contours of A-5, A-4, and A-1 for $Q_1=0.100$ kg/s are given in Figure 4.16. As shown in the figure, increasing tangential port number has a positive effect on the distribution of the particles for the atomizer. The results show that uniformity of particles is higher with six tangential ports than four and two tangential ports. The droplet distributions of spray for the atomizers with two and four tangential ports are irregular, and there are big particles near the axis of the hollow cone spray. On the other hand, the small droplets are located at the center of the spray, and an increase is observed in droplet diameter with y coordinate and reaches the maximum value on the

liquid jet for atomizer with six tangential ports. The uniformity is increased with increasing tangential port number.

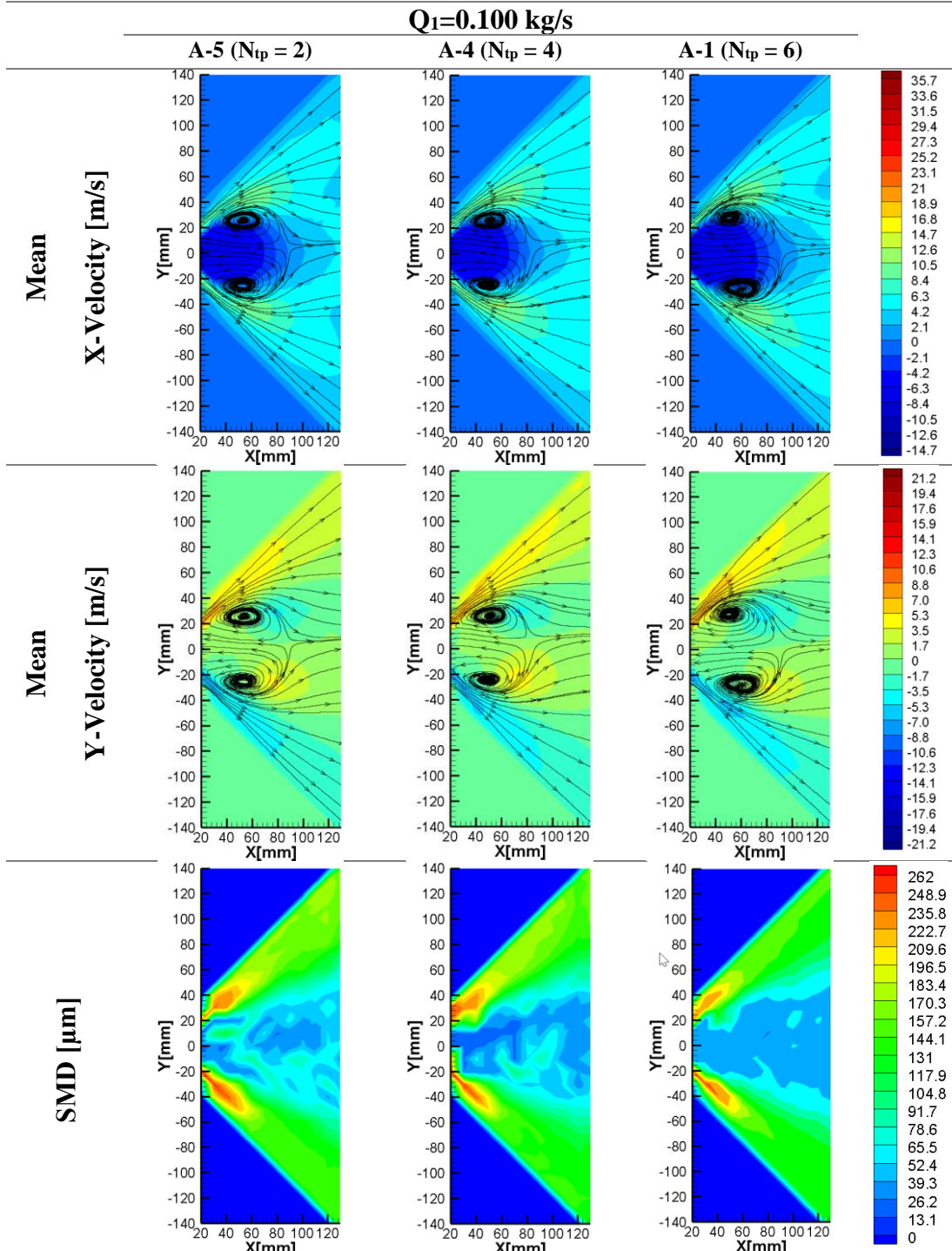


Figure 4.16. Tangential Port Number Effect on the Microscopic Properties for Q_1

In order to investigate the tangential port number effect at different mass flow rates experiments are repeated for Q_2 and Q_3 , and results are given in Figure 4.17 and Figure 4.18. As shown in mean velocity and SMD contours, when the mass flow rate is increased, changing tangential port number leads to similar effects on the microscopic properties as the flow rate is $Q_1=0.100$ kg/s.

As shown in the figures, increasing tangential port number has no significant effect on mean velocities at Q_2 and Q_3 , too. The maximum mean x velocity of the particles is 17.96 m/s, 18.70 m/s, and 18.70 m/s, and the maximum mean y velocity of the particles is 14.89 m/s, 14.71 m/s, and 15.54 m/s for A-5, A-4, and A-1 at $Q_2=0.173$ kg/s, respectively. The maximum mean x velocity of the particles is 25.12 m/s, 26.80 m/s, and 24.88 m/s, and the maximum mean y velocity of the particles is 19.96 m/s, 20.51 m/s, and 20.52 m/s for A-5, A-4, and A-1 at $Q_3=0.240$ kg/s, respectively.

As shown in the SMD contours, increasing tangential port number results in an increased uniformity of the droplet distribution in the spray for higher mass flow rate values. The uniformity of droplet distribution is higher with six tangential ports than four and two tangential ports for Q_2 and Q_3 .

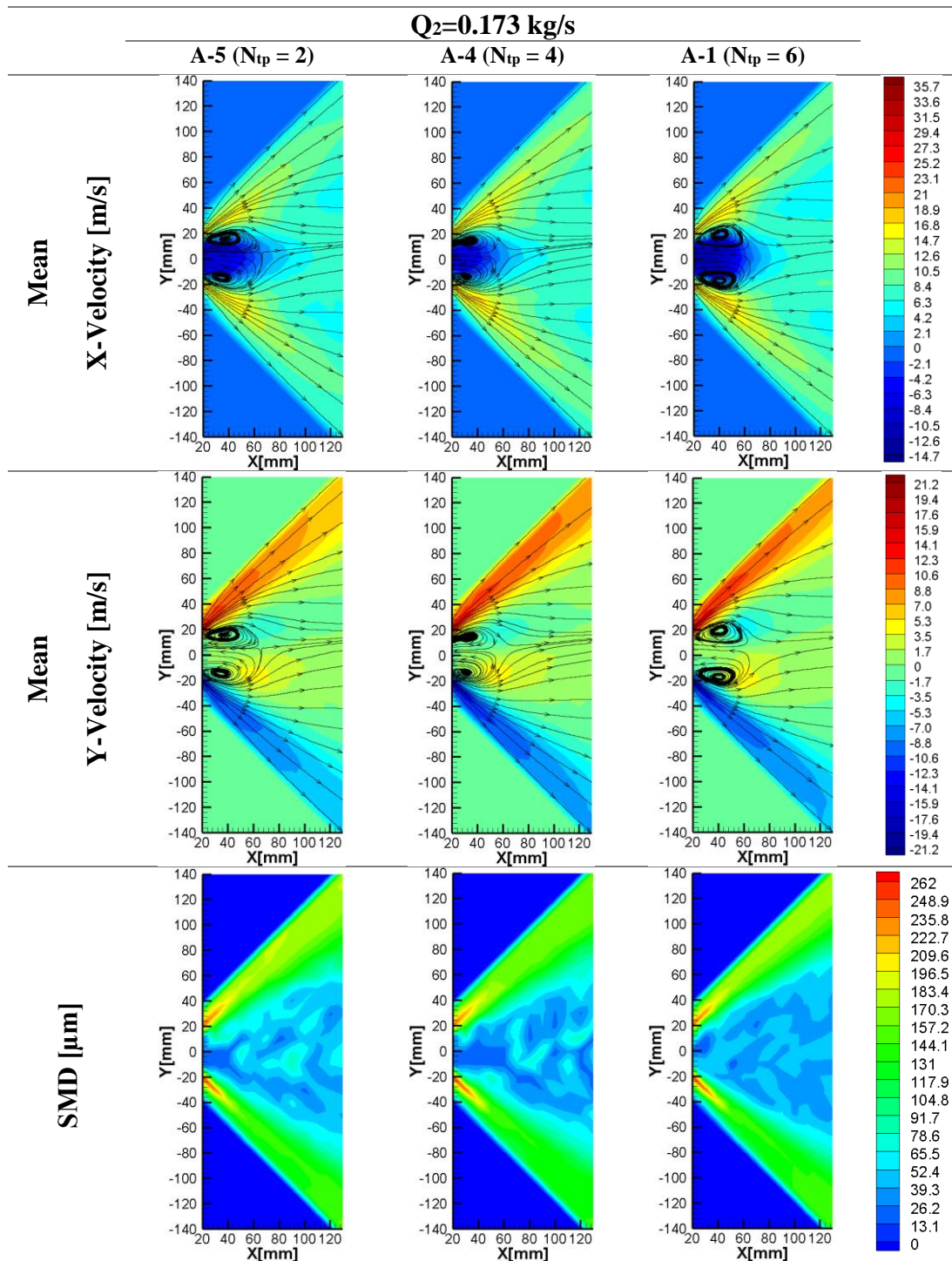


Figure 4.17. Tangential Port Number Effect on the Microscopic Properties for Q_2

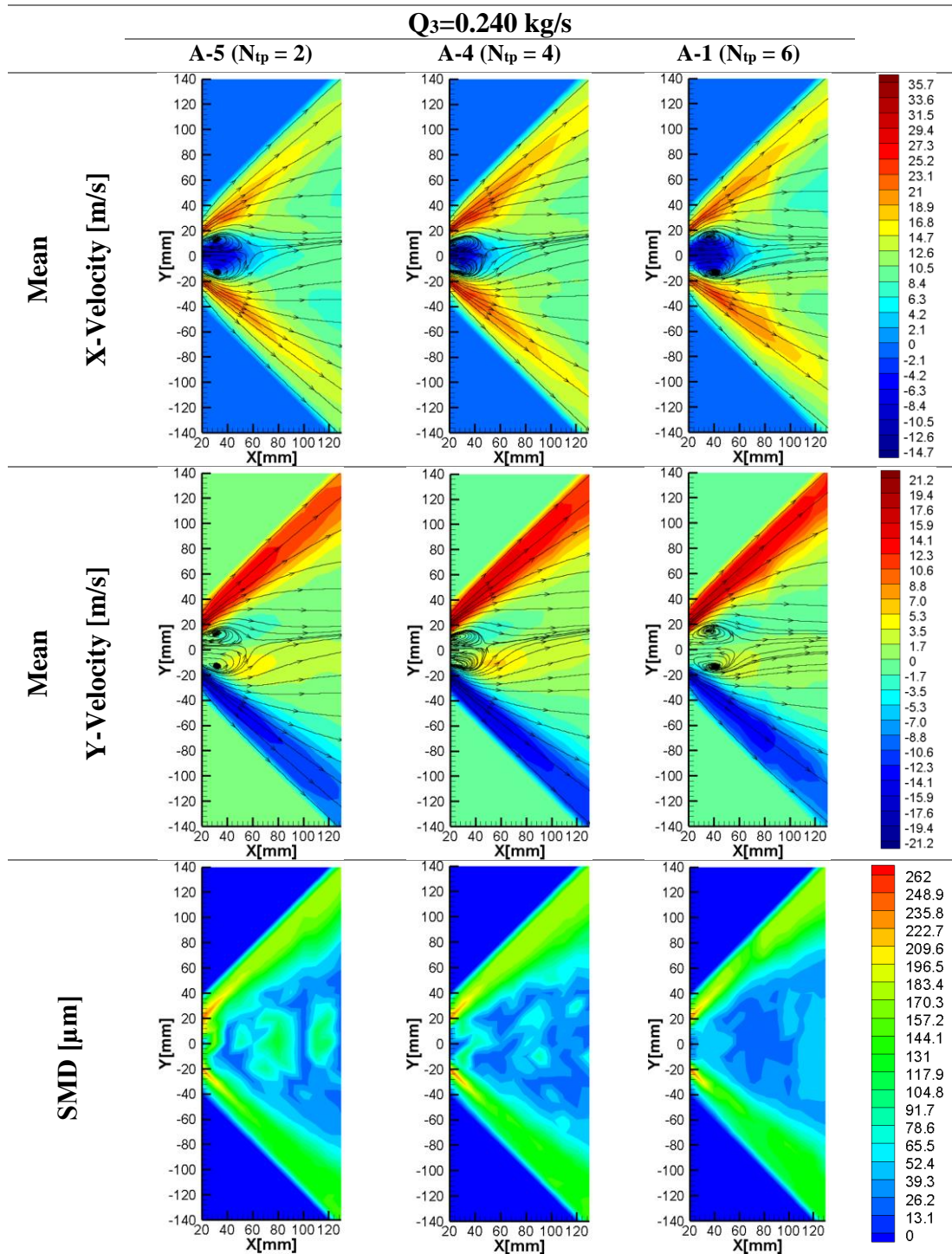


Figure 4.18. Tangential Port Number Effect on the Microscopic Properties for Q_3

In order to compare the results, mean x velocity, mean y velocity, and SMD values at $x=40$ mm, 80 mm and 120 mm are plotted for A-5, A-4, and A-1. Comparison graphics are given in Figure 4.19, Figure 4.20, and Figure 4.21 for Q_1 , Q_2 , and Q_3 , respectively.

As shown in the velocity graphics plotted for designated x locations, velocity profiles are almost the same for three different tangential port number, and it can be said that tangential port number has a negligible impact on velocity. However, increasing tangential port number has a positive impact on SMD distribution. As shown in comparison graphics, SMD distributions are more uniform in the center of the spray for six tangential ports, but decreasing port number increases the droplet diameter oscillations near the axis of the spray.

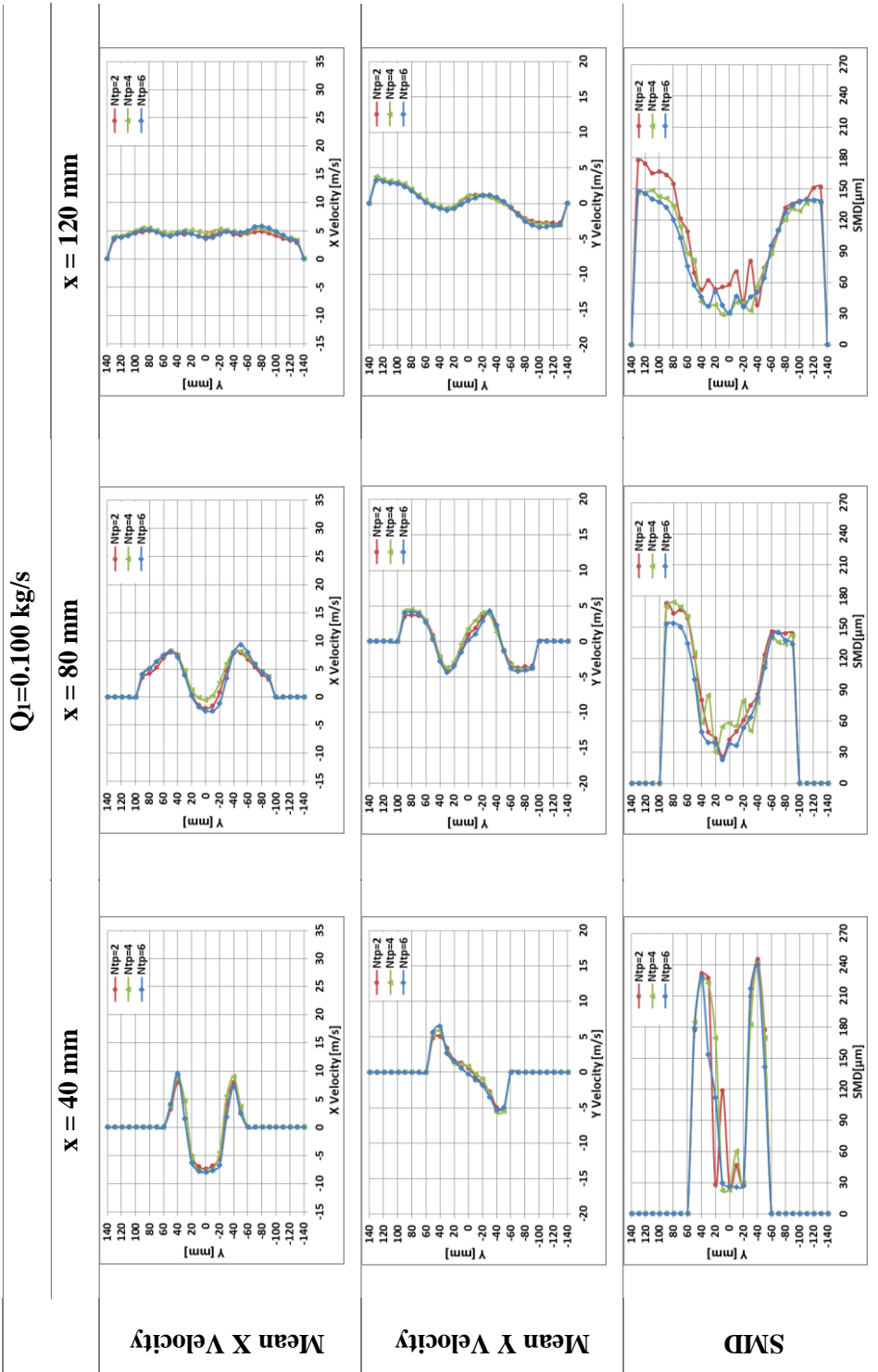


Figure 4.19. Comparison of Tangential Port Number Effect on the Microscopic Properties for $Q_1=0.100 \text{ kg/s}$ at Specified x Coordinates

$Q_2=0.173 \text{ kg/s}$

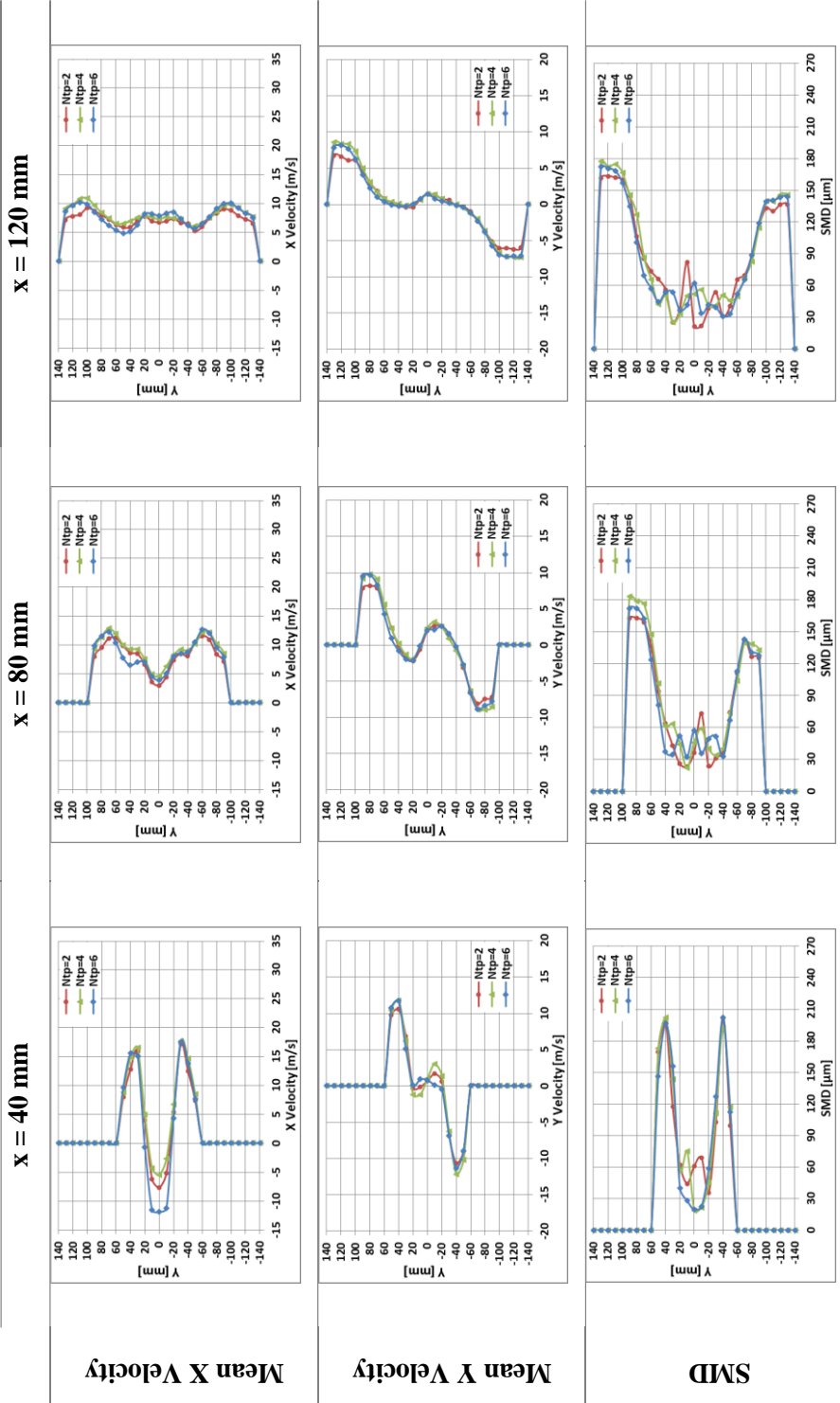


Figure 4.20. Comparison of Tangential Port Number Effect on the Microscopic Properties for $Q_2=0.173 \text{ kg/s}$ at Specified x Coordinates

$Q_3=0.240$ kg/s

x = 120 mm

x = 80 mm

x = 40 mm

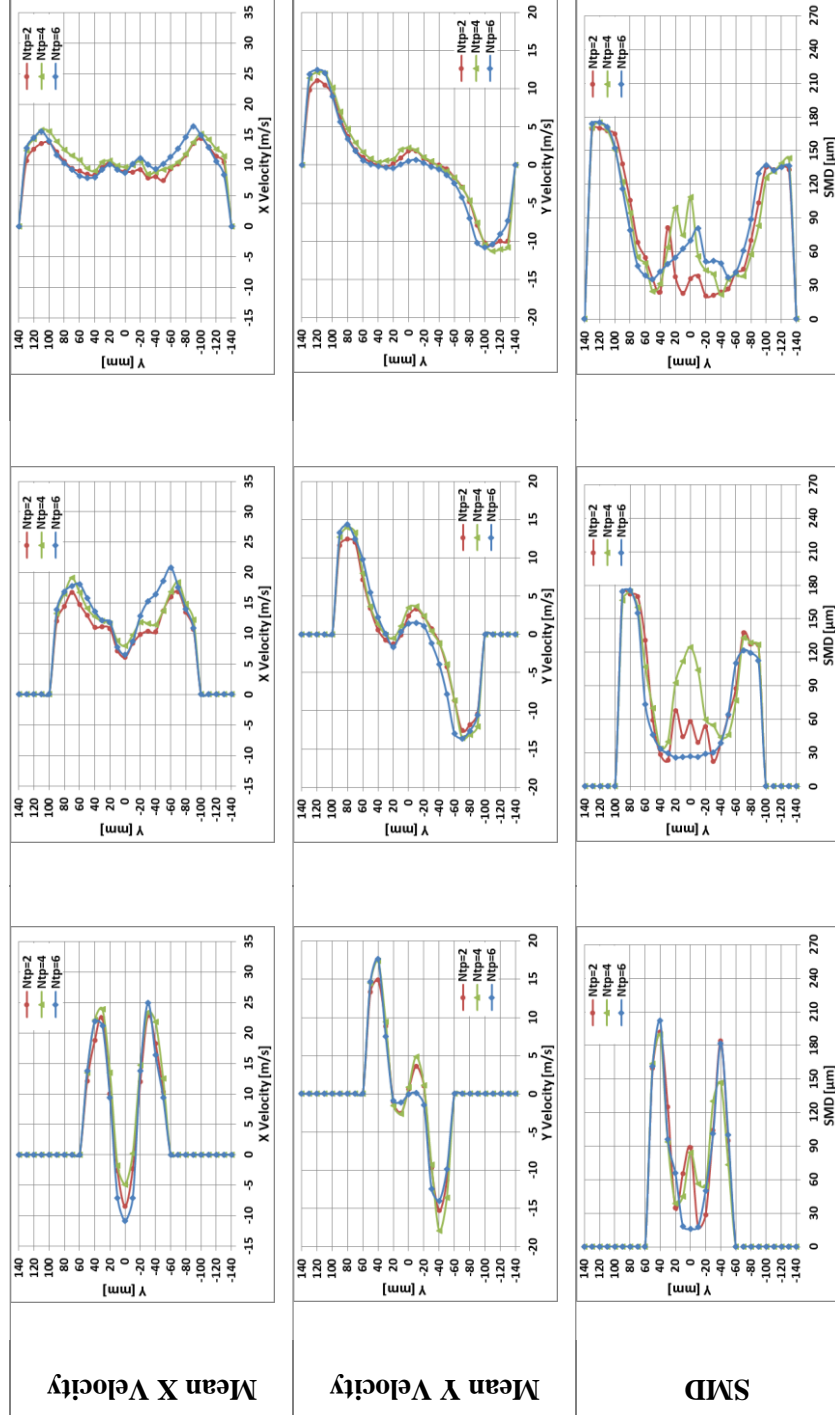


Figure 4.21. Comparison of Tangential Port Number Effect on the Microscopic Properties for $Q_3=0.240$ kg/s at Specified x Coordinates.

4.2.4. Mass Flow Rate Effect on the Microscopic Properties

In order to research the effect of mass flow rate on the microscopic properties experimental studies are performed with seven test atomizers for Q_1 , Q_2 , and Q_3 .

In order to compare the results for three mass flow rates, mean x velocity, mean y velocity, and SMD values at $x=40$ mm, 80 mm, and 120 mm are plotted for A-1. The contours and comparison graphics are given in Figure 4.22 and Figure 4.23, respectively. The comparison graphics for other atomizers are given in Appendix A.

As shown in the contours of mean velocities (Figure 4.22), the revealed vortex at the exit of the atomizer becomes smaller and approaches to the exit of the atomizer with higher mass flow rate values. It is also investigated that mean velocity values of the particles on liquid jet increases with increasing mass flow rate.

As demonstrated in the SMD contours (Figure 4.22), a coarse spray is obtained at low mass flow rates. Increasing mass flow rate leads to an increase in velocities of the liquid. The liquid exits from the nozzle with a higher velocity which causes more effective disturbances on the hollow cone spray. These effective disturbances increase the instabilities which would help to break up liquid into smaller droplets, lead to a better atomization and a decline in SMD.

It is also observed that increasing mass flow rate results in more unstable waves on the surface of the spray and because of that breakup appears much closer to the exit of nozzle.

As shown in comparison graphics of X and Y velocities (Figure 4.23), increasing mass flow rate causes an increase in magnitude of velocities on the spray. The revealed vortex at the nozzle exit becomes smaller and comes close to the nozzle exit with increasing mass flow rate.

As demonstrated in comparison graphics of SMD (Figure 4.23), increasing mass flow rate causes a decrease in SMD values of particles near the nozzle exit. Furthermore,

effect of increasing mass flow rate loses its strength on SMD of particles away from the nozzle exit.

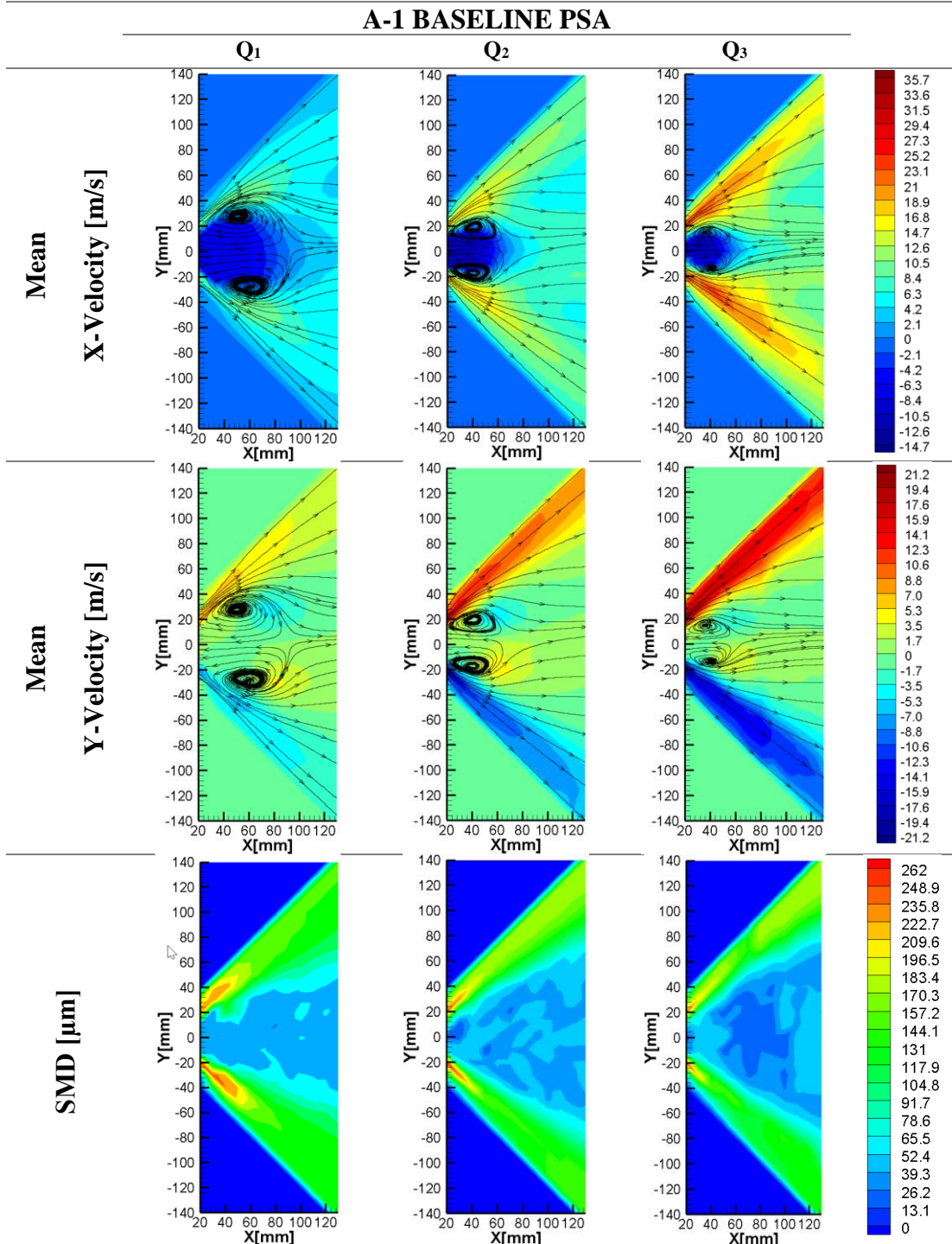


Figure 4.22. Mass Flow Rate Effect on the Microscopic Properties of Baseline PSA

A-1 BASE LINE ATOMIZER

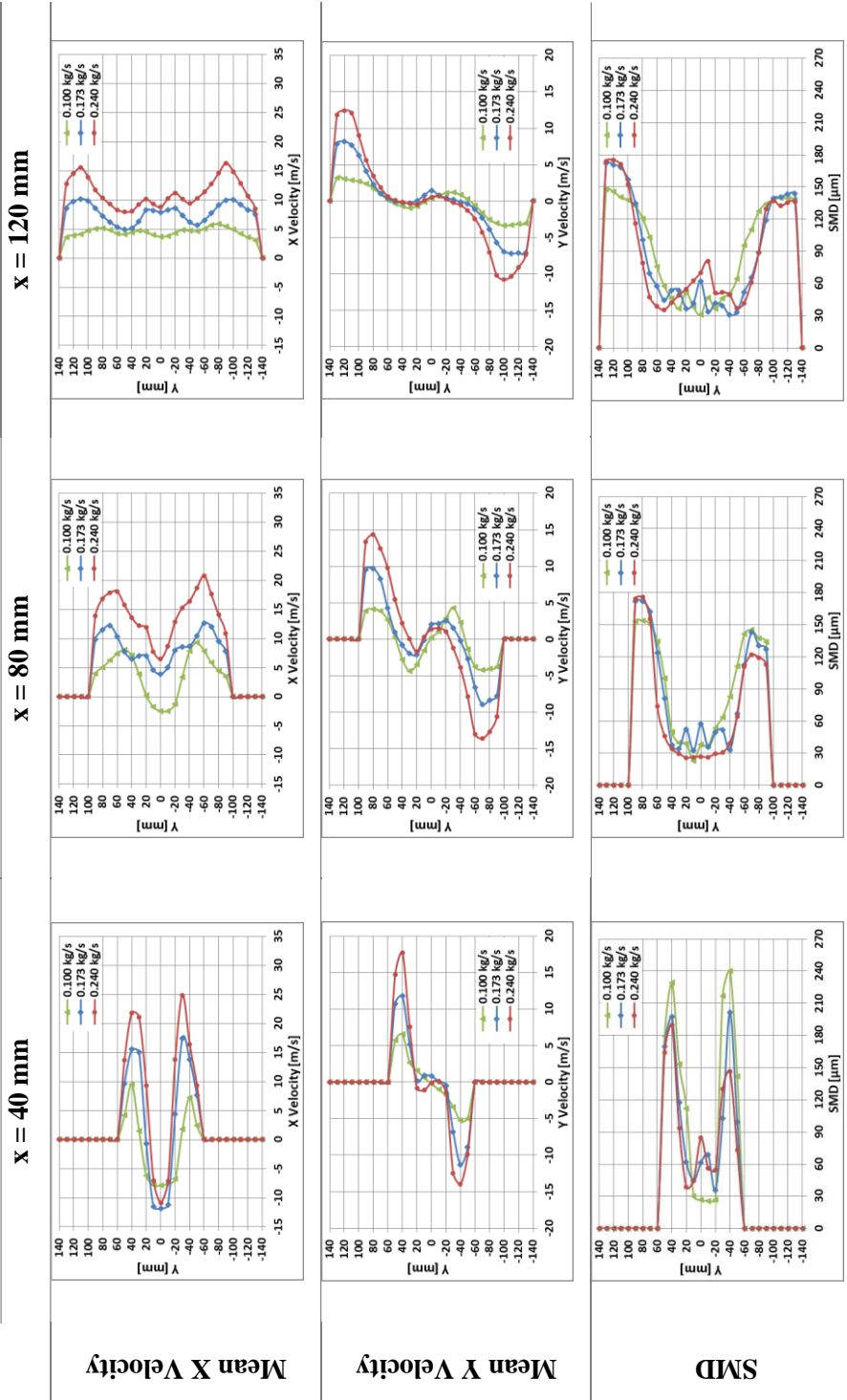


Figure 4.23. Comparison of Mass Flow Rate Effect on the Microscopic Properties of Baseline PSA at Specified x Coordinates.

4.3. Results of Pressure Drop Measurements

Mean pressure drop values are measured for seven test atomizers at Q_1 , Q_2 , and Q_3 .

In order to investigate the effect of nozzle diameter on pressure drop, mean pressure drop values of A-2, A-1, and A-3 are measured and results are given in Table 4.9.

Table 4.9. Mean Pressure Drop Values of Atomizers as a Function of Nozzle Diameter at Different Mass Flow Rates

	Mean Pressure Drop [bar]		
	Q_1	Q_2	Q_3
A-2 ($D_o=4.1$ mm)	3.80	10.50	19.40
A-1 ($D_o=5.4$ mm)	2.42	5.72	10.34
A-3 ($D_o=6.8$ mm)	1.86	3.84	6.80

As presented in Table 4.9, mean pressure drop value decreases with increasing nozzle diameter at different mass flow rates.

In order to examine the effect of nozzle length on pressure drop, mean pressure drop values of A-6, A-1, and A-7 are measured and results are given in Table 4.10.

Table 4.10. Mean Pressure Drop Values of Atomizers as a Function of Nozzle Length at Different Mass Flow Rates

	Mean Pressure Drop [bar]		
	Q_1	Q_2	Q_3
A-6 ($L_o=8.1$ mm)	2.30	5.25	9.83
A-1 ($L_o=10.2$ mm)	2.42	5.72	10.34
A-7 ($L_o=13.5$ mm)	2.41	5.48	10.01

As presented in Table 4.10, change in mean pressure drop due to the increase in nozzle length is negligible at different mass flow rates.

In order to investigate the effect of tangential port number on pressure drop, mean pressure drop values of A-5, A-4, and A-1 are measured and results are given in Table 4.11.

Table 4.11. *Mean Pressure Drop Values of Atomizers as a Function of Tangential Port Number at Different Mass Flow Rates*

	Mean Pressure Drop [bar]		
	Q₁	Q₂	Q₃
A-5 (N_{tp}=2)	2.40	5.80	10.87
A-4 (N_{tp}=4)	2.51	6.08	11.63
A-1 (N_{tp}=6)	2.42	5.72	10.34

As presented in Table 4.11, change in mean pressure drop due to the increase in tangential port number is negligible at different mass flow rates.

It is also observed from the results given in Table 4.9, Table 4.10, and Table 4.11 that increasing mass flow rate results in an increase in the pressure drop for all geometrical configurations.

All measured mean pressure drop values have a 0.5% error margin caused by pressure transducer.

CHAPTER 5

RESULTS OF NUMERICAL STUDY

5.1. Introduction

Two-dimensional axisymmetric swirl flow simulations are carried out and the liquid-gas phase interactions are examined.

5.2. Numerical Simulation Results

In this section, two-dimensional axis-symmetric simulations and their results are examined to understand the PSA flow.

5.2.1. Pressure Swirl Atomizer Flow

Contours of mean volume fraction of the baseline PSA for GRID3 are given in Figure 5.1.

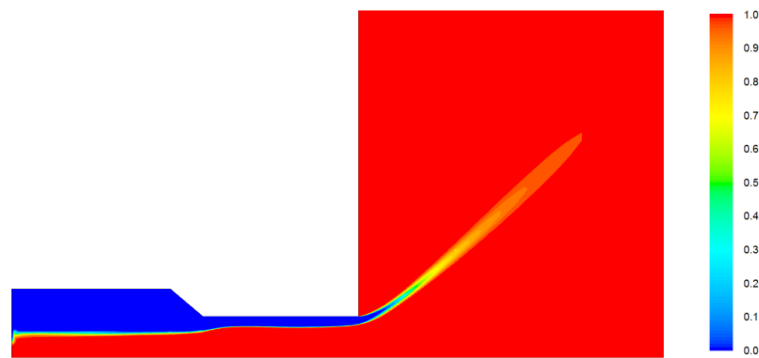


Figure 5.1. Contours of Mean Volume Fraction for Air [m/s]

The water takes part near the walls of the atomizer body, while the air is at the center of the atomizer as air core. The mean volume fractions of air at different measurement lines are given in Figure 5.2. The mean volume fraction is defined as one in the air region, zero in the water region, and between zero and one in the transition region.

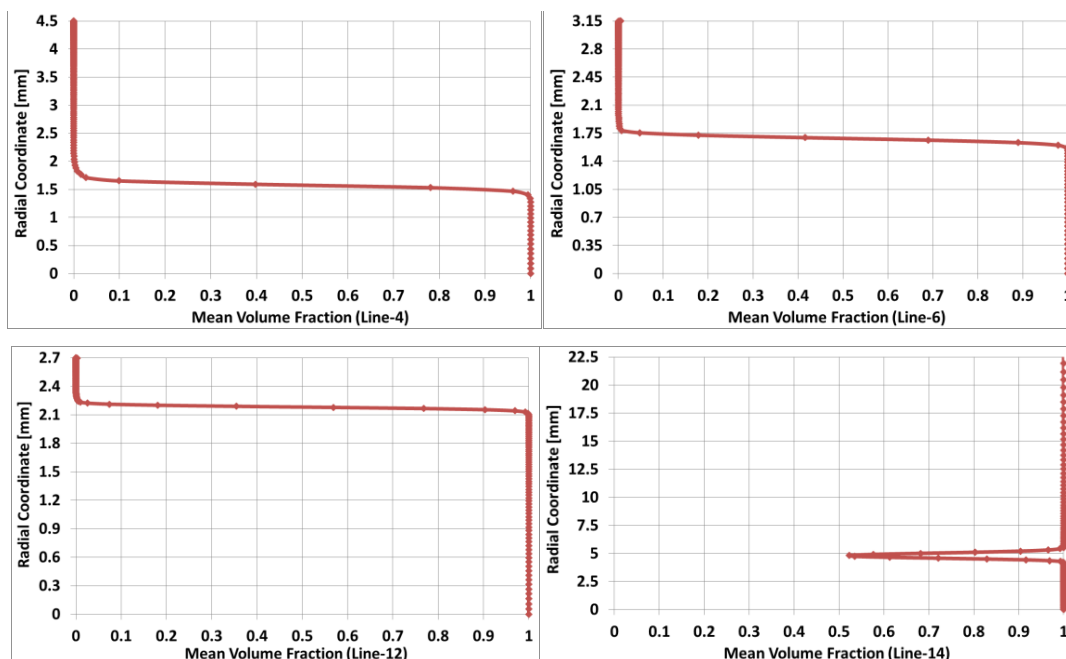


Figure 5.2. Mean Volume Fractions at Measurement Lines

Contours of mean axial velocity of the baseline PSA are given in Figure 5.3.

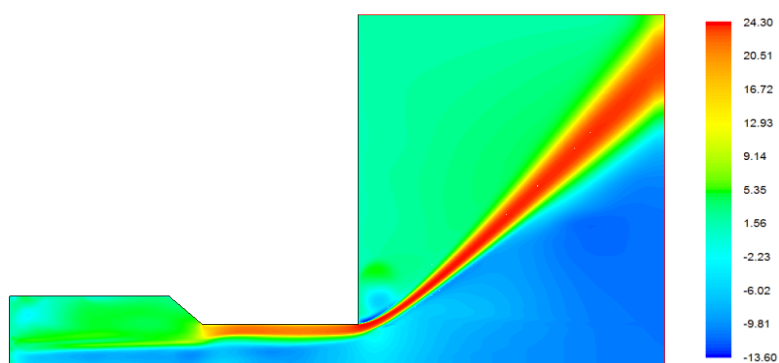


Figure 5.3 Contours of Mean Axial Velocity [m/s]

As seen from the contours of mean axial velocity, the mean axial velocity is slow in the swirl chamber and increasing through the atomizer and reaches its maximum value at the exit of the nozzle. In the air region, negative mean axial velocities are obtained which depicts the air flow into the atomizer. The magnitude of negative mean axial velocity is small at the nozzle exit and increases towards the beginning of the swirl chamber. The mean axial velocities of atomizer at four different measurement lines are shown in Figure 5.4. The horizontal red lines show the boundaries of transition region. For the Line-4, Line-6, and Line-12, upside of the transition region is water region and down side of the transition region is air region. For Line-14, transition region is on the spray, and upside and down side of the transition region is air region.

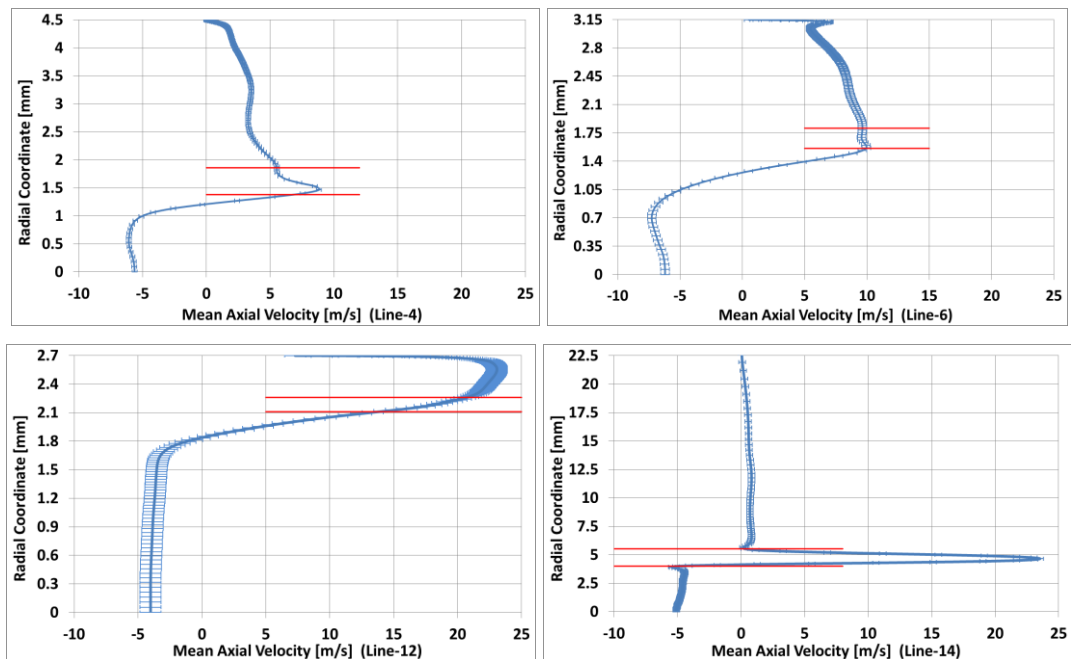


Figure 5.4. Mean Axial Velocities at Measurement Lines

The mean swirl velocity contours of the baseline PSA are given in Figure 5.5.

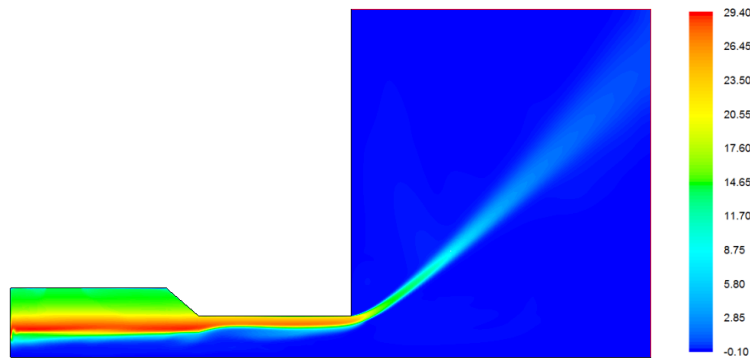


Figure 5.5. Contours of Mean Swirl Velocity [m/s]

As seen from the contours of mean swirl velocity, minimum mean swirl velocity is obtained near the atomizer walls, it gradually increases towards the transition region and reaches its maximum near the water-air interface and at the axis of the atomizer it decreases to zero. The mean swirl velocities of atomizer at four different measurement lines are shown in Figure 5.6. The horizontal red lines show the boundaries of transition region.

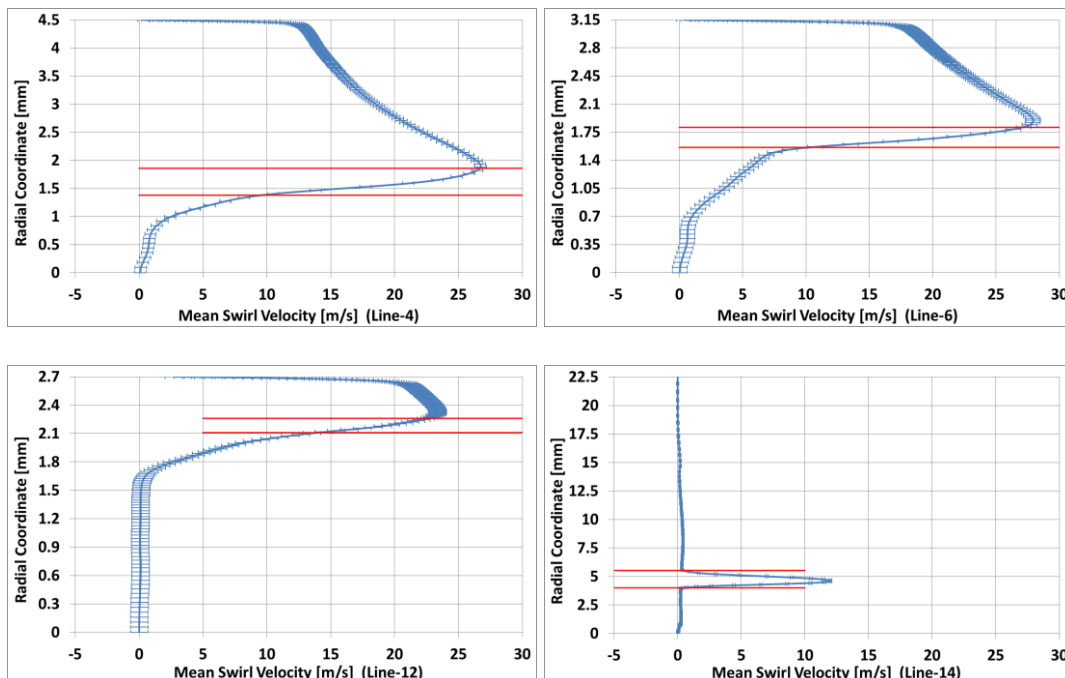


Figure 5.6. Mean Swirl Velocities at Measurement Lines

5.2.2. Mass Flow Rate Effect on the Pressure Swirl Atomizer Flow

To research the mass flow rate effect on the PSA flow, numerical analysis is repeated for Q_1 and Q_3 . The simulation results for Q_1 , Q_2 , and Q_3 are compared and results are given in Sections 5.2.2.1, 5.2.2.2, 5.2.2.3, and 5.2.2.4.

5.2.2.1. Mass Flow Rate Effect on Mean Volume Fraction

The mean volume fractions of air at different measurement lines for different mass flow rates are illustrated in Figure 5.7. As shown in graphics, mass flow rate effect on mean volume fraction is negligible. Mean volume fraction values remain nearly the same at designated measurement lines with increasing mass flow rate.

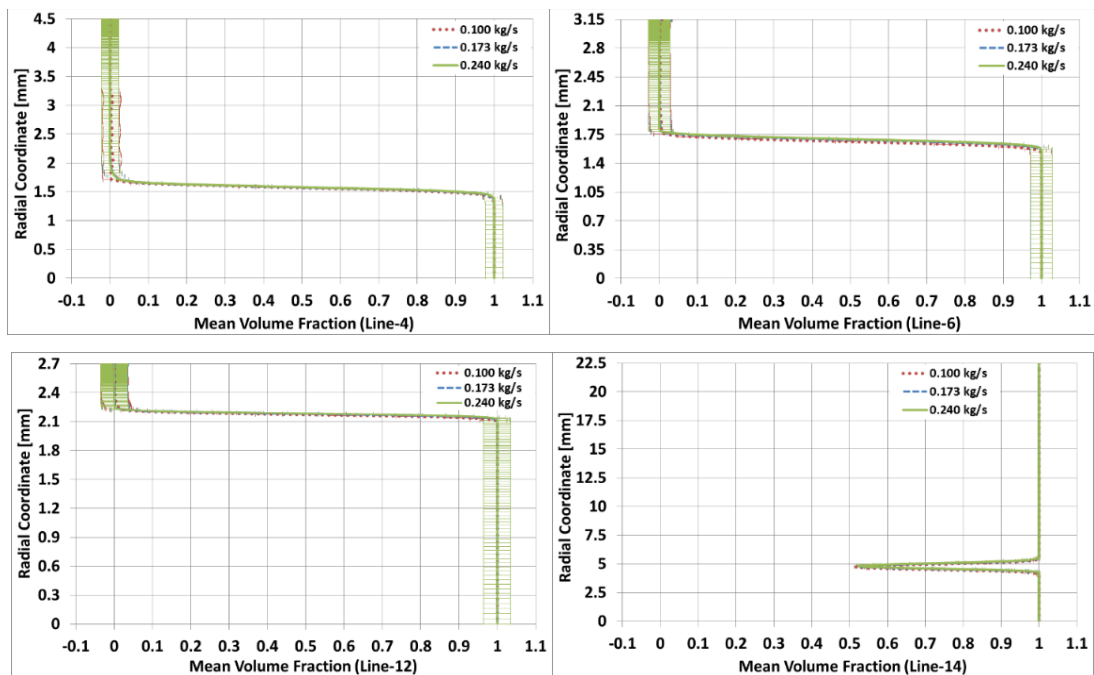


Figure 5.7. Mass Flow Rate Effect on Mean Volume Fractions at Designated Lines

5.2.2.2. Mass Flow Rate Effect on Spray Cone Angle and Air Core Diameter

The mean volume fraction of air is 1 at the atomizer axis because of the air core. The mean volume fractions of air at designated lines inside the atomizer change from 1 to 0 with increasing radial coordinate because there is the water region near the wall of the atomizer. The first change point of mean volume fraction from 1 to a lower value specifies the radial coordinate of the air core. Similarly, the mean volume fractions of air at designated lines outside the atomizer change from 1 to a lower value on the hollow cone spray. The first change point of mean volume fraction from 1 to a lower value specifies the radial coordinate of the spray edge. The air core and spray edges are defined by explained method at different measurement lines for different mass flow rates are demonstrated in Figure 5.8.

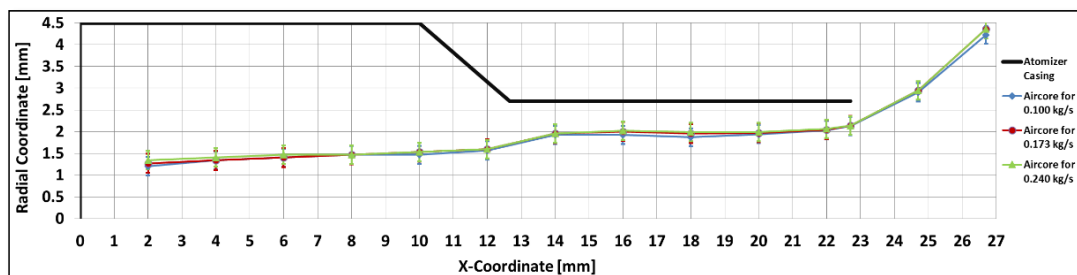


Figure 5.8. Mass Flow Rate Effect on SCA and Air Core Diameter at Designated Lines

Figure 5.8 shows that, the air core and SCA remains almost the same with increasing mass flow rate, which is in agreement with previous works [16], [29], and [49]. The minimum mean air core diameter is obtained at the beginning of the swirl chamber and stays nearly the same through the swirl chamber. At convergence section, the mean air core diameter begins to increase and at the exit of the nozzle it reaches to maximum value.

5.2.2.3. Mass Flow Rate Effect on Mean Axial Velocity

The mean axial velocities at different measurement lines for different mass flow rates are given in Figure 5.9.

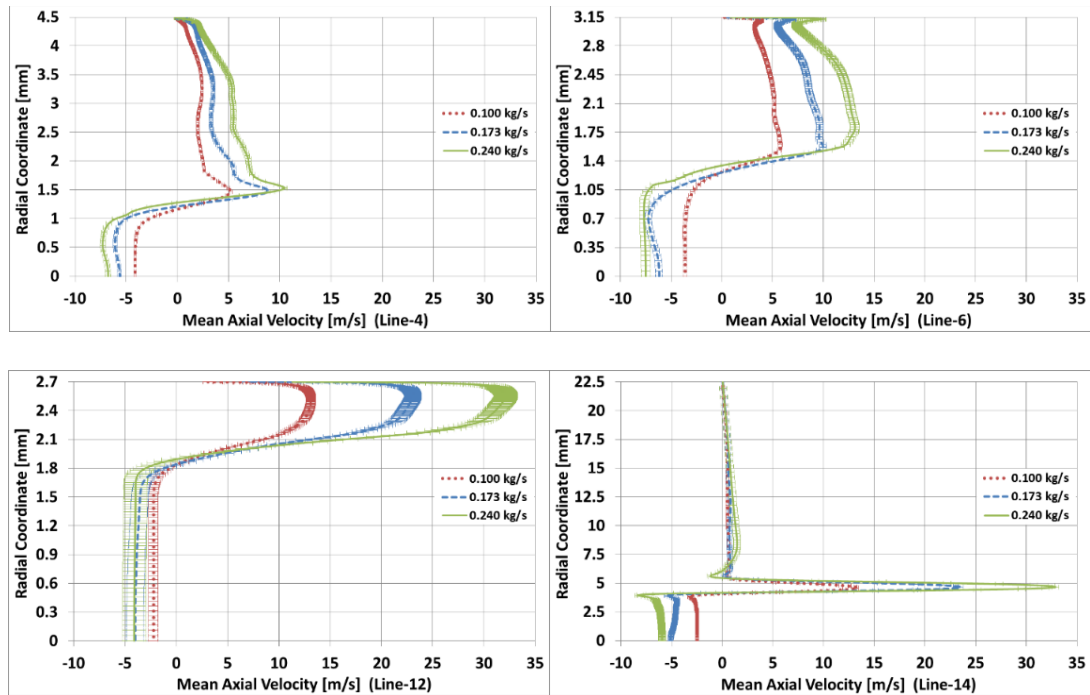


Figure 5.9 Mass Flow Rate Effect on Axial Velocities at Designated Lines

As shown in the figure, mean axial velocity in the water region and the magnitude of the negative mean axial velocity in the air region increase with increasing mass flow rate. The maximum mean axial velocities are 13.7 m/s, 24.0 m/s, and 33.5 m/s for Q_1 , Q_2 , and Q_3 , respectively. The maximum magnitude of negative mean axial velocities are 4.9 m/s, 7.3 m/s, and 8.3 m/s for Q_1 , Q_2 , and Q_3 , respectively.

5.2.2.4. Mass Flow Rate Effect on Mean Swirl Velocity

The mean swirl velocities at different measurement lines for different mass flow rates are given in Figure 5.10.

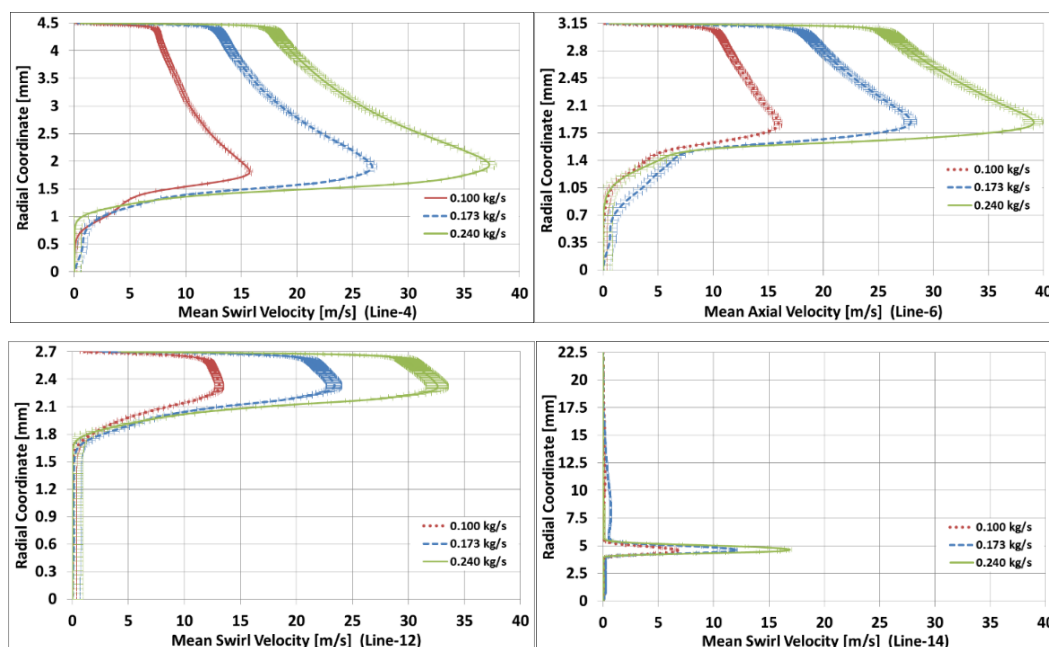


Figure 5.10. Mass Flow Rate Effect on Mean Swirl Velocities at Designated Lines

As depicted in the figure, increasing mass flow rate leads to an increase in the mean swirl velocity. The maximum values of mean swirl velocity are 16.1 m/s, 29.4 m/s, and 40.7 m/s for Q_1 , Q_2 , and Q_3 , respectively.

5.2.3. Spray Cone Angle

Calculated mean SCAs of baseline PSA for three different mass flow rates are given in Table 5.1.

Table 5.1. Mean SCA of Baseline PSA

	Mean SCA		
	Q_1	Q_2	Q_3
Baseline PSA	83.3°	84.0°	84.4°

Numerical simulations reveal that the mass flow rate has negligible effect on SCA.

CHAPTER 6

COMPARISON OF EXPERIMENTAL AND NUMERICAL RESULTS

6.1. Spray Cone Angle Comparison

Calculated SCAs of baseline PSA for experimental and numerical studies are given in Table 6.1 for three mass flow rates. Experimental SCA values in Table 6.1 have an uncertainty less than 3°.

Table 6.1. Comparison of SCAs

	Spray Cone Angle		
	Q ₁	Q ₂	Q ₃
Experimental Results	83.0°	81.1°	85.8°
Numerical Results	83.3°	84.0°	84.4°
Deviation	0.36 %	3.58 %	1.63 %

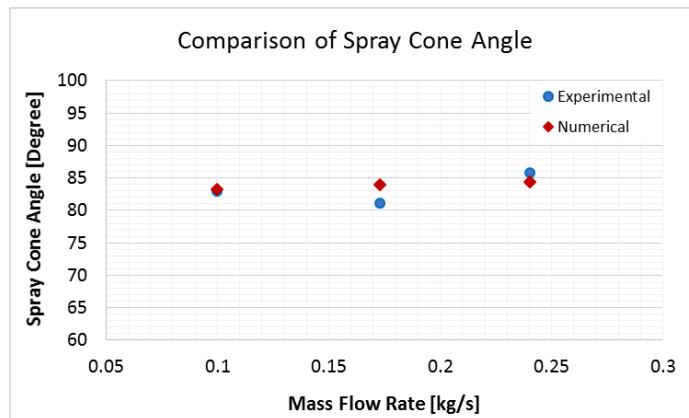


Figure 6.1. Comparison of Spray Cone Angle Graphically

The results show that SCAs for experimental and numerical studies are compatible and maximum difference is less than 4%.

6.2. Axial and Radial Velocity Comparison

Axial and radial velocities of baseline PSA are measured experimentally and numerically. Measured axial and radial velocities along a vertical line at location $x=20$ mm are compared for three mass flow rates and results are denoted in Figure 6.2 and Figure 6.3.

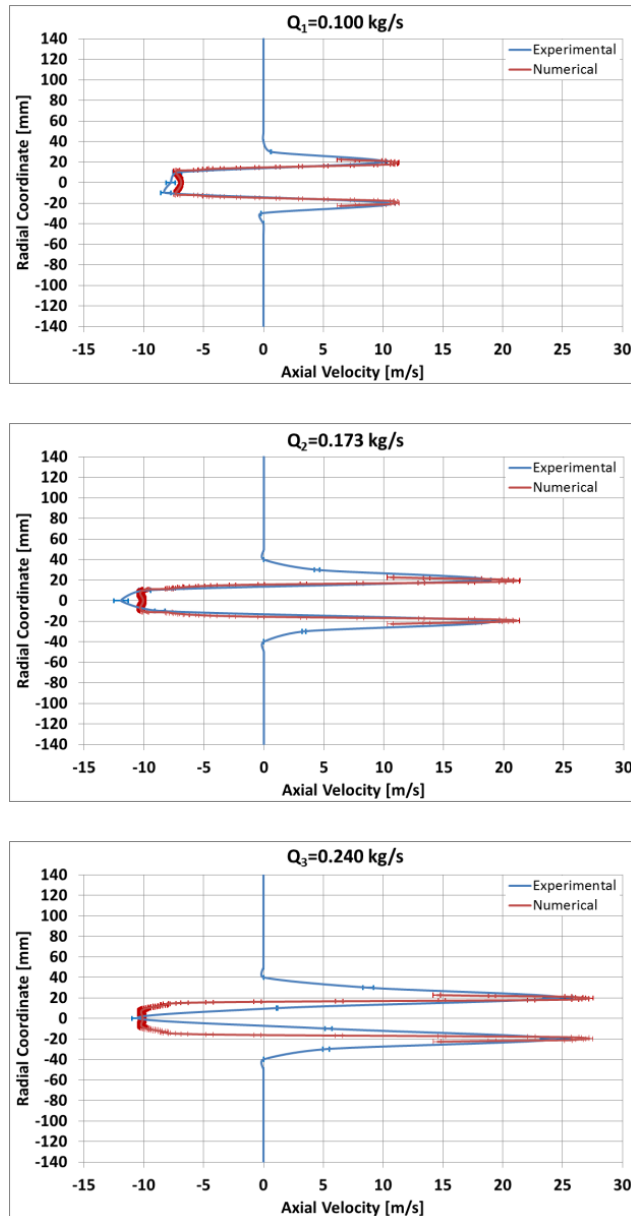


Figure 6.2. Comparison of Axial Velocities at $x=20$ mm for Three Mass Flow Rates

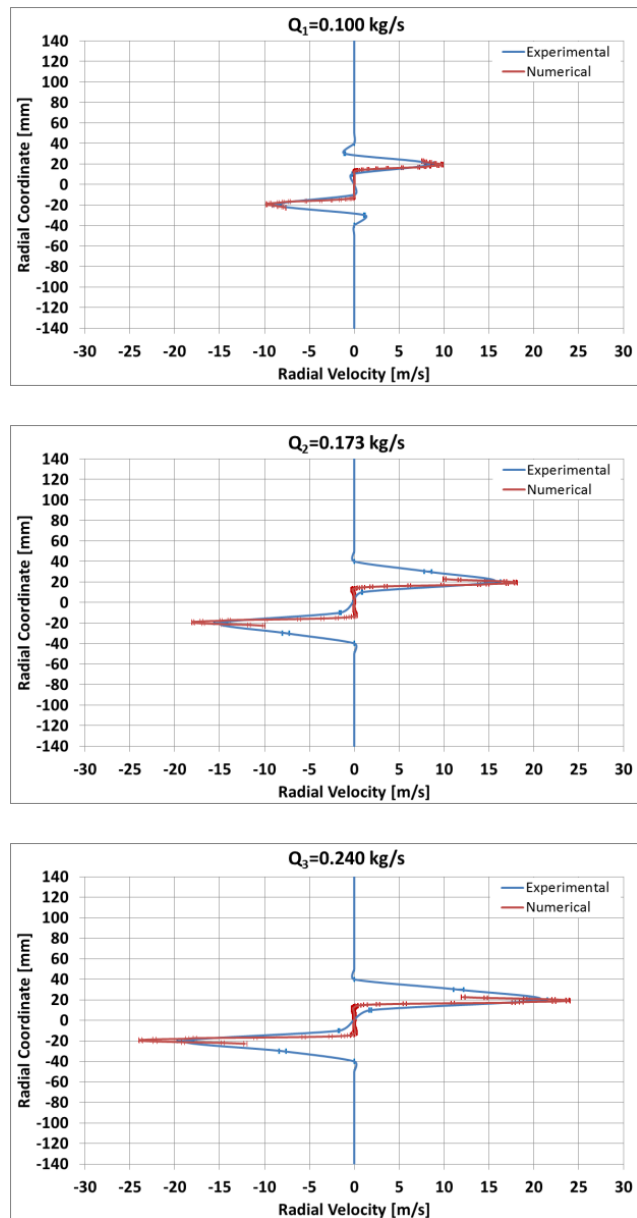


Figure 6.3. Comparison of Radial Velocities at $x=20$ mm for Three Mass Flow Rates

The comparisons show that numerical results are in good qualitative agreement with experimental results and velocity measurements are accurate to within 10%.

CHAPTER 7

CONCLUSIONS

In this thesis, effects of geometrical parameters of PSA on the hollow cone spray are investigated experimentally, and physical phenomenon inside the PSA is examined using numerical methods.

Within the scope of the experimental study, macroscopic properties of spray are visualized by HSSS. Obtained images via this system are imported in the image processing program and length between the spray edges is measured at two different locations. These distance values are used to calculate the SCA. SCA is calculated for seven test atomizers at three different mass flow rates. Additionally, microscopic properties of spray are investigated with PDPA system for seven test atomizers at three different mass flow rates.

Investigation of the macroscopic properties show that SCA changes slightly with variation of mass flow rate, nozzle length, and tangential port number. Otherwise, increasing nozzle diameter causes an increase in SCA. In addition to these results, the calculated SCA value for baseline atomizer is found to be consistent with the value specified in the literature. The breakup length shortens with increasing mass flow rate and decreasing nozzle diameter, but change of breakup length with nozzle length and tangential port number is negligible.

Investigation of the microscopic properties with PDPA system gives information about the velocity and size distribution of particles. Effects of geometrical parameters and mass flow rate on the axial and radial velocity distributions are investigated. The results show that magnitude of velocities of the spray increases and revealed vortex at the exit of the atomizer becomes smaller with increasing mass flow rate and decreasing nozzle diameter. Nozzle length and tangential port number have no significant effect

on the magnitude of velocities and vortex within the specified ranges of values. The SMD distributions show that big droplets exist on the spray cone and smaller ones appear near the axis of the hollow cone spray. As seen from the SMD distributions, the SMD values changes slightly with mass flow rate and nozzle length. In addition, the results show that nozzle diameter and tangential port number affect the SMD distributions. Decreasing nozzle diameter has a reducing effect on the SMD of particles near the spray boundaries. Increasing tangential port number causes an improvement on the uniformity of particle distribution. The results show that SMD distributions for the atomizers with two and four tangential ports are irregular, but small droplets are located in the center of the spray, and droplet diameter tends to increase with y coordinate and reaches the maximum value on the liquid jet for the atomizer with six tangential ports. This result shows that, unlike most studies in the literature, the tangential port number has a significant effect on droplet distribution.

The experimental results obtained in this thesis, such as SCA, breakup length, velocity and SMD distributions for PSAs, are important inputs for combustion modelling. There are not so many results in the literature about the velocity and SMD distribution fields of PSAs, but this thesis contains a lot of important experimental data and inputs for combustion modelling.

To investigate the flow phenomenon inside the PSA, two-dimensional axisymmetric and unsteady numerical simulations are performed for the baseline PSA using ANSYS-FLUENT software. Volume fraction, axial velocity, and radial velocity distributions inside the atomizer are obtained and effect of mass flow rate on the volume fraction, SCA, air core diameter, axial velocity, and swirl velocity is investigated. Simulations results show that SCA and air core diameter change barely with mass flow rate. Magnitude of the axial velocity in the water and air region tends to increase with increasing mass flow rate. Additionally, swirl velocity also increases with increasing mass flow rate. This thesis also shows that numerical results are in good qualitative agreement with experimental results. Therefore, numerical model can be used in order to obtain SCA and velocity distributions of PSA.

In a future study, effects of the rest of the geometrical parameters such as swirl chamber diameter, swirl chamber length, and tangential port diameter on the hollow cone spray may be investigated. Additionally, the tests performed in this thesis may be repeated with other test fluids (especially LOX) in order to investigate the effect of test fluid on the macroscopic and microscopic properties of PSA.

REFERENCES

- [1] D. H. Huang and D. K. Huzel, *Modern Engineering for Design of Liquid-Propellant Rocket Engines*. 1992.
- [2] H. C. T. Raposo, “Mixture Ratio and Thrust Control of a Liquid-Propellant Rocket Engine,” *Tecnico Lisboa*, 2016.
- [3] G. S. Gill and W. H. Nurick, “Liquid rocket engine injectors,” in *NASA Space Vehicle Design Criteria (Chemical Propulsion)*, 1976.
- [4] A. Lefebvre and V. McDonell, *Atomization and Sprays, Second Edition*. 2017.
- [5] Y. I. Khavkin, *Theory and Practice of Swirl Atomizers*. Taylor & Francis, 2004.
- [6] A. H. Lefebvre, D. R. Ballal, and D. W. Bahr, “GAS TURBINE COMBUSTION—Alternative Fuels and Emissions,” *J. Eng. Gas Turbines Power*, 2010.
- [7] L. Durdina, J. Jedelsky, and M. Jicha, “Experimental Investigation on Spray Characteristics of Pressure-Swirl Atomizers for a Small-Sized Jet Engine,” *ICLASS 2012, 12th Trienn. Int. Conf. Liq. At. Spray Syst. Heidelberg, Ger.*, 2012.
- [8] Q. Fu, L. Yang, and X. Wang, “Theoretical and Experimental Study of the Dynamics of a Liquid Swirl Injector,” *J. Propuls. Power*, vol. 26, no. 1, 2010.
- [9] V. R. Rubinsky, “Combustion Instability in the RD-0110 Engine,” in *Liquid Rocket Engine Combustion Instability*, V. Yang and W. E. Anderson, Eds. American Institute of Aeronautics and Astronautics, Inc., 1995, pp. 89–112.
- [10] M. Rashad, H. Yong, and Z. Zekun, “Effect of geometric parameters on spray characteristics of pressure swirl atomizers,” *Int. J. Hydrogen Energy*, vol. 41, no. 35, pp. 15790–15799, 2016.

- [11] J. Liu, X. Q. Zhang, Q. L. Li, and Z. G. Wang, "Effect of geometric parameters on the spray cone angle in the pressure swirl injector," *Proc. Inst. Mech. Eng. Part G J. Aerosp. Eng.*, 2013.
- [12] A. T. Sakman, M. A. Jog, S. M. Jeng, and M. A. Benjamin, "Parametric study of simplex fuel nozzle internal flow and performance," *AIAA J.*, 2012.
- [13] E. Steinthorsson, M. A. Benjamin, and P. H. Corporation, "Influence of Geometry on the Performance of Simplex Nozzles under Constant Pressure Drop J . Xue , M . A . Jog *, and S . M . Jeng University of Cincinnati , Cincinnati , OH 45221 and," *ILASS Am.*, vol. 15, no. May, 2002.
- [14] S. K. Chen, A. H. Lefebvre, and J. Rollbuhler, "Factors Influencing the Effective Spray Cone Angle of Pressure-Swirl Atomizers," *J. Eng. Gas Turbines Power*, vol. 114, no. 1, p. 97, 2008.
- [15] S. K. Som and S. G. Mukherjee, "Theoretical and experimental investigations on the coefficient of discharge and spray cone angle of a swirl spray atomizing nozzle," *Acta Mech.*, 1980.
- [16] A. Datta and S. K. Som, "Numerical prediction of air core diameter, coefficient of discharge and spray cone angle of a swirl spray pressure nozzle," *Int. J. Heat Fluid Flow*, vol. 21, no. 4, pp. 412–419, 2000.
- [17] M. S. F. M. Rashid, A. H. A. Hamid, O. C. Sheng, and Z. A. Ghaffar, "Effect of inlet slot number on the spray cone angle and discharge coefficient of swirl atomizer," *Procedia Eng.*, vol. 41, no. Iris, pp. 1781–1786, 2012.
- [18] C. Paper and M. Lowell, "Designing an Optimized Pressure-Swirl Atomizer by Using VOF Method," 2016, no. November, pp. 2–4.
- [19] L. Yu-jing, Y. Yan-xiang, X. Da-guang, D. Qing, and Z. Ping, "Experimental Study on the Macro- and Micro-Characteristics of the Spray from a Pressure Swirl Nozzle," *Trans. Tianjin Univ.*, vol. 7, no. 2, 2001.

- [20] S. K. Chen, A. H. Lefebvre, and J. Rollbuhler, "Influence of Geometric Features on the Performance of Pressure-Swirl Atomizers," *J. Eng. Gas Turbines Power*, vol. 112, no. 4, p. 579, 2008.
- [21] X. Wei and H. Yong, "Improved Semiempirical Correlation to Predict Sauter Mean Diameter for Pressure-Swirl Atomizers," *J. Propuls. Power*, 2014.
- [22] A. Radcliffe, "Fuel Injection," *High Speed Aerodyn. Jet Propuls.*, vol. XI, no. edited by Hawthome, W. R., and Olson, W. T., Princeton Univ. Press, Princeton, NJ, p. 84, 1960.
- [23] A. K. Jasuja, "Atomization of Crude and Residual Fuel Oils," *J. Eng. Power*, 2010.
- [24] J. M. Ballester and C. Dopazo, "Drop size measurements in heavy oil sprays from pressure-swirl nozzles," *At. Sprays*, 1996.
- [25] A. H. LEFEBVRE and X. F. WANG, "Mean drop sizes from pressure-swirl nozzles," *J. Propuls. Power*, 2008.
- [26] H. S. Couto, J. A. Carvalho, and D. Bastos-Netto, "Theoretical Formulation for Sauter Mean Diameter of Pressure-Swirl Atomizers," *J. Propuls. Power*, 2008.
- [27] Y. Chung, T. Khil, J. Yoon, Y. Yoon, and V. Bazarov, "Experimental study on simplex swirl injector dynamics with varying geometry," *Int. J. Aeronaut. Sp. Sci.*, 2011.
- [28] C. C. Chu, S. F. Chou, H. I. Lin, and Y. H. Liann, "An experimental investigation of swirl atomizer sprays," *Heat Mass Transf. und Stoffuebertragung*, 2008.
- [29] B. Sümer, "Experimental and Numerical Investigation of Pressure Swirl Atomizers", PhD Thesis, METU, Ankara, 2014.
- [30] FLOW-3D, *FLOW-3D® Version 12.0 Users Manual*. 2018.

- [31] TSI-Inc., *LDV/PDPA System: Instruction Manual*, PN 1990013. 2005.
- [32] J. Shakal, "Phase Doppler Particle Analyzer," *TSI LDV/PDPA Work. Train.*, 2007.
- [33] TSI-Inc., *MDG-100 Monosize Droplet Generator Operation and Service Manual*, P/N 199087. 2010.
- [34] L. P. Bayvel and Z. Orzechowski, *Liquid atomization*. 1993.
- [35] P.-K. Wu, G. A. Ruff, and G. M. Faeth, "PRIMARY BREAKUP IN LIQUID-GAS MIXING LAYERS," *At. Sprays*, 2014.
- [36] P.-G. Han, J.-H. Seol, S.-H. Hwang, and Y. Yoon, "The Spray Characteristics of Swirl Coaxial Injectors," 2013.
- [37] M. J. Ketabdari, "Free Surface Flow Simulation Using VOF Method," in *Numerical Simulation - From Brain Imaging to Turbulent Flows*, 2016.
- [38] M. R. Morad and E. Eslami, "Numerical and experimental study on aircore formation in a liquid-liquid coaxial swirl injector," in *10th International Conference on Liquid Atomization and Spray Systems*, 2006.
- [39] A. Nouri-Borujerdi and A. Kebriaee, "Numerical Simulation of Laminar and Turbulent Two-Phase Flow in Pressure-Swirl Atomizers," *AIAA J.*, 2012.
- [40] J. Madsen, B. H. Hjertager, and T. Solberg, "Numerical Simulation of Internal Flow in a Large-Scale Pressure-Swirl Atomizer," *ILASS-Europe*, 2004.
- [41] Inc. ANSYS, "ANSYS FLUENT Theory Guide," *Release 18.2*, 2013.
- [42] M. R. Modarres-Razavi, M. R. Moghaddam, and R. Elahi, "Designing an Optimized Pressure-Swirl Atomizer by Using VOF Method," *Iran. Aerosp. Soc. Conf.*, 2010.

- [43] J. J. Chinn, “The Internal Flow Physics of Swirl Atomizer Nozzles,” University of Manchester Institute of Science and Technology, Manchester, England, 1996.
- [44] S. Muzaferija, M. Peric, P. Sames, and T. Schellin, *A two-fluid Navier-Stokes solver to simulate water entry*. 1998.
- [45] S. K. Dash, M. R. Halder, M. Peric, and S. K. Som, “Formation of Air Core in Nozzles With Tangential Entry,” *J. Fluids Eng.*, 2002.
- [46] Q. F. Fu, “Numerical simulation of the internal flow of swirl atomizer under ambient pressure,” *Proc. Inst. Mech. Eng. Part C J. Mech. Eng. Sci.*, 2016.
- [47] E. von Lavante, U. Maatje, and F.-O. Albina, “Investigation of Unsteady Effects in Pressure Swirl Atomizers,” *ILASS-Europe*, 2002.
- [48] S. K. Som, “Air Core in Pressure Swirl Atomizing Nozzles,” *At. Sprays*, vol. 22, no. 4, pp. 283–303, 2012.
- [49] M. R. Halder, S. K. Dash, and S. K. Som, “Influences of nozzle flow and nozzle geometry on the shape and size of an air core in a hollow cone swirl nozzle,” *Proc. Inst. Mech. Eng. Part C J. Mech. Eng. Sci.*, 2003.

APPENDICES

A. Mass Flow Rate Effect on Microscopic Properties of Test Atomizers

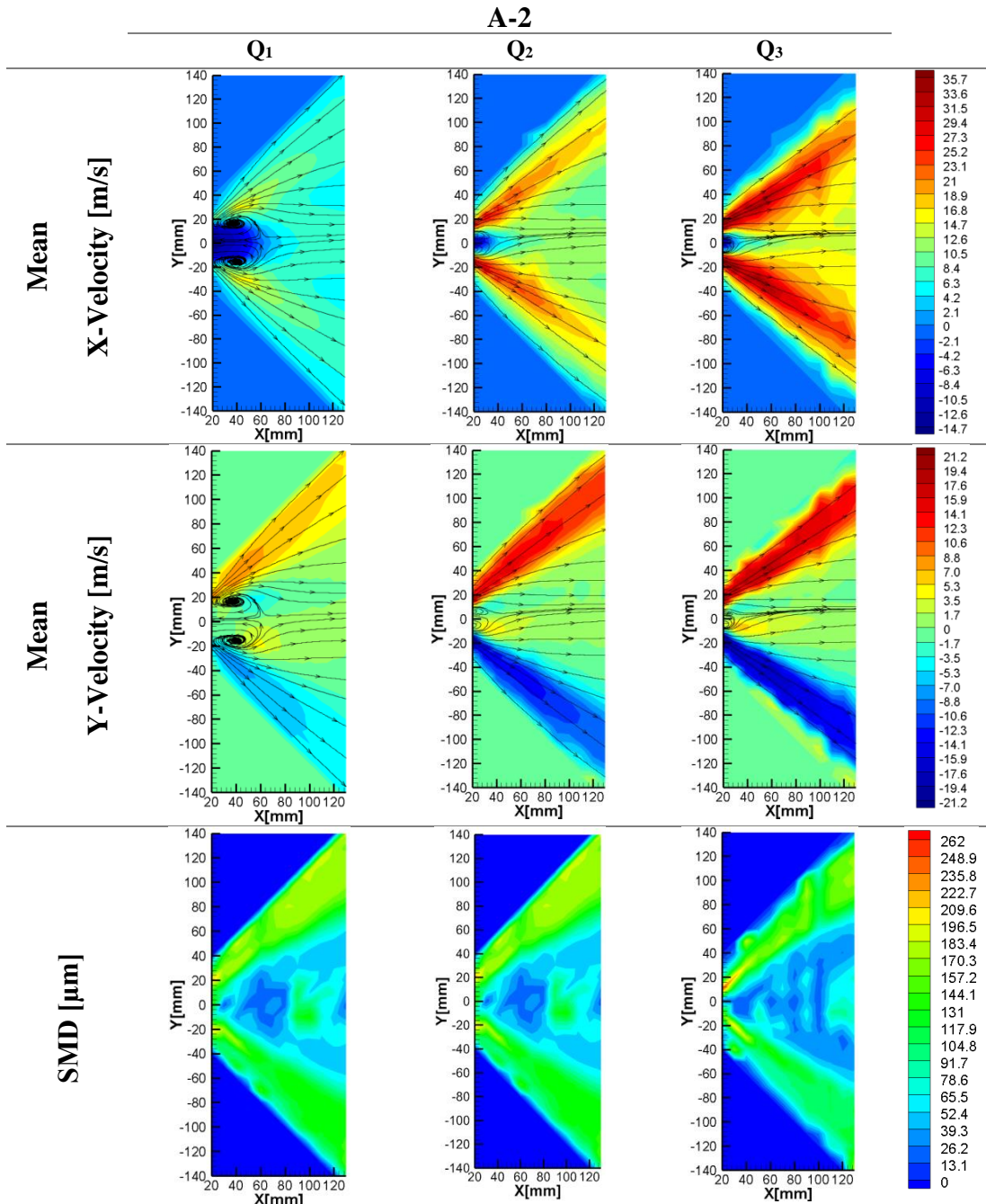


Figure A.1. Mass Flow Rate Effect on the Microscopic Properties of A-2

A-2 ($D_0=4.1$ mm)

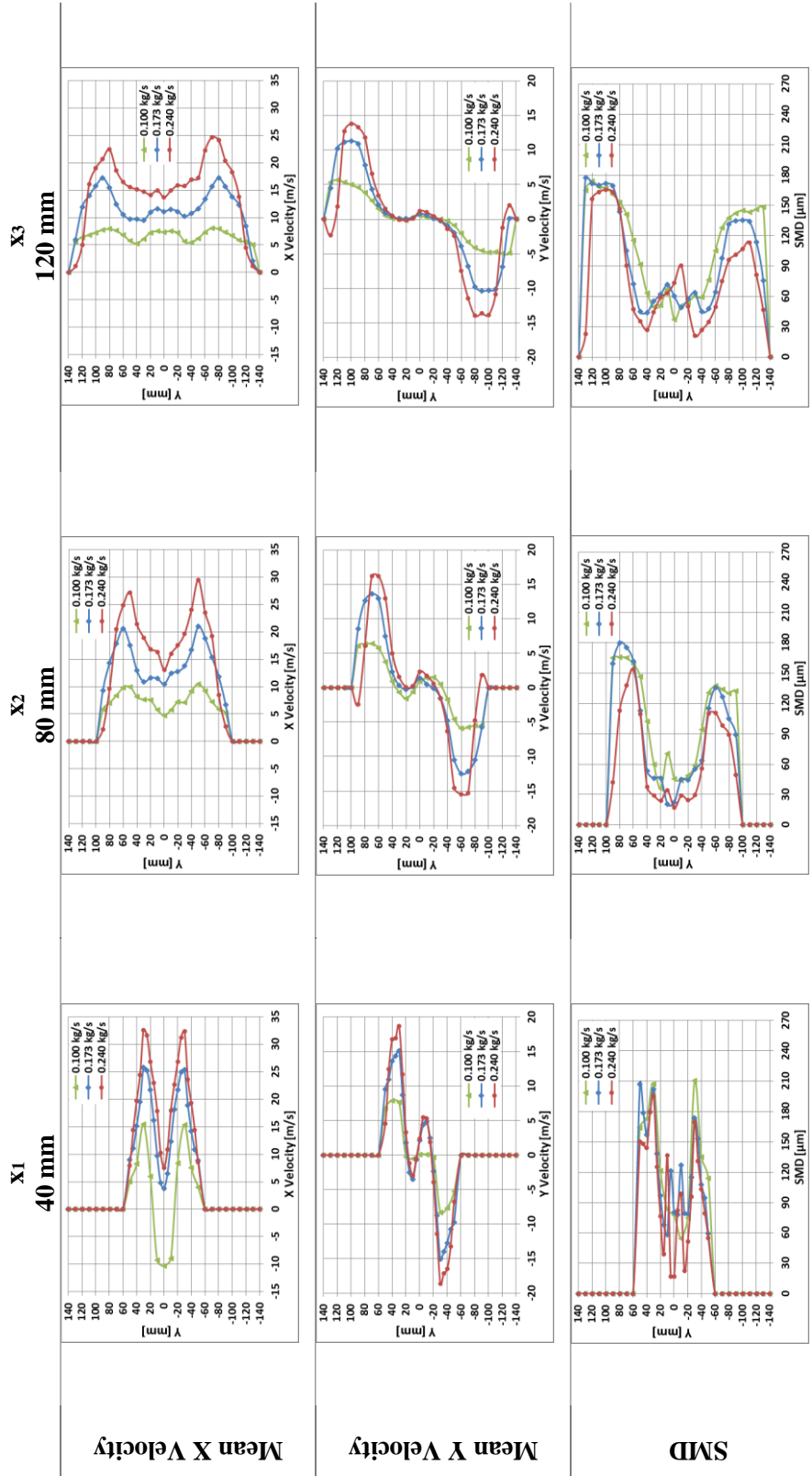


Figure A.2. Comparison of Mass Flow Rate Effect on the Microscopic Properties of A-2 at Specified x Coordinates

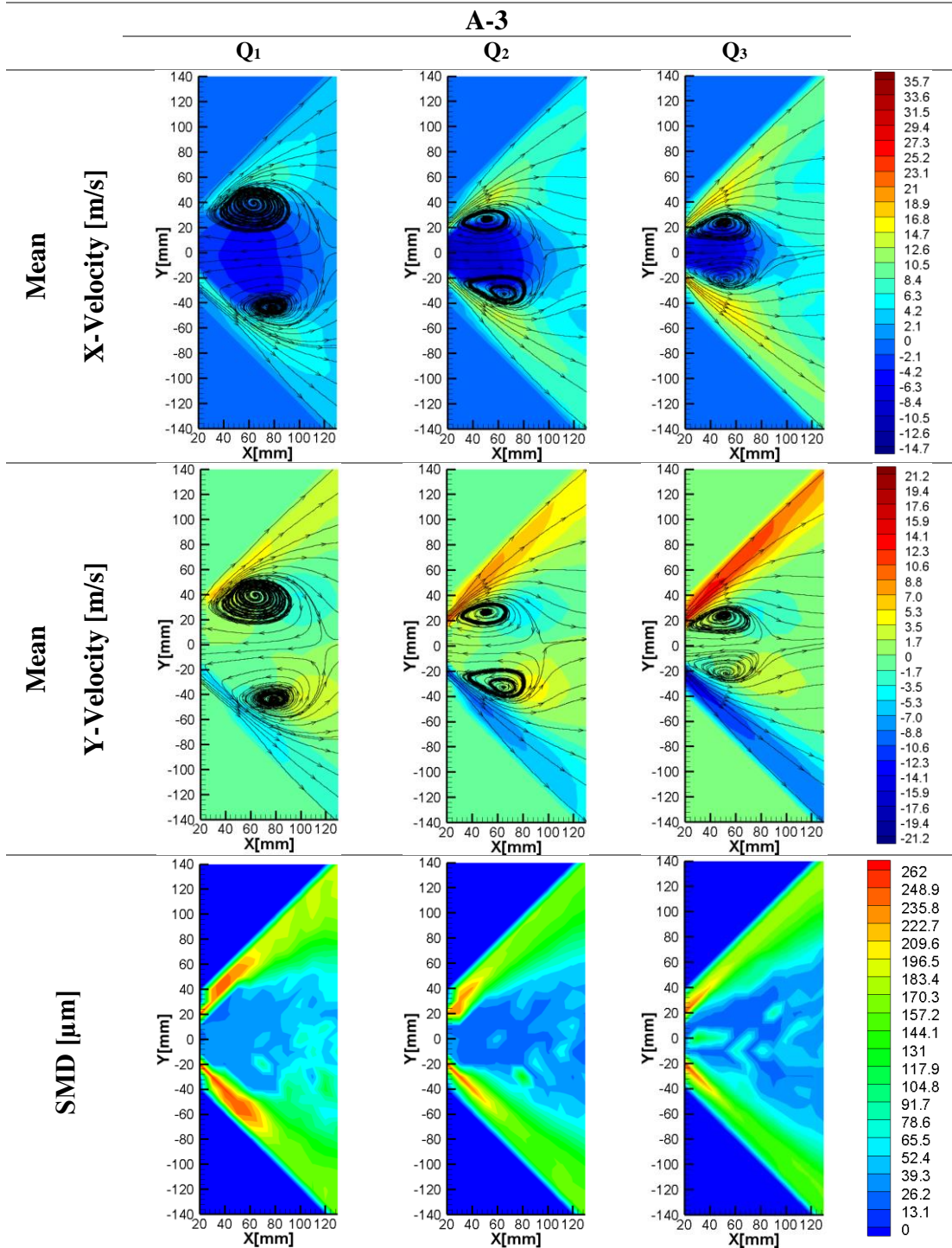


Figure A.3. Mass Flow Rate Effect on the Microscopic Properties of A-3

A-3 ($D_0=6.8$ mm)

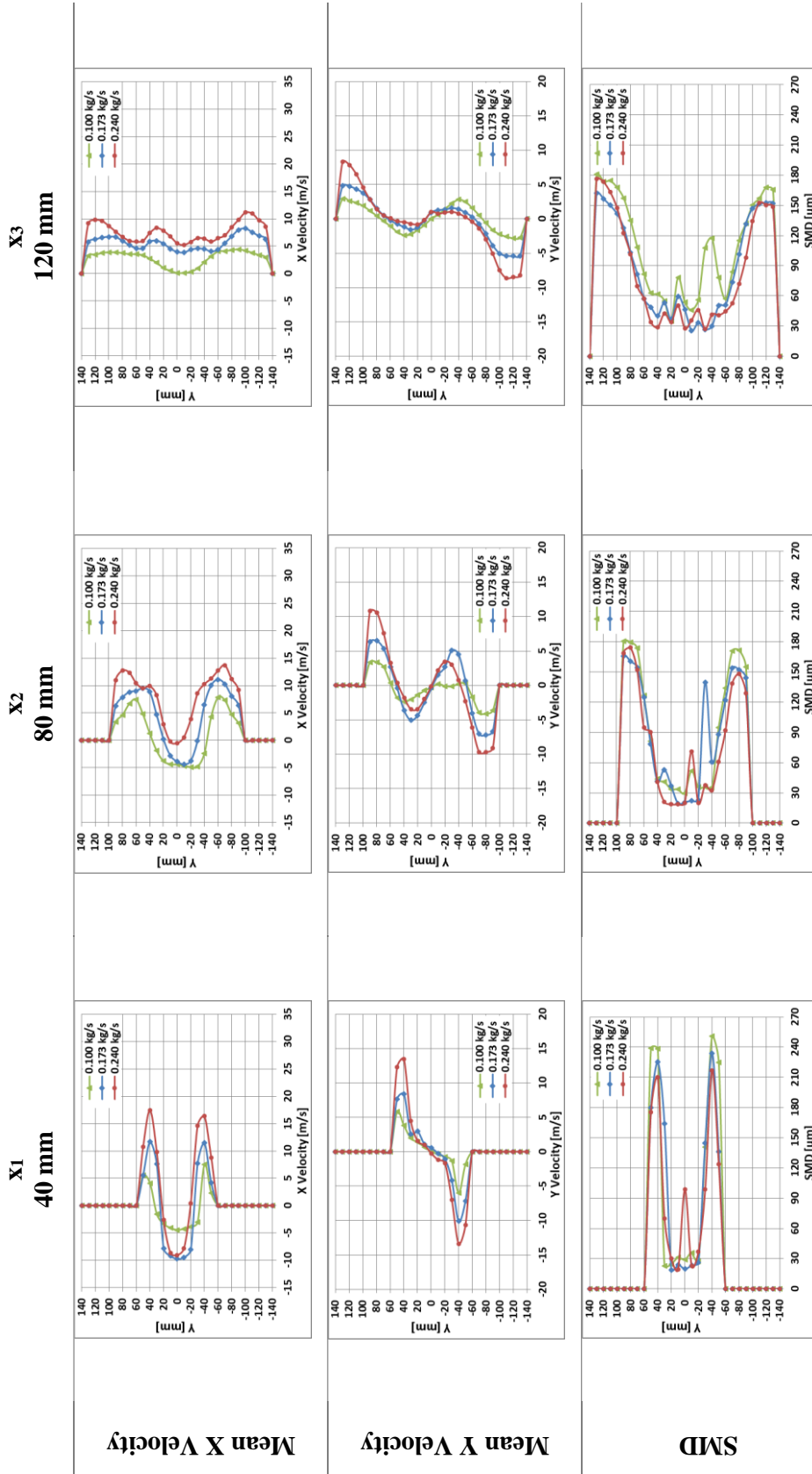


Figure A.4. Comparison of Mass Flow Rate Effect on the Microscopic Properties of A-3 at Specified x Coordinates

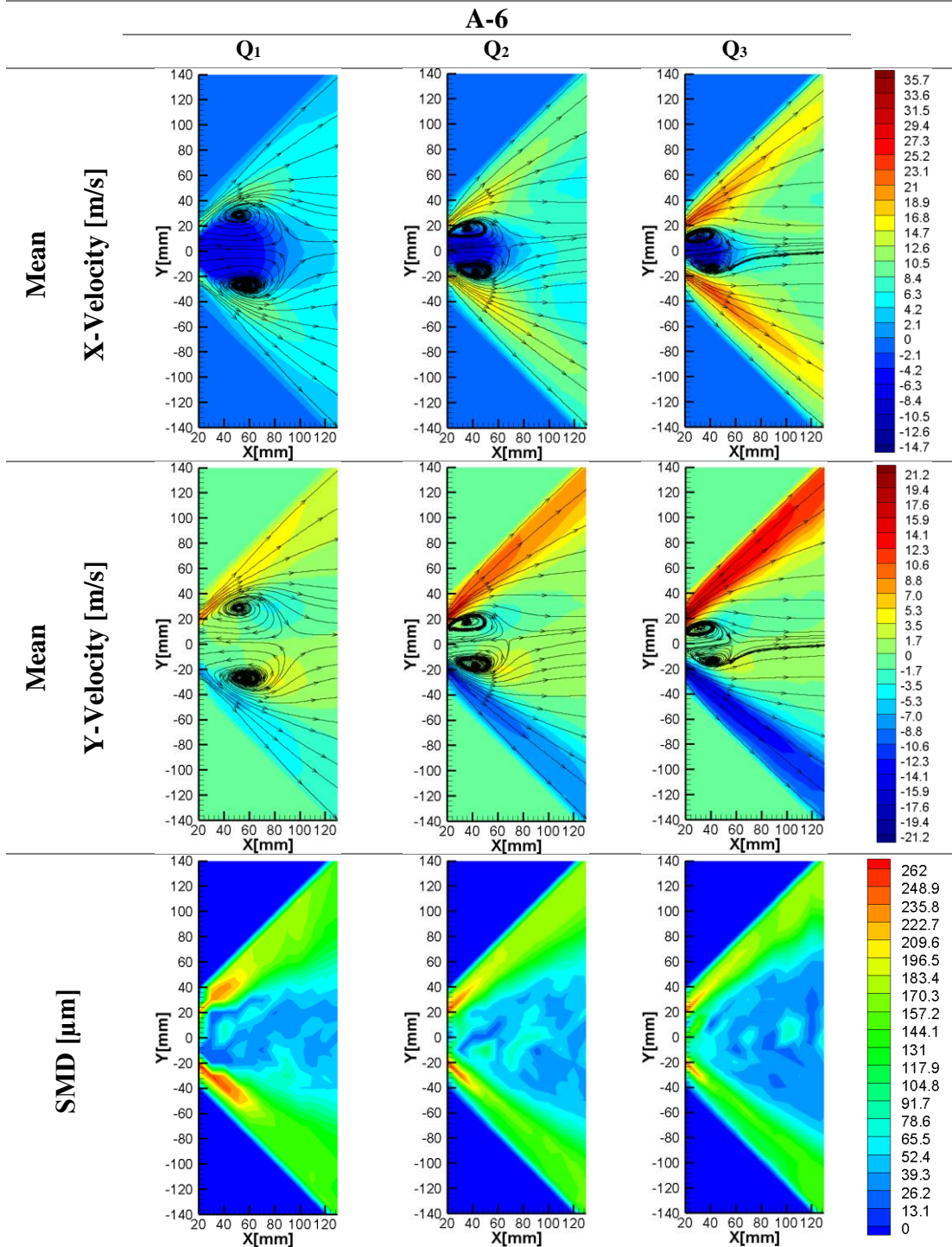


Figure A.5. Mass Flow Rate Effect on the Microscopic Properties of A-6

A-6 ($L_0=8.1$ mm)

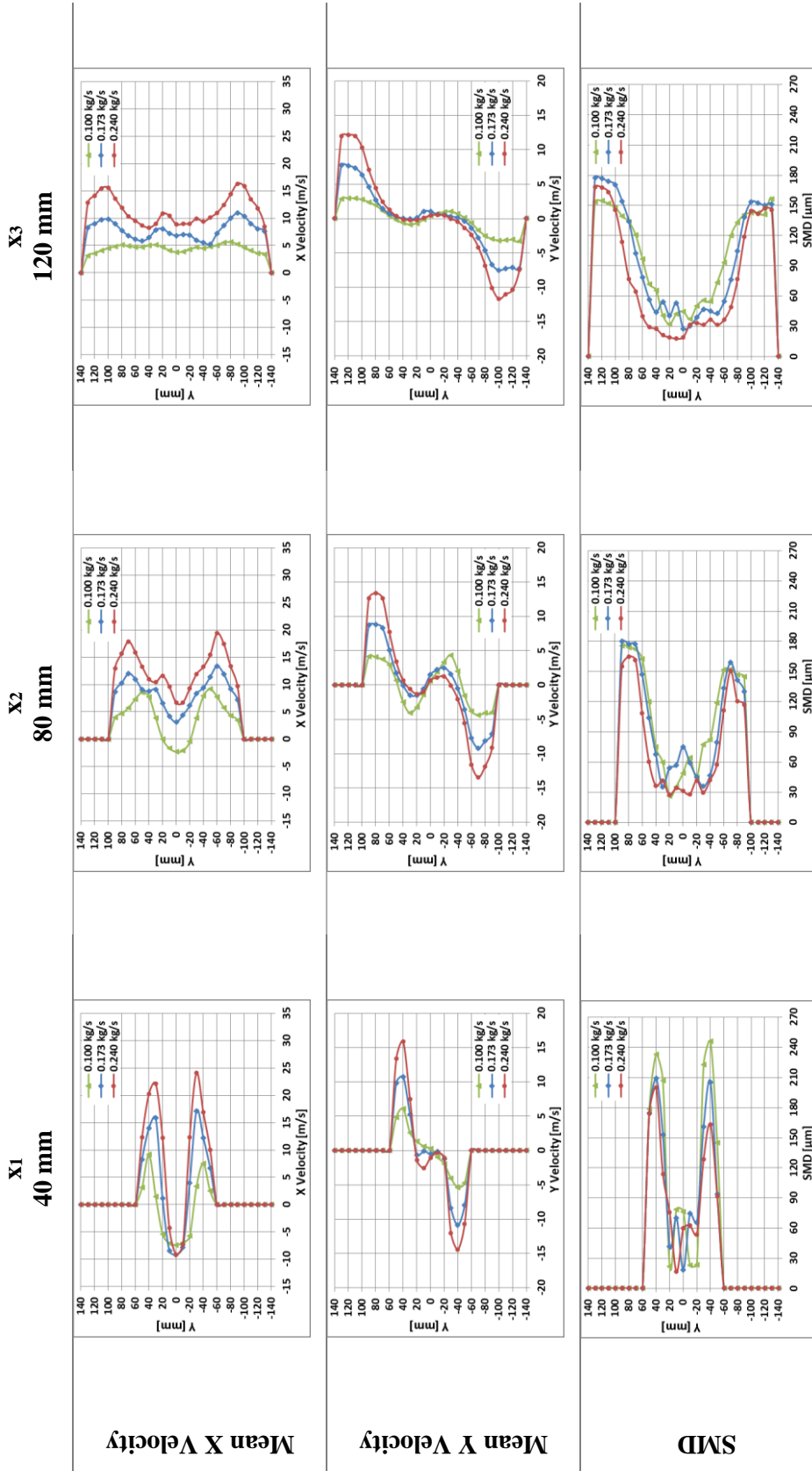


Figure A.6. Comparison of Mass Flow Rate Effect on the Microscopic Properties of A-6 at Specified x Coordinates

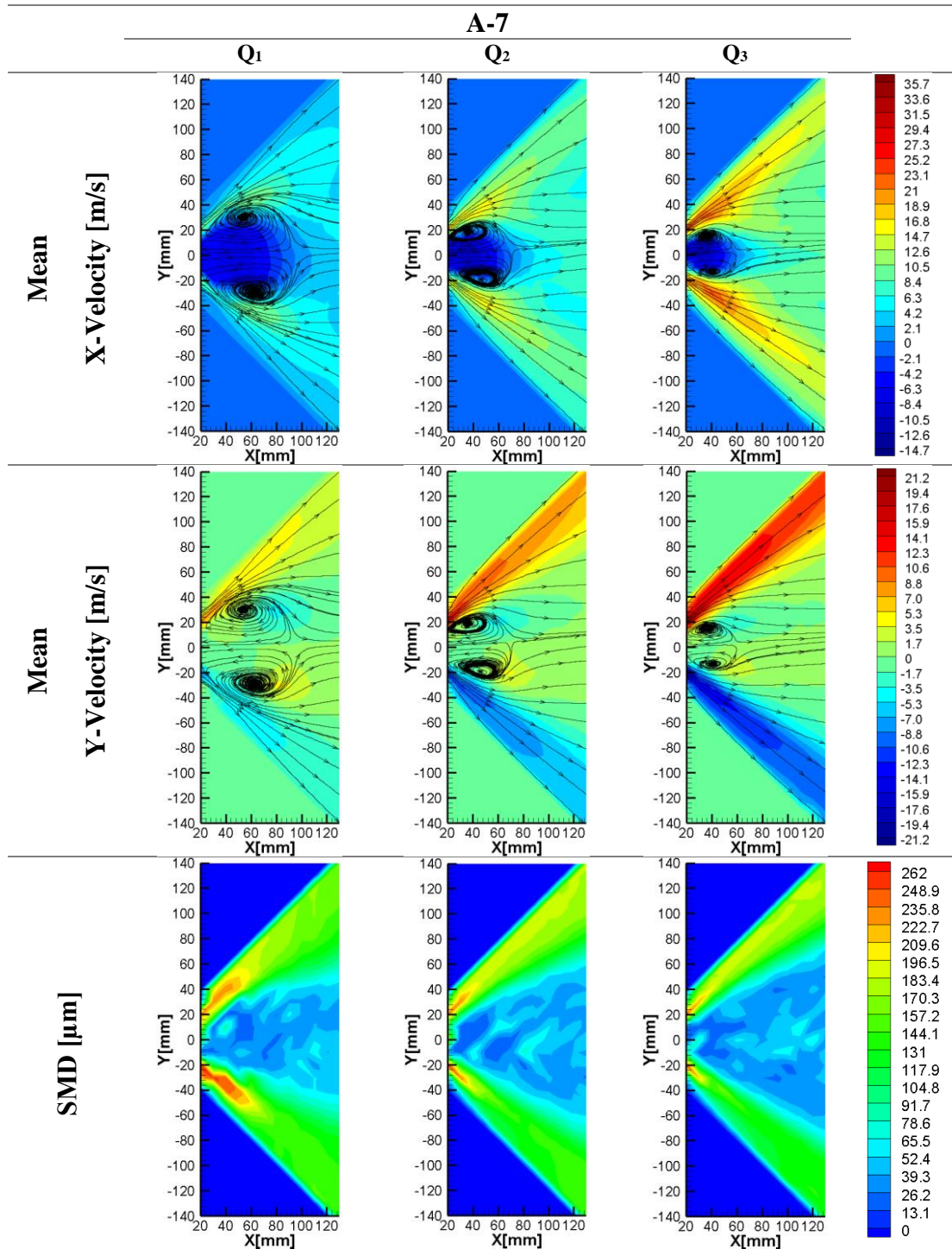


Figure A.7. Mass Flow Rate Effect on the Microscopic Properties of A-7

A-7 ($L_0=13.5$ mm)

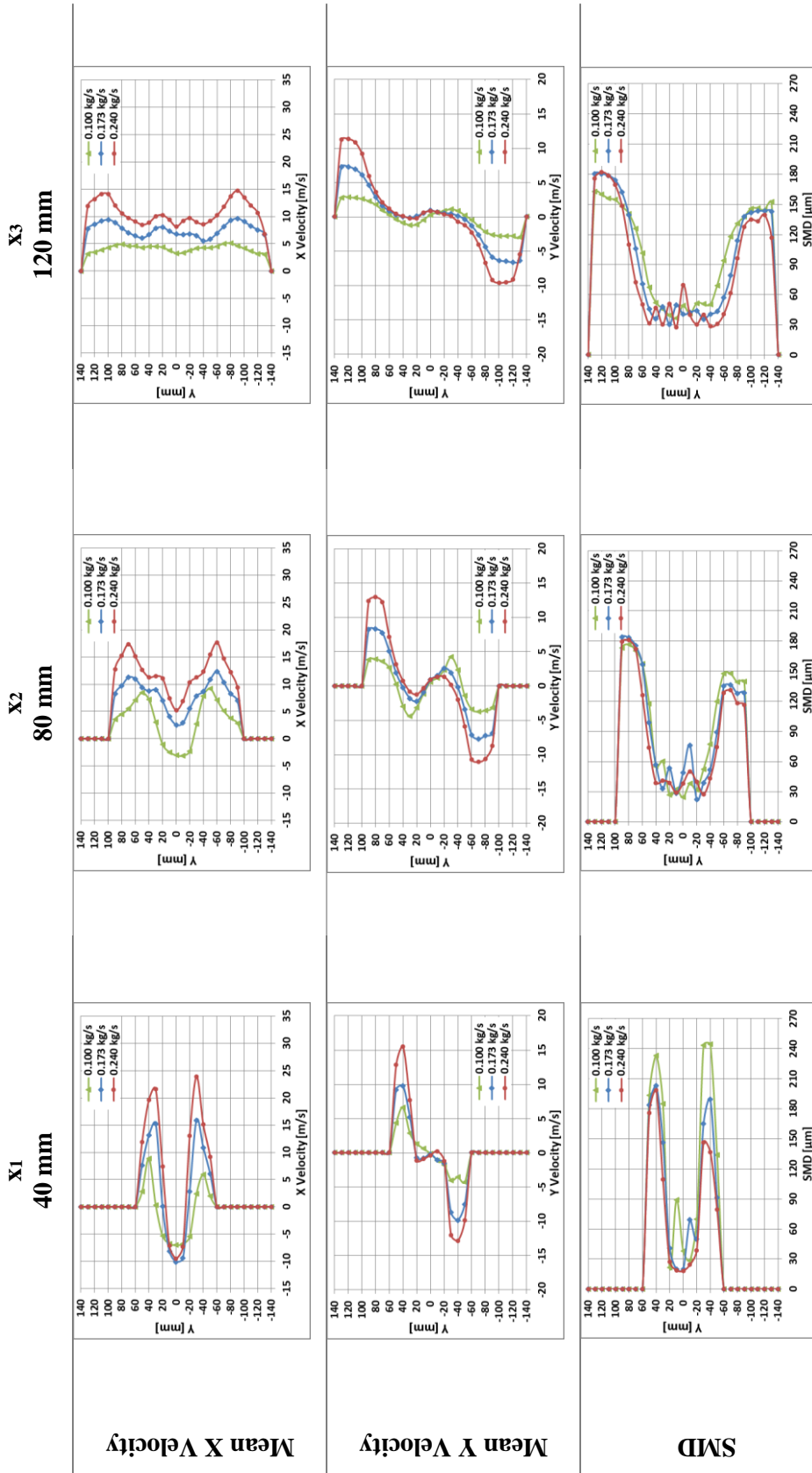


Figure A.8. Comparison of Mass Flow Rate Effect on the Microscopic Properties of A-7 at Specified x Coordinates

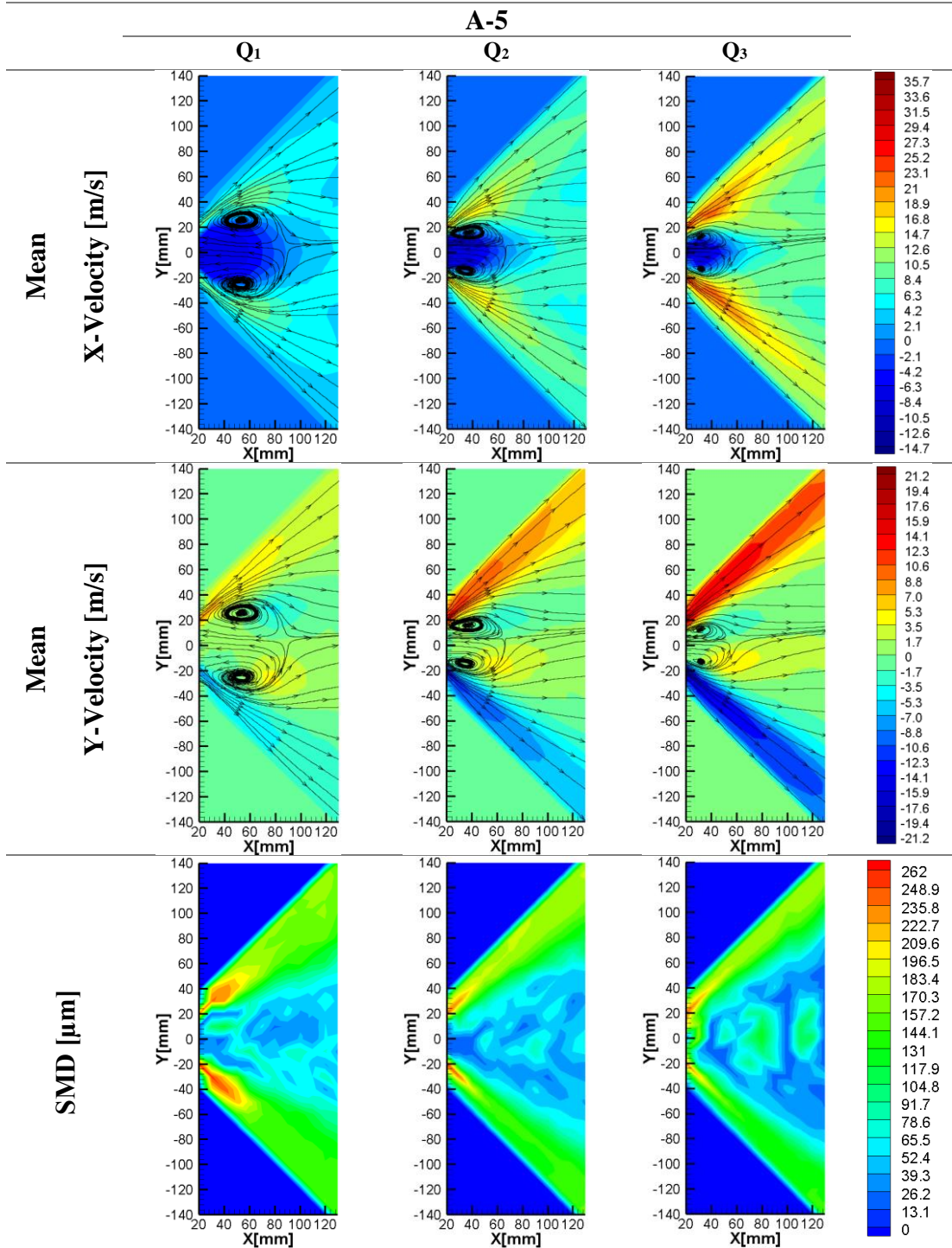


Figure A.9. Mass Flow Rate Effect on the Microscopic Properties of A-5

A-5 ($N_{ip}=2$)

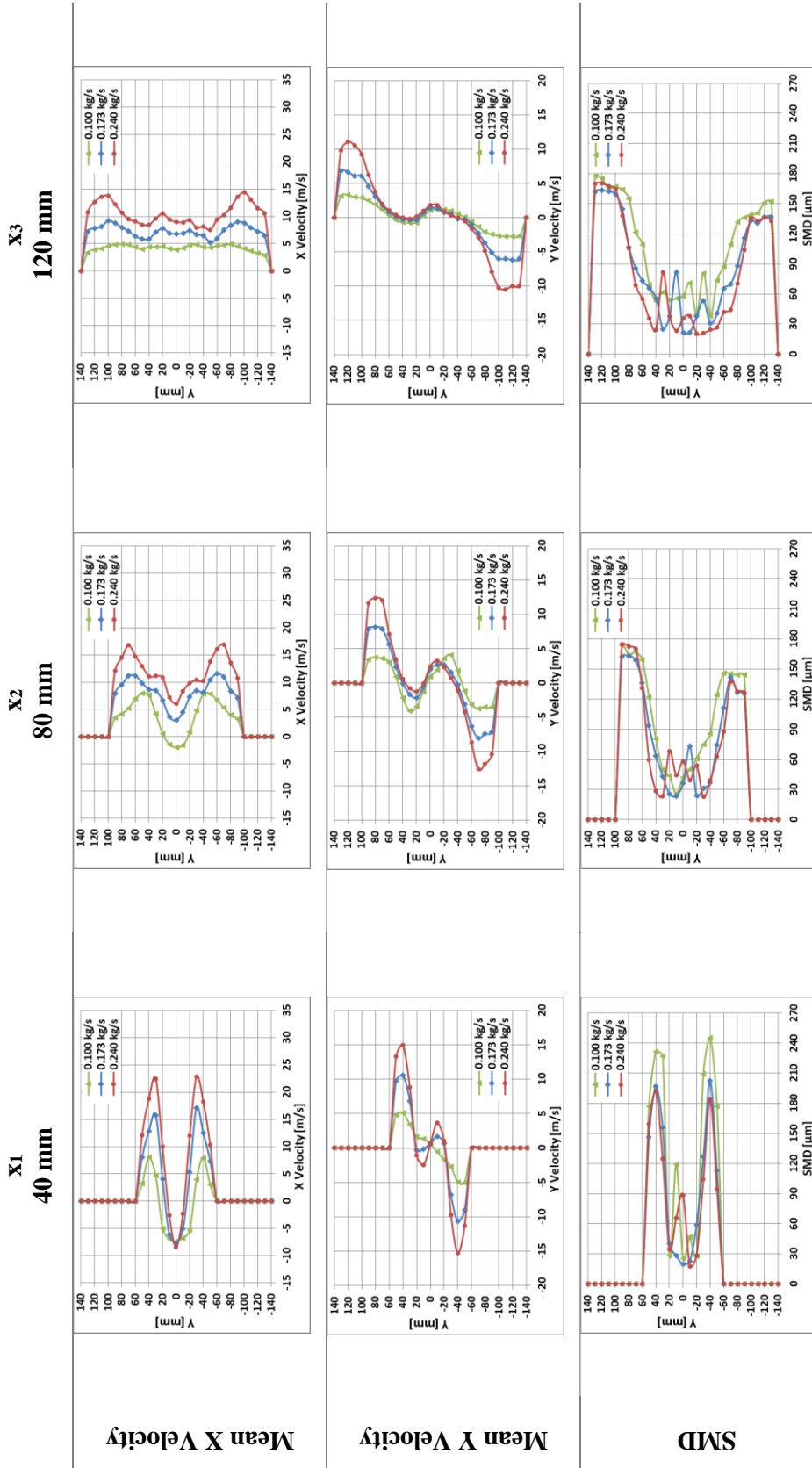


Figure A.10. Comparison of Mass Flow Rate Effects on the Microscopic Properties of A-5 at Specified x Coordinates

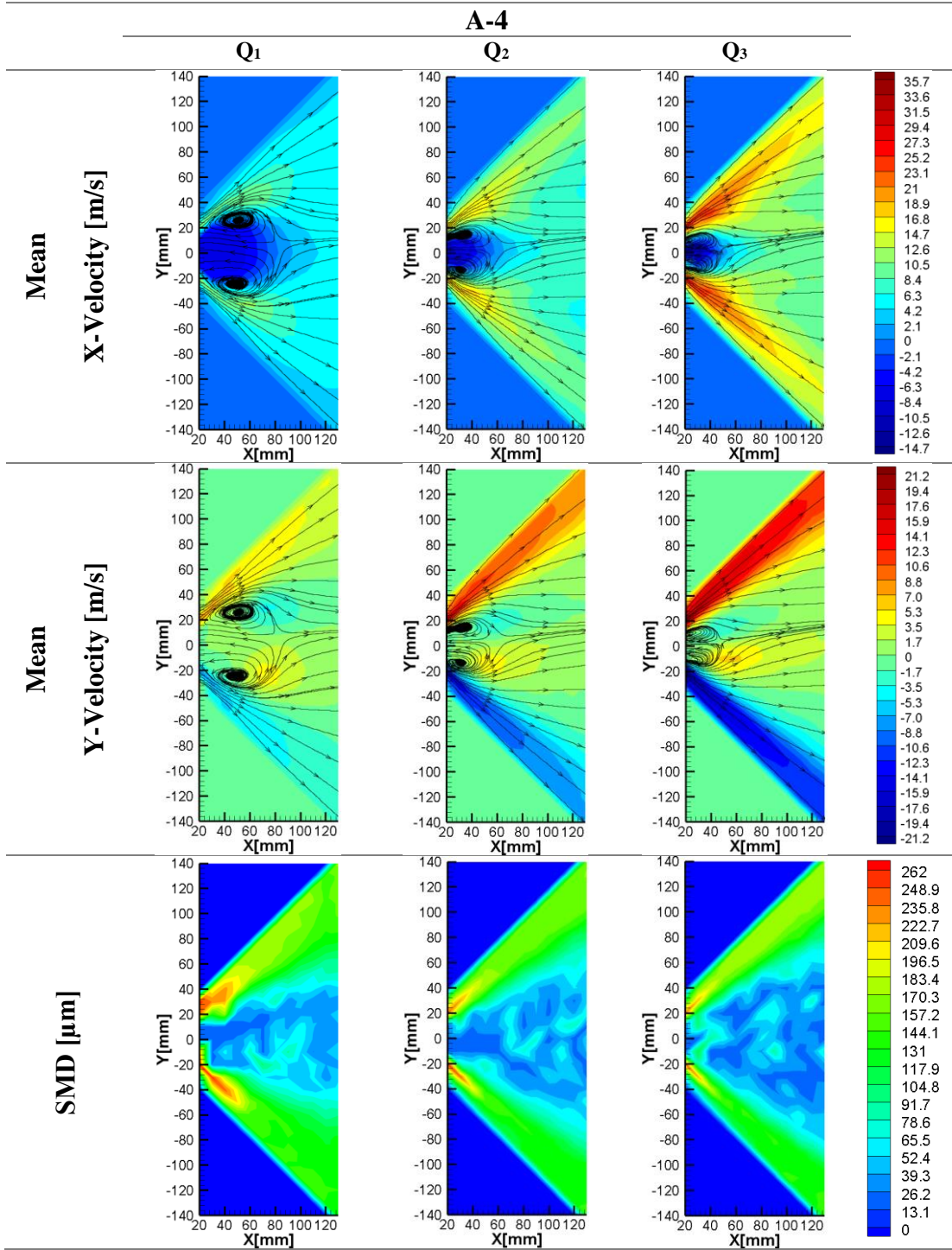


Figure A.11. Mass Flow Rate Effect on the Microscopic Properties of A-4

A-4 ($N_{ip}=4$)

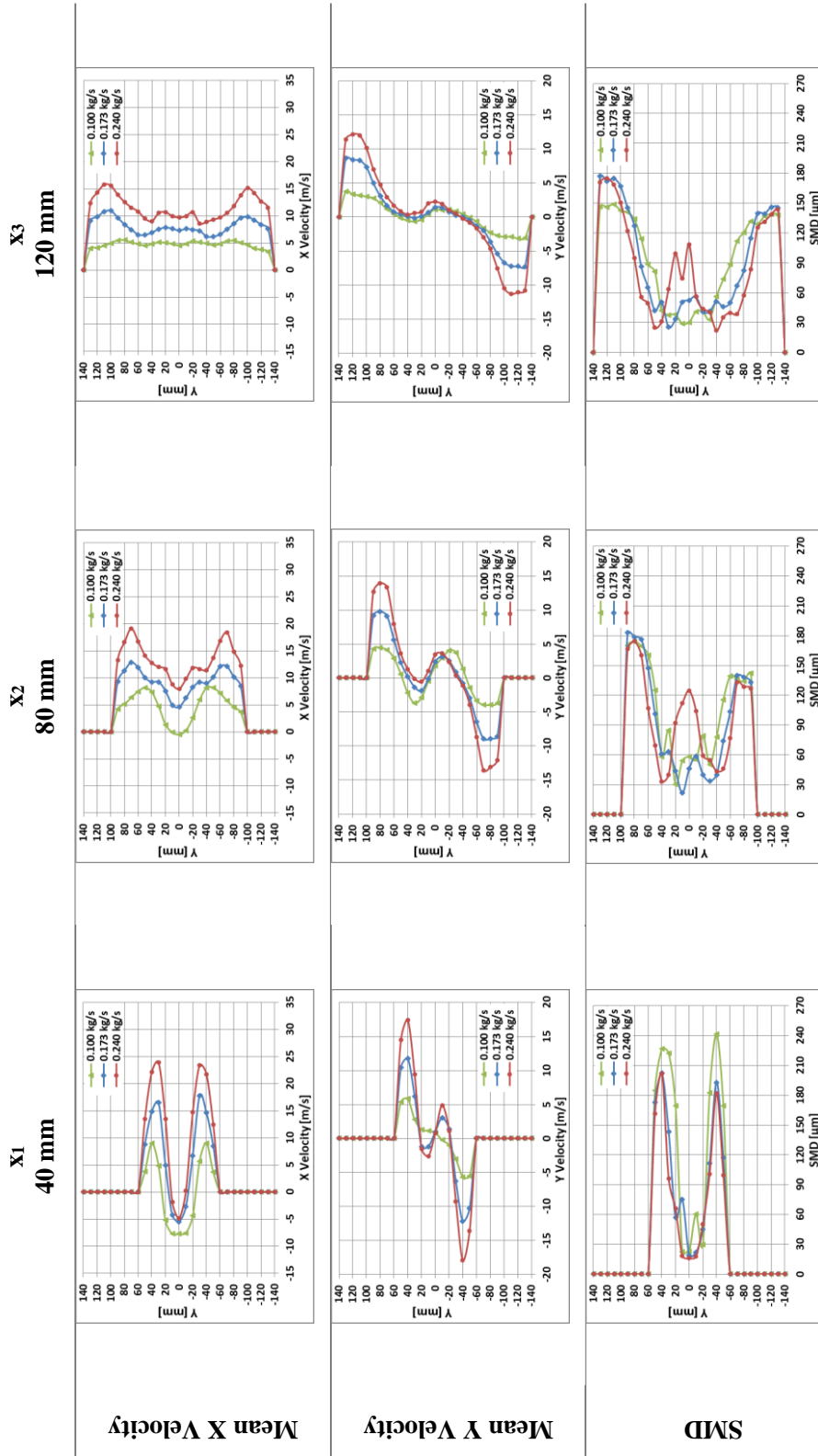


Figure A.12. Comparison of Mass Flow Rate Effect on the Microscopic Properties of A-4 at Specified x Coordinates